Development of an Intelligent Standalone Solar Photovoltaic 48V DC Microgrid System.

By

Thandeka Makhanya

A Thesis Submitted to the Faculty of Engineering and the Built Environment

in Fulfilment of the Requirements for the

Master of Engineering

In

Electronic and Computer Engineering

In the

Faculty of Engineering and the Built Environment

At the

Durban University of Technology

Supervisor: Dr. N Pillay

Co-Supervisor Mr. R. Sewsunker

PLAGIARISM AND DECLARATION

1. I know and understand that plagiarism is using another person's work and pretending it is one's own, which is wrong.
2. This essay/ report/ project is my work.
3. I have appropriately referenced the work of other people I have used.
4. I have not allowed and **will not allow** anyone to copy my work to pass it off as his/her own work.

29-11-2023

Thandeka Makhanya Date

Student Number: 20502104

This research was duly supervised by Dr. N Pillay and co-supervised by Mr. R. Sewsunker at the Durban University of Technology. This thesis is the student's own work, every cited work or text has been properly referenced. It has not been partially or fully submitted to any other University.

18 March 2024

Supervisor: Dr. N. Pillay Date

18 March 2024

Co-supervisor: Mr. R. Sewsunker Date

ABSTRACT

With load shedding negatively affecting South Africans there are many concerns regarding stable power delivery to residential households. Amid all the power delivery concerns some rural communities are still not connected to the existing power infrastructure. Implementation of newer efficient clean energy sources is in demand. A standalone Photovoltaic (PV) Solar distributed renewable energy Direct Current (DC) microgrid can be the best possible approach to tackle the power grid shortcomings and to electrify communities that are not yet covered by the power grid or communities that want to transition to clean energy.

The research focuses on the design of an optimal 48 VDC Multiple-PV Standalone microgrid in remote areas not covered by the main grid. The proposed microgrid can be typically used for lighting, charging phones, and other low-power applications. The microgrid will consist of 4 microgrid subgrids, each consisting of a dedicated Solar PV array, battery storage systems, loads, and other components that connect to the DC Bus and need to be monitored and controlled for efficient operation.

Furthermore, the subgrids were designed based on the meteorological data of the selected location and the load demand for each subgrid. The microgrid design enables the subgrids to share power through a bidirectional DC-DC converter based on certain conditions. A power-sharing management system was implemented to manage power-sharing ensuring that the sharing subgrid does not drive its users to load shedding.

Moreover, the microgrid design was simulated on Matlab/Simulink to observe the operation of the designed system and to determine if the proposed design would be able to achieve the desired goal. The results obtained from simulations indicate that the proposed microgrid design can provide an optimal service to its users by allowing the subgrid with surplus energy to share its power with the subgrid when needed.

PUBLICATIONS

A conference paper titled "**A Distributed Standalone Solar PV and Battery Energy Storage System DC Microgrid"** was presented at the 2023 31st Southern African Universities Power Engineering Conference (SAUPEC), 24-26 January 2023, University of Johannesburg, South Africa.

ACKNOWLEDGEMENT

I would like to thank God Almighty for paving the way and enabling me to reach every milestone required, my supervisor Dr. N Pillay, and my co-supervisor Mr. Sewsunker for the support, guidance, and direction they provided for my research thesis. I am grateful for the support my family (the Makhanya Clan) provided during the period of my research.

This study is dedicated to my forever fans, my Mom, Mrs. W.N Makhanya, and my dad, Mr. BI Makhanya. Thank you for your love, care, and encouragement.

Table of Contents

List of Figures

List of Tables

List of Abbreviations

AC	Alternating Current
BES	Battery Energy Storage
CCSA	Cable Cross Sectional Area
DBS	DC Bus Signaling
DC	Direct Current
DERs	Distributed Energy Resources
DG	Distributed Generation
FCFS	First Come, First Served
GC	Global Control
GCM	Global Control Monitor
GHI	Global Horizontal Irradiance
KCL	Kirchhoff's Current Law
KVL	Kirchhoff's Voltage Law
LFC	Load Flow Control
MPPT	Maximum Power Point Tracker
NIBBBC	Non Isolated Bidirectional Buck Boost Converter
OES	Open Energy System
PS	Priority Selector
PSMS	Power Sharing Management System
PV	Photovoltaic
PWM	Pulse Width Modulated

RE	Renewable Energy
RERs	Renewable Energy Resources
SOC	State of Charge
SSM	Surplus Subgrid Monitor
VD	Voltage Drop
IC	Incremental Conductance
FLC	Fuzzy Logic Controller

List of Symbols

Symbol	Unit	Description
$\tilde{\imath}_{\mathrm{L}}$	A	Inductor current perturbation
$\tilde{v}_{\mathrm{in}}$	V	Input voltage perturbation
$\tilde{v}_{\mathrm{out}}$	V	Output voltage perturbation
Δi_L	A	Inductor ripple current
Δv_c	V	Capacitor ripple voltage
B_C	Ah	Battery capacity
B_{GC}	Ah	Battery global capacity
C_A	mm^2	Cable cross sectional area
$CC(I_R)$	A	Charge controller minimum current rating
$CC(V_R)$	V	Charge controller minimum voltage rating
C_L	m	Cable length
E_L	W/h	Average Load daily demand
I_C	A	Cable maximum current
I_{Max}	A	Charge controller maximum input current
N_B	-	Number of batteries
N_{BP}	-	Number of batteries in parallel
N_{BS}	-	Number of batteries in series
N_{CCP}	-	Number of parallel connected charge controllers
N_P	-	Number of parallel connected PV panels
N_{Pv}	-	Number of PV panels
N_S	-	Number of PV panels connected in series
$PV(I_{SC})$	A	PV panel short circuit current
$PV(V_{OC})$	V	PV array open circuit voltage
PV_{NP}	W	PV module nominal power
PV_{PP}	kW	PV array peak power
R_L	R	Load resistor
V_B	V	Battery voltage

V_{Bus}	V	Bus voltage
V_D	V	Cable voltage drop
V_L	V	Voltage across the inductor
V_{Max}	V	Charge controller maximum input voltage
V_{in}	V	Input voltage
V_{out}	V	Output voltage
$\tilde{d}$	%	Duty cycle perturbation
i_L	A	Current passing through the inductor
t_{on}	s	Switch ON period
ΔQ	C	Change in charge
h	m	Height
A	-	Autonomy
ASH	kWh/m^2	Annual average daily sun hours
C	F	Capacitor
D	%	Duty cycle
DOD	%	Battery depth of discharge
L	H	Inductor
T	s	Total switching period
b	mm	Breadth
f	f	Switching frequency
k	-	Safety coefficient 1.25
l	M	Length
w	mm	Width
ρ	Ω m	Cable resistivity
DT	s	Switch ON period
(1 – D)T	s	Switch OFF period

CHAPTER 1: INTRODUCTION

1.1 Background

In [1], the South African Department of Mineral Resources and Energy states its future investment plan in renewable energy resources (RERs) to curb high emissions of greenhouse gasses. The Integrated Resource Plan 2019 [1] also states that 80% of the country's greenhouse gases are contributed by the energy sector of which 50% are contributed by the generation of electricity and liquid fuel production. The installation of Standalone PV RERs can assist in electrifying rural and remote areas not connected to the power grid while curbing the increase and high percentage of greenhouse gasses contributed by the energy sector of the country.

“In recent years, supplying electricity has become necessary for daily survival and further development of emerging communities” [2]. The injection of more RERs in remote areas, rural areas, and other areas that are not yet covered by the power grid can help reduce the dependency on fossil fuels for energy production. Fig. 1.1(a) illustrates the scale of an average daily Global Horizontal Irradiation that is available on the horizontal surface of South Africa depending on location [3]. Fig 1.1(b) illustrates the scale of average daily PV power potential that can be harvested from the sun in South Africa depending on location [3].

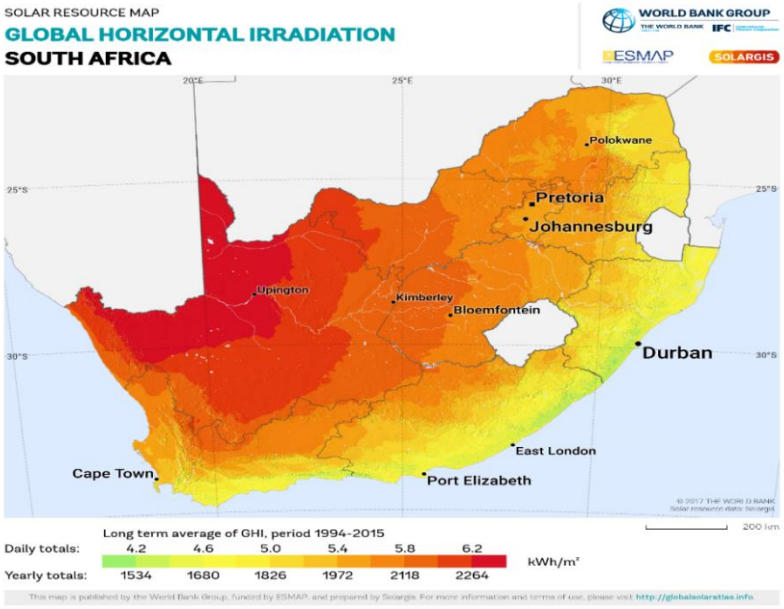

(a)

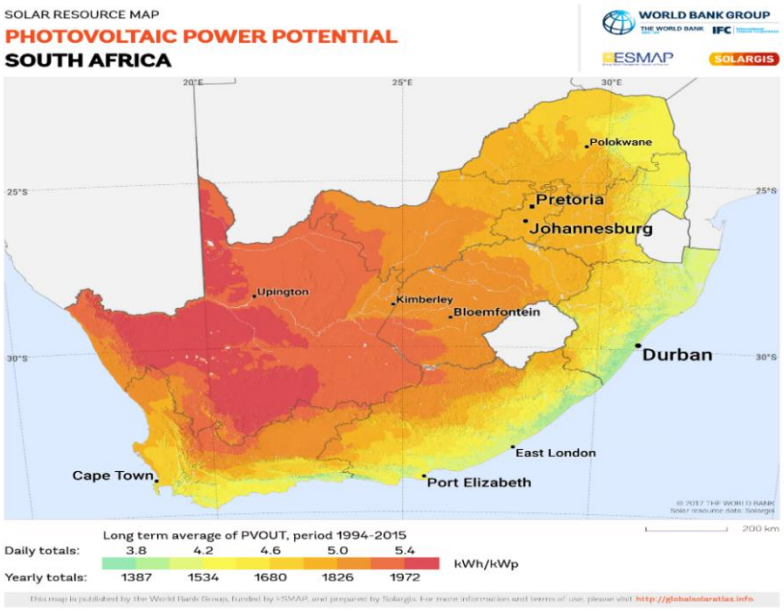

(b)

Figure 1.1 South African Solar Resource Map. (a) Global Horizontal Irradiation (b) PV Power Potential [3]

Furthermore, research and studies are conducted around the world to power remote and rural areas with RERs. In [4] a 72V DC grid system was designed to power homes for basic electrical needs like lighting, fans, and charging of computers/phones. The system is designed to power rural and remote areas in India where it costs a fortune for communities to access the utility grid. Moreover, a study was conducted in [5] to optimally control the flow of power between multiple interconnected microgrids. The study in [5] had similar features as the proposed research like power-sharing between Multiple-PV generation points. However, it was tied to the utility grid. In the proposed study, the microgrid system will have no connection with the utility grid. The standalone DC microgrid will be monitored and controlled for optimal operation.

1.2 Problem Statement

"The Photovoltaic (PV) based distributed energy resource is one of the most promising alternative energy resources owing to the abundance in sunlight and offers the cleanest form of alternative energy generation" [6]. The South African Department of Energy states that South Africa has an average of more than 2500 hours of sunshine per year and an average daily solar irradiation levels range between 4.5-6.5 $kWh/\ m^2$. South Africa has a high potential solar energy resource ready to be harvested [7], however, the country is lacking in implementing solar energy harvesting

technologies. Furthermore, the country's total energy generation is 51.7 GW with only 5.4 GW generated from renewable energy (RE) [1]. The development of standalone solar PV array microgrid can assist in electrifying rural and remote areas not connected to the power grid while curbing the increase and high percentage of greenhouse gasses.

1.3 Aim and Objectives

The research aims to design a PV standalone distributed 48V DC microgrid to power areas not covered by the utility and analyze the effect of using Multiple-PV arrays as a source for an optimal standalone 48V DC microgrid. Below are the objectives of the research:

I. Search for a rural location suitable for PV system implementation based on the meteorological data.
II. Design a 48V DC Multi-PV array standalone microgrid for Mhlungwane Village, Nqutu ward 7, KwaZulu Natal, South Africa.
III. Design and simulate the proposed scheme in Matlab/Simulink software.

1.4 Thesis Outline

I. **Chapter 1** – This chapter outlines significant research attributes including background, problem statement, aim and objectives.
II. **Chapter 2 –** This chapter reviews the literature related to renewable energy, solar energy, energy conversion, energy storage, distributed generation, microgrids, and power-sharing.
III. **Chapter 3 –** This chapter focuses on the design of the 48V DC multi-PV array standalone microgrid. The PV array, battery storage, charge controller, and cable are sized utilizing calculations with equations and then sized utilizing the PVSyst software tool.
IV. **Chapter 4 –** In this chapter, the designed microgrid in chapter 3 is simulated on Matlab/Simulink.
V. **Chapter 5 –** Results obtained from simulating the microgrid in chapter 4 are discussed.
VI. **Chapter 6 –** The conclusion is presented in this chapter which highlights the research results and recommendations for further studies.

CHAPTER 2: LITERATURE REVIEW

In this chapter, the literature associated with the proposed research is presented. This section will cover literature based on RE, Distributed Generation (DG), DC microgrid Topologies, standalone PV DC microgrid, standalone PV DC microgrid components, power sharing, and DC microgrid control. An overview of the components associated with the proposed research is presented.

2.1 Renewable Energy

RERs illustrated by Fig. 2.1 such as Bioenergy, Hydropower, Geothermal, Wind, and Solar are abundant within the time horizon of humanity [8], they are abundantly available and can be harvested and utilized. Moreover, more people around the world are exposed to the negative effects of climate change caused by fossil fuel consumption [9-12]. The negative impacts of fossil fuels on the environment have pushed for more research, and the consumption of RE has rapidly grown over the past decades to reduce the use of fossil fuels as a source of energy.

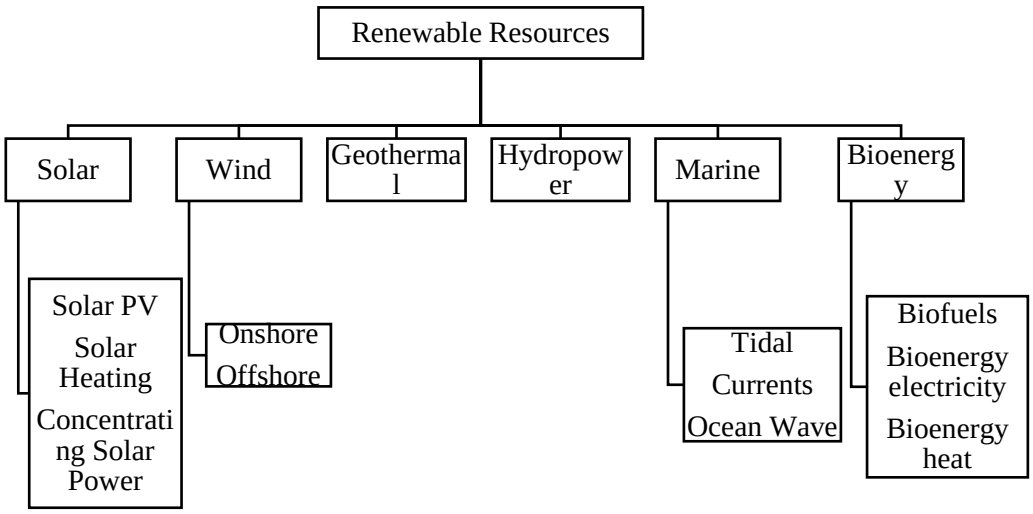

Figure 2.1 Renewable Energy Resources [8][13]

Furthermore, renewable energies are the best option that can cover the energy requirements in a climatically sustainable way [14]. They are considered a clean source of energy that minimizes environmental impacts by mitigating CO_2 emissions since they can provide energy with almost zero emissions of pollutants and greenhouse gases [14].

Moreover, the Earth receives about $3.9x10^{24}J \approx 1.08x10^{18}KWh$ of solar energy yearly. This is ten thousand times more than the global primary energy demand per year, which means the solar energy that reaches Earth can be used to cover the energy demand of humanity [15]. Solar energy is the most inexhaustible RE which can be obtained in direct or indirect form. According to [16] South Africa has the potential PV power of $42243\ TWh/Year$ and has the advantage since Solar energy is becoming more economically feasible with time [17].

2.2 Distributed Generation

Local power generation from Distributed Energy Resources (DERs) is called Distributed Generation. [18] states that DG systems can be designed and implemented based on various DER technologies which are RERs, non-RERs, and energy storage. Fig. 2.2 illustrates the DG technologies available. Moreover, DG energy systems can be can be utilized as a backup for the power grid or off-grid.

Furthermore, since microgrids implemented from renewable and storage DERs are advancing in efficiency, and decreasing in cost they are viewed as the best option for rural and remote areas electrification where it can be high cost to transmit and distribute power grid electricity. Moreover, proper sizing, installation, and choice of location for a distributed generation can remarkably reduce system losses, improve power quality and system dependability [17]. PV arrays and BES systems are the DG technologies applied in the proposed system's design.

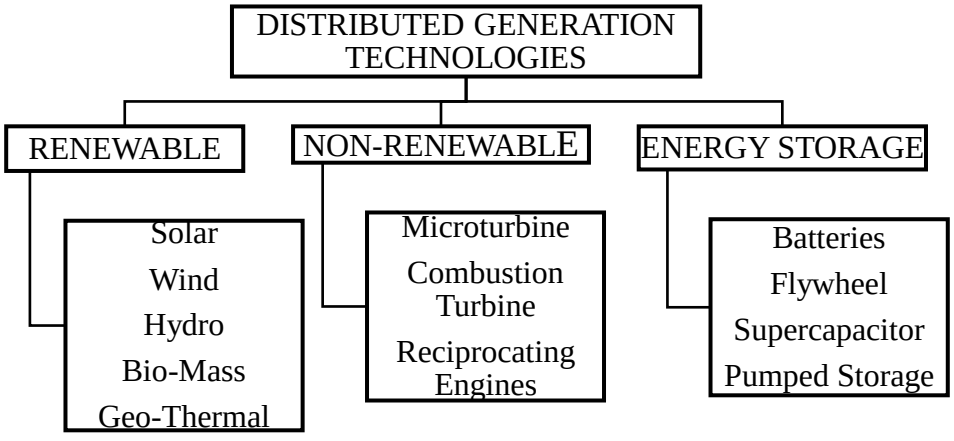

Figure 2.2 Distributed Generation Technologies [18]

2.3 DC Microgrid Topologies

The topology describes the structure of the DC microgrid configuration. Different topologies can be applied when designing a DC microgrid depending on your goal. Each topology has its characteristics which can aid a designer in selecting the appropriate structure for their DC microgrid.

2.3.1 Single Bus DC Microgrid

This topology comprises a single DC bus as illustrated by Fig. 2.3. Some components are connected directly to the DC bus while others are connected via a converter [19].

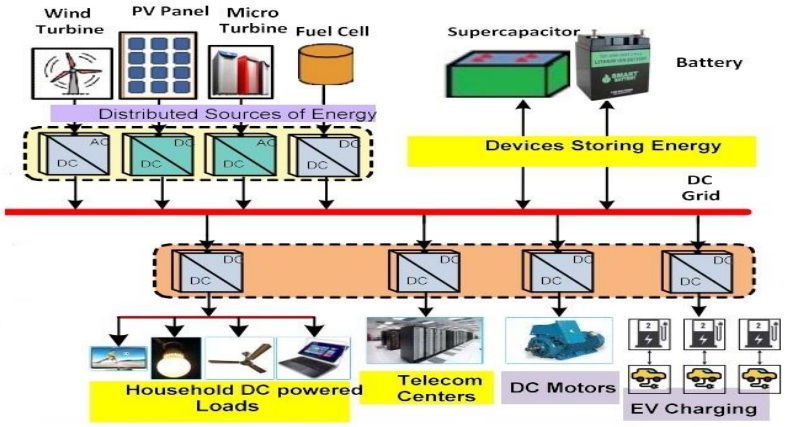

Figure 2.3 Single Bus DC Microgrid Topology [20]

2.3.2 Multi-Bus DC Microgrid Topology

Fig. 2.4 illustrates the multi-bus DC microgrid topology, with multiple clusters interconnected via DC Buses. The interconnection gives each cluster the ability to share power to and from the neighboring clusters [19].

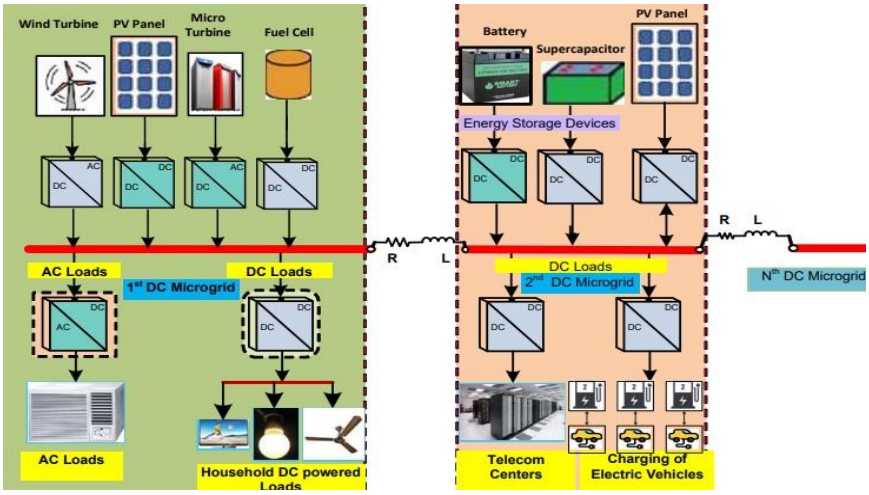

Figure 2.4 Multi Bus DC Microgrid Topology [20]

2.3.3 Ring Bus DC Microgrid Topology

The ring bus topology illustrated by Fig. 2.5 allows for a loop connection of all DERs and loads to the ring Bus through converters. This topology is more flexible than the single bus topology since when there is a presence of a fault in one of the DERs, the microgrid will continue supplying power to loads [19]. However, the fault presence in the ring bus DC microgrid will cause a loss of loop connection, and the topology changes from ring to single bus [19].

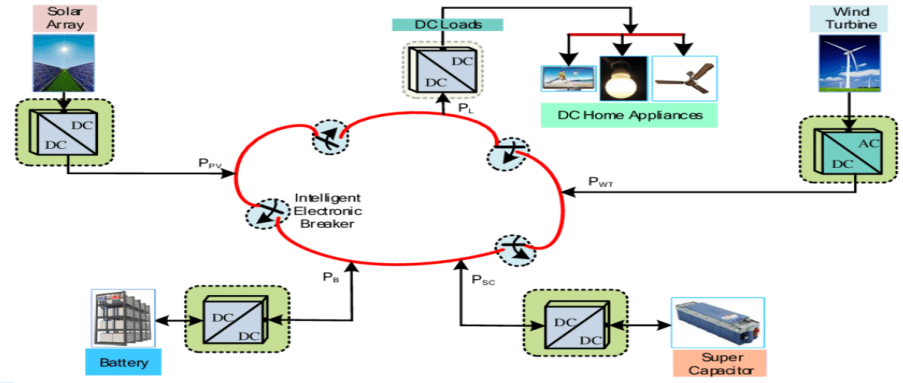

Figure 2.5 Ring Bus DC Microgrid Topology [20]

2.3.4 Zonal Bus DC Microgrid

The zonal bus topology is illustrated in Fig. 2.6, this topology has multiple DC buses and the microgrid is split into zones. Each zone has its dedicated load which is supplied by DERs [19].

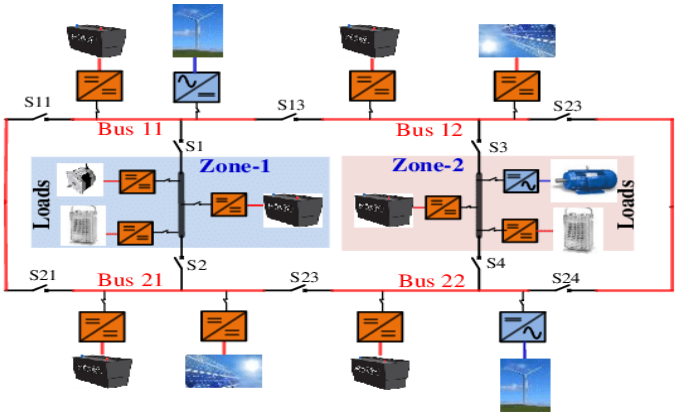

Figure 2.6 Zonal Bus DC Microgrid Topology [21]

2.3.5 Interconnected DC Microgrid Topology

The interconnected DC microgrid topology is illustrated in Fig. 2.7. This topology has multiple DC buses which are all interconnected. The reliability of the microgrid is improved since all loads are interfaced with all DERs through the interconnection of buses. If one DER is disconnected, the power will continuously flow to all loads from the connected DERs [21, 22].

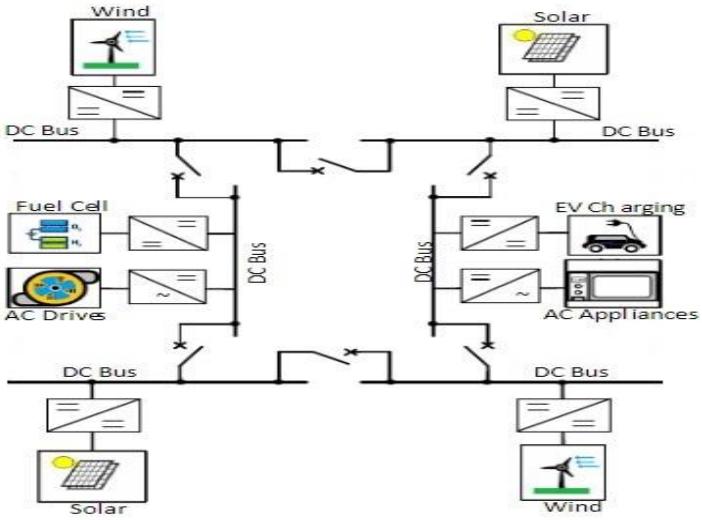

Figure 2.7 Interconnected Bus DC Microgrid Topology [22]

2.4 Standalone PV DC Microgrid

The standalone DC microgrid system operates without the power grid connection. Fig 2.8 illustrates a distributed standalone PV-Battery DC microgrid. Renewable energy (RE) DERs as standalone microgrids are identified as a potential solution for addressing rural electrification and

have several applications in automotive industries, marine technologies, and communication centers [23]. The proposed microgrid is standalone since power is generated and consumed in the same location and has no connection whatsoever with the power grid. The proposed system is suitable for the electrification of remote rural areas or small communities that do not have access to the power grid power due to economic or geographical constraints.

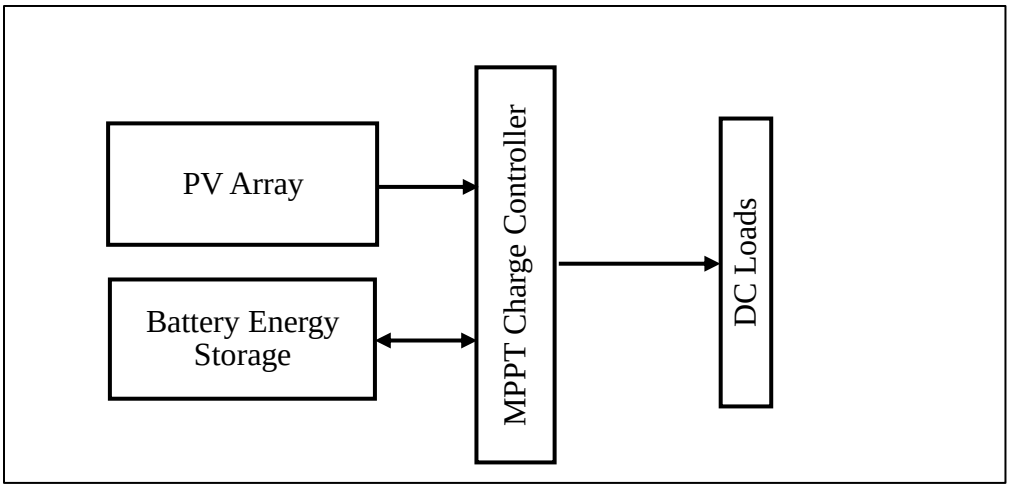

Figure 2.8 PV Standalone system with battery storage and without inverter.

Furthermore, research papers have presented possible solutions to power remote and rural areas. Where it costs too much to run the power grid or is impossible because of geographical reasons. In [24] a design of a low voltage DC microgrid system for rural electrification is covered. The DC microgrid system consists of a PV array as the RERs, a BES system, and a charge controller to control the charging and discharging of the Batteries.

Research conducted by [25], indicates that an improved typical design method for a standalone PV system can be utilized to electrify remote and rural areas, while [26] emphasizes that the standalone PV system must be able to provide maximum efficiency, reliability, and flexibility at an affordable cost. Moreover, [27] emphasizes the importance of a proper design of the standalone PV system, stating that if the system is optimally designed it can be reliable to its users while costing less. Different methods are suggested that can assist system designers in optimally designing a standalone PV system in terms of cost and reliability.

Moreover, research shows that standalone distributed DC microgrids are a promising option in the integration of RERs, distributed non-RERs, and energy storage for optimization of reliability and cutting costs [28]. A study was conducted to investigate the costs incurred by users of different power utilities: AC, Smart AC, and DC homes [28]. Results showed that DC homes with DC loads cost less compared to AC and smart AC. The results conclude that DC microgrids can assist in lowering household costs which is good for powering poor rural areas.

2.5 Standalone PV DC Microgrid Components

Research and studies are continuously conducted to improve the efficiency of RER systems. Some of these studies focus on individual components that make up the complete system like PV power, energy storage, DC-DC converters, and charge controllers. All these components play a vital role in the system's proper functioning. Published research will assist when designing the proposed system to choose the most suitable system components.

2.5.1 Photovoltaic Power

Photovoltaic power is obtained when photovoltaics directly convert sunlight to electricity in a process called the PV effect. Photovoltaics are efficient in converting solar energy into electrical energy [29]. Among renewable energies, photovoltaics are said to be the highest in adaptability as they can be customized to any desired generator size. Since PV power is only generated during the presence of sunlight, battery backup is vital to supply the loads during the absence of sunlight [30].

PV power systems comprise a PV array/module which is the source of electric energy. PV array is the series, parallel, or series-parallel connection of PV modules. Series for higher voltages, parallel for higher currents, and series-parallel to achieve the required power [31]. PV module is the connection of PV cells in series, parallel, or series-parallel for desired output [31]. A PV cell is a *pn* junction barrier device that can convert sunlight directly into electricity. It is usually made of silicon with traces of other elements through a doping process. Only 15-25% of the sunlight's energy is absorbed by the PV cell [32]. When photon energy from the sun is absorbed by a PV cell, electrons move through the material producing a voltage [31].

Moreover, PV cells are manufactured differently using diverse types of semiconductor materials which act as an insulator at low temperatures and as a conductor when heat is available [33]. PV cell technologies include monocrystalline silicon, polycrystalline silicon, Amorphous/thin-film silicon, and Hybrid silicon cells.

2.5.2 Battery Energy Storage System

A reliable BES system is vital for the efficient operation of most PV standalone systems since the production of power only occurs in the presence of sufficiently strong sunlight during the day. A BES system will be used in the proposed research for backup when there is no sunlight available for energy production by a PV array. The battery stored power supplies the loads during the absence of sunlight required by the PV array to produce power [34]. Different battery technologies are used with PV standalone systems which include nickel-cadmium, nickel-metal-hydride, lithium-ion phosphate, and lead-acid [35].

Moreover, batteries that are used with PV systems are required to have a deep cycle, thicker plates, and greater surface area than the typical motor battery. PV standalone systems with BES systems can supply the DC loads directly with the DC power or a DC-DC converter can be used to regulate power [36]. The proposed PV standalone systems will use photovoltaics as a source for battery charging**.** The energy transferred to the battery will be controlled by the MPPT charge controller accordingly which regulates the output of the PV array [37].

2.5.3 Charge controller

A charge controller is an electronic regulator used to regulate voltage and current flowing to and from the batteries to avoid overcharging and/or over-discharging which can damage the batteries [31]. Diverse types of controllers are available such as a series charge controller, shunt charge controller, PWM (Pulse-Width-Modulated) charge controller, and MPPT (Maximum Power Point Tracker) charge controller.

Furthermore, [38] presents research that analyzes different charge controllers that can be utilized with numerous solar panels. The analysis was between two charge controller types, the PWM and the MPPT charge controller. The analysis showed that using the MPPT controller can be beneficial as it can harvest maximum charge from solar panels even in difficult weather conditions.

MPPT

MPPT controllers are used with the PV module/array to track the MPP of the PV module/array. Power harvested from the PV module/array varies depending on the state of atmospheric temperature, cell temperature, and solar irradiance. To extract maximum power in real time from the PV module/array regardless of the temperature and solar irradiance state, the MPPT controller is utilized. The MPPT controller can be designed based on a variety of MPPT methods, which include [39, 40]:

I. Measurement and Comparison Based Methods.
II. Mathematics Calculation Based Methods.
III. Intelligence-Based Methods.

In [41] a comparative study was conducted between three MPPT techniques, Perturb and Observe (P&O), Incremental Conductance (IC), and Fuzzy Logic Controller (FLC). The techniques were implemented and simulated on Matlab/Simulink to analyze their performance for power extraction and tracking efficiency in steady state and dynamic behavior considering the variable irradiance and constant temperature. FLC demonstrated a better steady state behavior while P&O demonstrated smooth transition dynamic behavior. The results further demonstrated P&O to be more efficient in tracking and power extraction.

The P&O algorithm which is based on the measurement and comparison method will be utilized to implement the MPPT controller for the proposed microgrid. The P&O technique is broadly used compared to other techniques since it is easy to implement and can provide the best performance at a low cost [42]. Moreover, a study was conducted by [43] where they evaluated the P&O and IC algorithms under variable temperature and solar irradiance operating conditions. The algorithms were simulated in Matlab/Simulink and the results obtained demonstrated the P&O to be faster in reaching MPP and to fully charge a battery.

2.5.4 DC-DC Converters

A DC-to-DC Converter converts one value of DC voltage to a desired value. A buck converter takes a high voltage as an input and bucks down the high input voltage to a low output voltage, while a boost converter takes a low voltage as an input and boosts the low input voltage to a high

output voltage [31]. The proposed system design for the research will consist of a bidirectional DC-DC converter which is vital for the interface of the microgrid subgrids for power-sharing and battery charging and discharging.

Furthermore, [44] Emphasizes the vital role played by a bidirectional DC-DC converter to interface a PV system with a battery storage system. A bidirectional DC-DC converter can operate as both the buck and boost converter for both the BES system and loads. A non-isolated bidirectional buck-boost DC-DC converter topology is presented in [45] for battery charging. This converter is available in different topologies (Push Pull, Full Bridge, and Half Bridge). The presented bidirectional converter uses bidirectional switches (MOSFET or IGBT) to control the charging and discharging of batteries. Its operation with the PV system was simulated and analyzed using Matlab/Simulink.

Furthermore, [46] proposes a control technique for a bidirectional DC-DC converter intending to stabilize the DC bus voltage for RERs. The cause of the DC bus voltage being unstable is the fluctuating power produced by RERs due to uncontrollable environmental factors. The proposed control technique is the "selector-based algorithm converged with a proportional-integral control" [46]. This control technique triggers the bidirectional DC-DC converter to buck or boost according to the DC bus voltage and battery charging voltage maintaining the DC bus voltage constant during any changes from the sources and loads.

Moreover, the proposed control technique was simulated on a DC microgrid with two independent PV arrays, the analyzed results from the proposed control method and standard DC microgrid without the proposed control technique prove the proposed control technique to be efficient in keeping DC bus voltage constant.

2.6 Power-sharing

The efficiency of RE systems is vital, as more studies are being conducted to improve RE systems' optimality. Studies present the interconnection of nano-grids and microgrids to improve RE system efficiency and reliability. A study is conducted in [47] to compare three microgrid topologies

illustrated by Fig. 2.9, the three topologies are centralized microgrid, distributed standalone home system, and OES (open energy system) which is the hybrid approach with interconnected nanogrids. The topologies were implemented in a 20-household rural community. The study compares the solar replacement ratio of the topologies for the community.

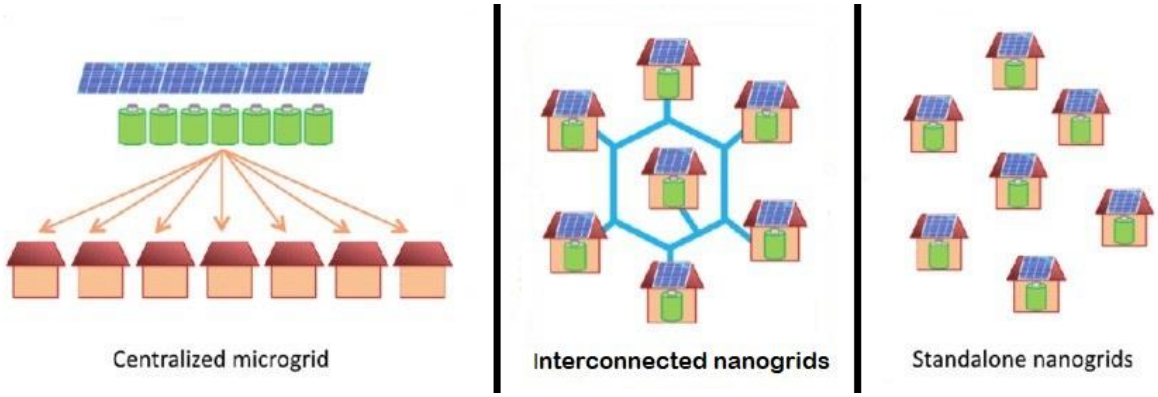

Figure 2.9 Three Microgrid Topologies [48]

Furthermore, in the latter approach, the households are interconnected and can share power via a bidirectional DC-DC converter. Moreover, the OES also has a communication system that manages the demand and response between interconnected households. The results obtained demonstrate that the OES has a better performance compared to standalone nanogrids. While [49] proposes various operational schemes that can be used when interconnecting DC microgrids through an isolated bi-directional DC-DC converter, a DC signaling operational scheme is proposed to be used to restore the DC bus voltage from general overload or failure situations in standalone DC microgrids.

Furthermore, the direct transmission operation scheme is proposed to be used with power grid connected microgrids. The proposed operational scheme intended to provide efficient and reliable power management, by allowing efficient power transfer between adjacent DC microgrids. The proposed schemes were implemented and tested in a laboratory experiment and results showed improved efficiency and reliability of the microgrids, overcoming the limitations of a single DC microgrid. On the other hand, [50] proposes the Load Flow control LFC method for

interconnecting and controlling bidirectional power flow between multiple DC microgrids by applying and controlling voltage between the microgrids. LFC is a combination of a Dual Active Bridge and a full bridge DC-DC converter which allows for efficient power flow between multiple microgrids at different voltage levels.

Furthermore, [51] develops power control and management distributed control strategy based on DC bus signaling for individual autonomous DC microgrids and autonomous DC microgrids without a communication system. This strategy uses bus voltage information to trigger power-sharing between microgrids and to control/manage loads, storage, and sources [51]. The proposed control strategy is a non-communication power control strategy for interconnected microgrids aimed to improve system reliability and effectiveness.

The interconnection of equal and non-equal capacity DC microgrids through an isolated DC-DC bi-directional converter for power-sharing and increased reliability of the microgrids is discussed in [52]. The proposed study will also tackle the issue of efficiency and optimality of renewable sources by interconnecting microgrids through a bidirectional DC-DC converter to share power for optimal operation. The management control system will be implemented to ensure the best operation of the entire microgrid without a communication link.

2.7 DC Microgrid Control

DC microgrids are designed and implemented to achieve efficient, reliable, and stable operation to provide optimum service for users, optimality is achieved by implementing control strategies for the microgrids. Control strategies are implemented to achieve a smooth transition between DG sources, power flow control between interconnected microgrids, current/voltage/power control, proportional load sharing, and coordination between DG sources and energy storage devices. Fig. 2.10 illustrates the control strategies and the control modes that are applied for each control strategy. The subsections below describe the control strategies:

2.7.1 Centralized Control Strategy

This control strategy utilizes a central controller to control DG sources and the energy storage system. The central controller collects data and send instructions to local controllers via a communication link [19]. If the communication system fails it will impact the efficiency, reliability, and stability of the microgrid. Moreover, the Master-Slave is the mode of control for the central controller [53].

2.7.2 Decentralized Control Strategy

In the decentralized control strategy, DG sources and energy storage devices have dedicated controllers. This strategy does not require communication links but depends on a common DC bus value for control [19]. Furthermore, DC Bus Signaling and Droop control are the modes of control for this control strategy [53].

2.7.3 Distributed Control Strategy

The distributed control strategy is the best compared to both centralized and decentralized since it has the advantages of both control strategies. The local controllers communicate by communication links, moreover, failure of the communication link of a DG unit will not affect the operation of other DG units [19]. Consensus and Agent based modes of control are applied to achieve the distributed controller [53].

2.7.4 Multilevel Control Strategy (Hierarchical)

The multilevel control strategy is applied to microgrids that require higher intelligence control systems to achieve power sharing, current/voltage/power control, and more control objectives. The multilevel control strategy can either be 2 (Lower and Upper) or 3 levels (Primary, Secondary and Tertiary). Moreover, the distinct levels of hierarchical control apply 1, 2, or more control strategies mentioned in sections 2.71-2.7.3 [53]. The proposed system will implement the hierarchical control strategy for system efficiency, reliability, and stability.

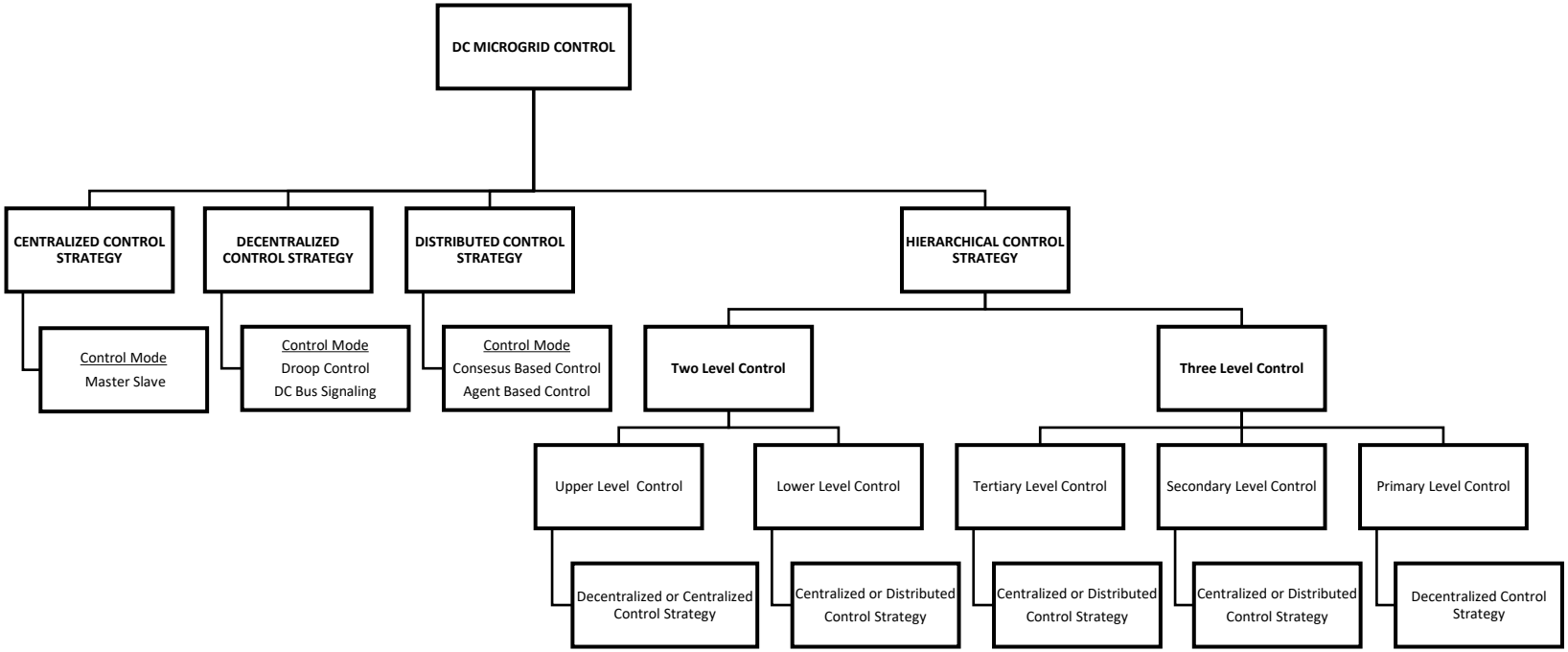

Figure 2.10 Control Strategies for DC microgrid [19, 53]

2.8 Summary

Providing electricity to humanity is vital for everyday living. However, emphasis has been made to move away from fossil fuel generated electricity to RERs generated electricity to save our environment. The literature provided shows how much effort researchers have put into improving the reliability and optimality of intermittent RERs. The literature review chapter presented the important components required to implement RERs of the proposed system. The functions of components for the proposed microgrid were described based on but not limited to literature on books, conference papers, journal papers, government publications, and encyclopedias.

CHAPTER 3: SYSTEM REQUIREMENTS AND DESIGN

3.1 Introduction

This chapter describes the planning and design of the proposed microgrid. This includes finding the meteorological data of the selected location and analyzing the data to determine if the solar system application will be practical. The load demand for the microgrid will be calculated based on the rating of the appliances that will be utilized. Meteorological data and load demand will aid with the sizing of the PV arrays, BES system charge controller, and cables. Fig. 3.1 illustrates the proposed microgrid topology.

Furthermore, the proposed microgrid subgrids will be simulated on PVSyst and the sizing results obtained from PVSyst will be compared with the calculated results. The microgrid consists of 4 microgrid subgrids, each microgrid subgrid has a dedicated PV array, BES system, MPPT charge controller, and load demand. Moreover, the microgrid subgrids are all interconnected through a power-sharing bus via a bidirectional DC-DC converter which enables power-sharing amongst the microgrid subgrids. Furthermore, an energy management system will be incorporated into the design to allow optimal operation.

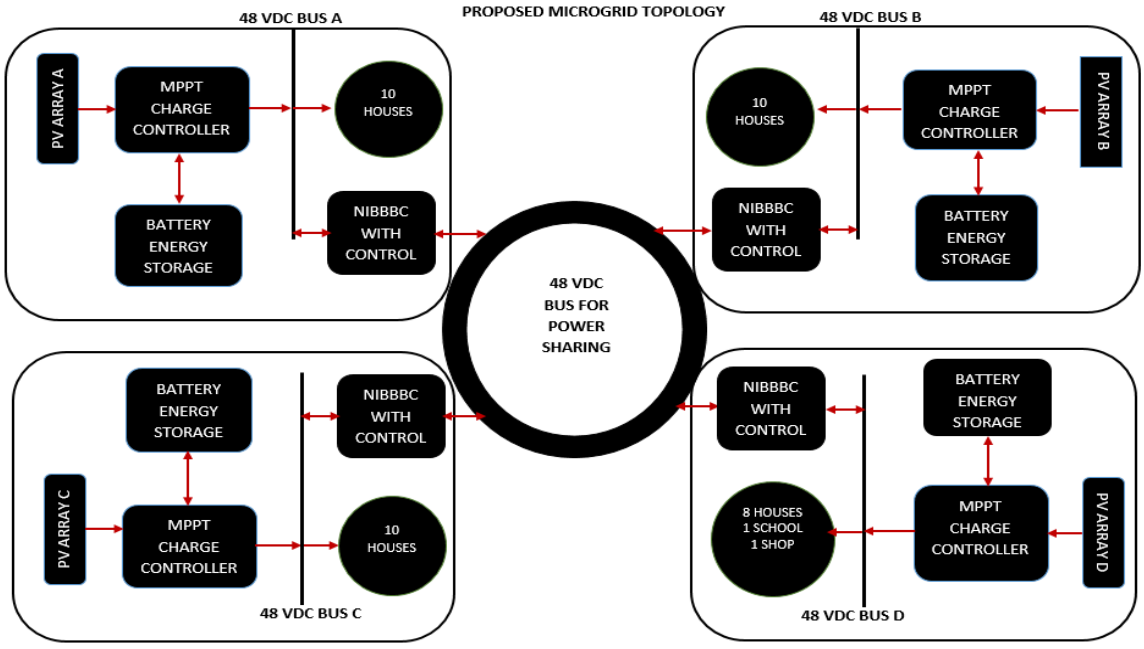

Figure 3.1 Propose microgrid topology block diagram.

3.2 PV System Location

Mhlungwana the rural village in Nquthu Ward 07, KwaZulu Natal, South Africa is the chosen location as illustrated by Fig. 3.2. The village has 651 households, of which only 12.75% (88) households have access to electricity according to StatsSA 2011 [54]. Moreover, Mhlungwana village is divided into 3 sections (A, B & C), Mhlungwana B section illustrated by Fig. 3.3 consists of 216 households with 0% of the households having access to electricity according to StatsSA 2011 [54].

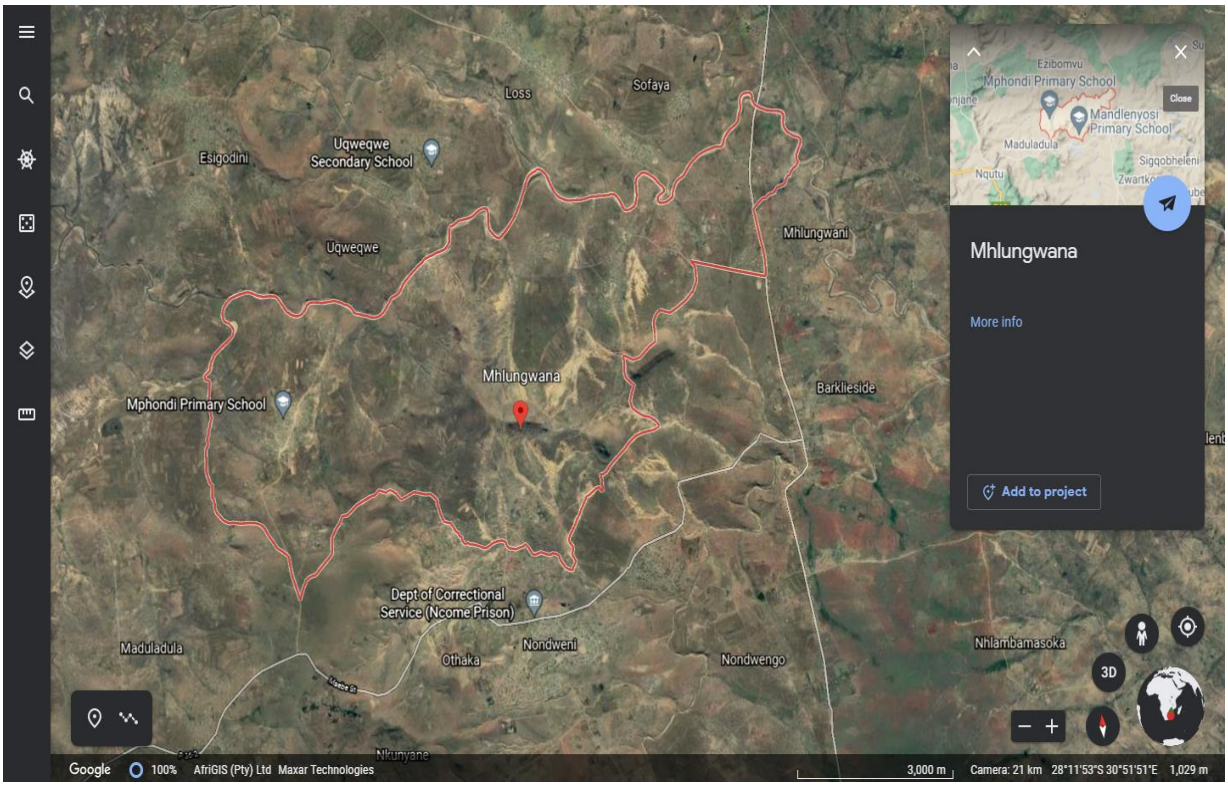

Figure 3.2 Mhlungwana village, Nquthu ward 07, KwaZulu Natal – Google Earth [55].

Figure 3.3 Mhlungwana village, Mhlungwane B section – Google Earth [55] .

3.3 Meteorological Data

Mhlungwana village has a longitude of 30.4852 East, a latitude of 28.0856 South, and an altitude of 1055m above sea level [55]. The meteorological data of Mhlungwana is shown in Table 3.1. The village has an annual average daily GHI (Global Horizontal Irradiance) of 4.89 KWh/m^2, average air temperature of 17.22 ℃ and average wind speed of 2.76 m/s [56].

Table 3.1 Mhlungwana village meteorological data [56].

Region: Africa		**Location Co-ordinates**		
Country: South Africa		**Latitude: -28.0856**		
Location: Nquthu, Ward 07, Mhlungwana		**Longitude: 30.4852** **Altitude: 1055 m**		
MONTH	**Daily GHI** KWh/m^2	**Monthly GHI** KWh/m^2	**Air Temperature** ℃	**Wind Speed** m/s
January	5.41	167.61	21.02	2.97
February	5.93	166	21.86	2.5
March	5.17	160.12	19.78	2.79
April	4.51	135.36	15.66	2.37
May	4.05	125.41	15.56	2.19
June	3.71	111.27	12.52	2.78
July	3.9	120.8	12.25	2.61
August	4.41	136.83	12.11	2.81
September	5.11	153.35	17.79	3.08
October	4.87	150.87	17.02	3.19
November	5.8	173.96	19.2	2.86
December	5.77	178.87	22.2	2.99
Year Av.	4.89	148.37	17.22	2.76

3.4 Daily Load Requirements

The proposed PV system will be designed to cater to 38 households, 1 school, and 1 small shop. The users will be divided into 5 distinct categories, each category has a distinct daily load demand as illustrated by Table 3.2-3.6. Table 3.7 illustrates the allocation of categories per microgrid subgrid (A-D) and total daily demand per microgrid subgrid.

Table 3.2 Category 1 load demand.

No.	Appliance	Power (w)	Total power (w)	Daily use (h)	Daily Energy (Wh/day)
8	LED Lights	6	48	12	576
2	Cell Recharge	5	10	3	30
1	Radio	10	10	12	120
1	TV	30	30	10	300
Total			**98**		**1026**
20% System losses					**205.2**
Total daily demand					**1231.2**

Table 3.3 Category 2 load demand.

No.	Appliance	Power (w)	Total power (w)	Daily use (h)	Daily Energy (Wh/day)
8	LED Lights	6	48	12	576
2	Cell Recharge	5	10	3	30
1	Radio	10	10	12	120
1	TV	30	30	10	300
1	Fan	40	40	12	480
Total			**138**		**1506**
20% System losses					**301.2**
Total daily demand					**1807.2**

Table 3.4 Category 3 load demand.

No.	Appliance	Power (w)	Total power (w)	Daily use (h)	Daily Energy (Wh/day)
8	LED Lights	6	48	12	576
2	Cell Recharge	5	10	3	30
1	Radio	10	10	12	120
1	TV	30	30	10	300
1	Fan	40	40	12	480
1	Fridge	90	90	12	1080
Total			**228**		**2586**
20% System losses					**517.20**
Total daily demand					**3103.20**

Table 3.5 Category 4 load demand for school.

No.	Appliance	Power (w)	Total power (w)	Daily use (h)	Daily Energy (Wh/day)
10	LED Lights	6	60	12	720
4	Cell Recharge	5	20	3	60
4	Fan	40	160	12	1920
Total			**240**		**2700**
20% System losses					**540**
Total daily demand					**3240**

Table 3.6 Category 5 load demand for a small shop.

No.	Appliance	Power (w)	Total power (w)	Daily use (h)	Daily Energy (Wh/day)
2	LED Lights	6	12	12	144
1	Cell Recharge	5	5	3	15
1	Refrigerator	90	90	12	1080
1	Radio	10	10	12	120
2	Fan	40	80	12	960
Total			**197**		**2319**
20% System losses					**463.8**
Total daily demand					**2782.8**

Table 3.7 Number of categories allocation to microgrid subgrids.

Microgrid subgrid	Number of Households Per Category					Total Energy Demand
	Category 1	Category 2	Category 3	Category 4	Category 5	
	Total Energy Demand for a Household in Each Category					
	1231.20 Wh/day	1807.20 Wh/day	3103.20 Wh/day	3240 Wh/day	2782.80 Wh/day	
A	4	4	2	0	0	18360
B	4	4	2	0	0	18360
C	4	4	2	0	0	18360
D	4	3	1	1	1	19472.40

3.5 PV Array Sizing

Proper PV array sizing is vital to avoid designing a system that may fail to meet the demand. The number of PV panels required to generate enough peak power is determined step by step utilizing Eq. (3.1) and (3.2) [2, 57-59]. Initially, Eq. (3.1) calculates the PV array peak power(PV_{PP}) required to meet the daily energy demand (E_L) for each microgrid subgrid. Annual average daily sun hours (ASH) of the location illustrated in Table 3.1 and the calculated energy demand (E_L) illustrated in Table 3.7 are utilized. Eq. (3.2) which determines the number of PV panels (N_{Pv}) required to generate the peak power which depends on the PV panel's nominal power (PV_{NP}) rating. The higher the power rating of the PV panel the fewer panels will be required to implement a PV array and vice versa.

Moreover, Table 3.8 illustrates the specifications of the PV panel model selected to be utilized for the implementation of the PV arrays for the microgrid subgrids [60, 61]. The PV panels are manufactured by SunPower, a world leader in high-efficiency solar panels [62]. SunPower solar panels have a 40-year performance and product warranty, a 25-year manufacture product warranty, and 92 percent retained capacity after 25 years [62]. The (E_L) value for each subgrid is calculated in section 3.4, Table 3.7, the (ASH) value is taken from section 3.3, Table 3.1 and the (PV_{NP}) value is taken from section 3.5, Table 3.8 which illustrates the PV panel specifications utilized to implement the PV array.

$$PV_{PP} = \frac{E_L}{ASH} \tag{3.1}$$

$$N_{Pv} = \frac{PV_{PP}}{PV_{NP}} \tag{3.2}$$

E_L – Average Load Daily Demand

ASH – Annual Average daily Sun hours

PV_{PP} – PV Array Peak Power

N_{Pv} – Number of PV Panels

PV_{NP} – PV Module Nomonal Power

Table 3.8 PV Module Specifications.

MAKE	**SPR-MAX3-430 BY SUNPOWER**	
ELECTRICAL SPECIFICATIONS		
Parameter	**Value**	**Units**
Nominal Power	430	W
PV Efficiency	22.7	%
V_{mpp}	70.4	V
I_{mpp}	6.11	A
V_{oc}	81.4	V
I_{sc}	6.57	A
Temperature Coef.	-0.27	%/℃
Max. Voltage	1000	V
Max. Series fuse	20	A
OPERATING CONDITIONS		
Temperature	-40 **to** +85	℃
Cell Technology	Monocrystalline Maxeon Gen 3	Cell
MECHANICAL SPECIFICATIONS		
Solar Cells	112	Cells
Solar Cells (Parallel)	1	String
Dimensions	1812x1046x40	mm
Weight	21.2	Kg

3.5.1 Microgrid subgrid A - C

$$PV_{PP} = \frac{E_L}{ASH}$$

$$= \frac{18360}{4.89}$$

$$= \mathbf{3754.60\ W}$$

$$N_{Pv} = \frac{PV_{PP}}{PV_{NP}}$$

$$= \frac{3754.60}{430}$$

$$= \mathbf{8.7 \approx 9\ Modules}$$

3.5.2 Microgrid subgrid D

$$PV_{PP} = \frac{E_L}{ASH}$$

$$= \frac{19472.40}{4.89}$$

$$= \mathbf{3982.10\ W}$$

$$N_{Pv} = \frac{PV_{PP}}{PV_{NP}}$$

$$= \frac{3982.10}{430}$$

$$= \mathbf{9.3 \approx 10\ Modules}$$

3.6 Battery Energy Storage System Sizing

The main aim of the research is to design a standalone PV system that is optimum for its users, a BES system is an essential part of the system that will assist in achieving the goal. PV array energy can only generate electrical energy during the presence of sunlight, the BES system will take over from PV arrays when there is no energy to harvest from the PV panels during the night, cloudy, and or rainy days [30]. LiFePO4 (Lithium Ferro Phosphate) battery technology was selected to implement the BES system for the microgrid subgrids.

In [63] a study was conducted to compare two battery technologies namely lead acid and lithium-ion. The comparison covers a variety of characteristics which include charging time, life cycle, maintenance, safety, recycling, capital cost, net present cost, and environmental effect. The results of the study revealed that lithium-ion battery technology is the best option which has a modest maintenance cost. It is not hazardous to the environment, has a fast charging rate, and versatile SOC. However, they are expensive, and large capital is required to source them.

Eq. (3.3) -(3.6) are utilized to determine the vital parameters for the BES system [2, 57-59]. Eq. (3.3) determines the BES system's global capacity (B_{GC}) required to meet a household's energy demand which includes 4 days of autonomy (A). Autonomy is the number of days the batteries will be able to cater for the load without being recharged. The depth of discharge (DOD) of the battery which is the usable percentage of the total rated capacity, efficiency (η_B) which is the rate of energy loss in a charge/discharge cycle, and bus voltage (V_{Bus}) of the PV system which is 48V DC are utilized in Eq. (3.3). The (DOD) and (η_B) values utilized in calculations are taken from Table 3.9 which illustrates the selected battery storage technology specifications.

$$B_{GC} = \frac{A * E_L}{DOD * \eta_B * V_{Bus}} \tag{3.3}$$

B_{GC} − Battery Global Capacity

A − Autonomy

DOD − Battery Depth of Discharge

V_{Bus} − Bus Voltage

η_B − Battery efficiency

Eq. (3.4) determines the number of batteries (N_B) required to meet the required battery global capacity. Eq. (3.5) and (3.6) determine the number of batteries to be connected in parallel (N_{BP}) and series (N_{BS}). Parallel connection increases the battery system amp-hour capacity, series connection increases battery system voltage. Table 3.9 illustrates the specifications of the selected lithium-ion battery that will be utilized to implement the BES system for each microgrid subgrid [64, 65]. (B_C) is the battery nominal capacity, (B_V) is the battery nominal voltage as illustrated in Table 3.9 and the V_{Bus} is the bus voltage value of the system being designed which is 48V DC.

$$N_B = \frac{B_{GC}}{B_C} \tag{3.4}$$

N_B − Number of Batteries

B_C − Battery nominal capacity

$$N_{BS} = \frac{V_{Bus}}{B_V} \tag{3.5}$$

N_{BS} − Number of Batteries in Series

B_V − Battery nominal voltage

$$N_{BP} = \frac{N_B}{N_{BS}} \tag{3.6}$$

N_{BP} − Number of Batteries in Parallel

Table 3.9 Battery Specifications.

MAKE	**LiFe4833P BY PowerPlus Energy**	
ELECTRICAL SPECIFICATIONS		
Parameter	**Value**	**Units**
Nominal Voltage	48	V
Nominal Power Capacity	3.3	kWh
Nominal Capacity	64	Ah
OPERATING CONDITIONS		
Continuous discharge	0.5 (C2)	C
Maximum Charging Current	63	A
Maximum discharging Current	32	A
Charge Cut-Off Voltage	58.4	V
Discharge Cut-Off Voltage	40	V
Temperature Charge	0 to 55	℃
Temperature Discharge	-20 to 55	℃
Minimum Charging Temp.	0.0	℃
Minimum Discharging Temp.	-20	℃
Efficiency	>96	**%**
Operating Humidity	85	%
Shutdown SOC recommended	20	%
Battery Technology	Lithium Ferro Phosphate	cells
MECHANICAL SPECIFICATIONS		
Dimensions	635D x 434W x 88H	mm
Weight	41	kg

3.6.1 EqMicrogrid subgrid A- C

$$B_{GC} = \frac{A * E_L}{DOD * \eta_B * V_{Bus}}$$

$$= \frac{4 * 18360}{0.8 * 0.97 * 48}$$

$$= 1971.65\ \boldsymbol{Ah}$$

$$N_B = \frac{B_{GC}}{B_C}$$

$$= \frac{1971.65}{64}$$

$$= 30.8 \approx \textbf{30 Batteries}$$

$$N_{BS} = \frac{V_{Bus}}{B_V}$$

$$= \frac{48}{48}$$

$$= \mathbf{1}$$

$$\approx \mathbf{1\ Battery\ in\ series}$$

$$N_{BP} = \frac{N_B}{N_{BS}}$$

$$= \frac{30.8}{1}$$

$$= \mathbf{30.8}$$

$$\approx \mathbf{30\ Batteries\ in\ Parallel}$$

3.6.2 Microgrid subgrid D

$$B_{GC} = \frac{A * E_L}{DOD * \eta_B * V_{Bus}}$$

$$= \frac{4 * 19472.40}{0.8 * 0.97 * 48}$$

$$= \mathbf{2091.11\ Ah}$$

$$N_B = \frac{B_{GC}}{B_C}$$

$$= \frac{2091.11}{64}$$

$$= \mathbf{32.67}$$

$$\approx \mathbf{33\ Batteries}$$

$$N_{BS} = \frac{V_{Bus}}{B_V}$$

$$= \frac{48}{48}$$

$$= \mathbf{1}$$

$$\approx \mathbf{1\ Battery\ in\ series}$$

$$N_{BP} = \frac{N_B}{N_{BS}}$$

$$= \frac{32.67}{1}$$

$$= \mathbf{32.67}$$

$$\approx \mathbf{33\ Batteries\ in\ Parallel}$$

3.7 Sizing MPPT Charge Controller

A charge controller plays a vital role in protecting the batteries from overcharging and over-discharging [31]. An MPPT charge controller design will be utilized for the proposed system. When selecting a charge controller two important aspects need to be considered, the current rating, and the voltage rating [2, 57-59]. The current rating of the charge controller needs to be greater than or equal to the load maximum current, the charge controller minimum current rating ($CC(I_R)$) is calculated utilizing Eq. (3.7). N_P represent the number of PV panels connected in parallel which

is 9 for subgrid A-C and 10 for subgrid D, $PV(I_{SC})$ represent the PV panel short circuit current illustrated in Table (3.8) and k represent the safety factor of 1.25 for the charge controller.

Furthermore, the voltage rating needs to be greater than or equal to the bus voltage and the charge controller minimum voltage rating ($CC(V_R)$) calculated utilizing Eq. (3.8) [2, 57-59]. N_S represent the number of series connected PV panels of the array which is 1 for the designed system and $PV(V_{OC})$ represent the PV array open circuit voltage illustrated in Table 3.8. Eq. 3.9 calculates the number of charge controllers (N_{CCP}) required for each subgrid, I_{Max} represents the charge controller maximum input current rating illustrated in Table (3.10).

Moreover, Table (3.10) outlines the specifications of the selected charge controllers that will be utilized for each microgrid subgrid [66, 67]. SmartSolar MPPT charge controller manufactured by Victron Energy had high ratings as stated by clean energy reviews in 2022 [68]. Furthermore, Eqs. (3.7) -(3.9) are utilized to determine the charge controller's current and voltage minimum ratings, and the number of parallel connected charge controllers required [2, 57-59].

$$CC(I_R) = N_P * PV(I_{SC}) * k \tag{3.7}$$

$$CC(V_R) = N_S * PV(V_{OC}) * k \tag{3.8}$$

$$N_{CCP} = \frac{CC(I_R)}{I_{Max}} \tag{3.9}$$

$CC(I_R)$ – Charge Controller Minimum Current Rating
$CC(V_R)$ – Charge Controller Minimum Voltage Rating
N_{CCP} – Number of parallel connected charge controllers
I_{Max} – Charge Controller Maximum input current
N_S – Number of series connected PV Panels
N_P – Number of Parallel connected PV Panels
$PV(I_{SC})$ – PV Panel Short Circuit Current
$PV(V_{OC})$ – PV Array Open Circuit Voltage
k – Safety Coefficient 1.25

Table 3.10 MPPT Charge Controller Specifications.

MAKE	**SmartSolar MPPT 150/45 BY VICTRON ENERGY**	
ELECTRICAL SPECIFICATIONS		
Parameter	**Value**	**Units**
Battery Voltage	48	V
Nominal PV Power	2600	W
Max. PV V_{OC}	150	V
Max. PV I_{SC}	50	A
OPERATING CONDITIONS		
Temperature	-30 to +60	℃
Humidity	95	%
Efficiency	98	%
MECHANICAL SPECIFICATIONS		
Dimensions	130H x 186W x 70D	mm
Weight	1.25	Kg

3.7.1 Microgrid subgrid A – C

$$CC(I_R) = N_P * PV(I_{SC}) * k$$

$$= 9 * 6.57 * 1.25$$

$$= \mathbf{74.91\ A}$$

$$CC(V_R) = N_S * PV(V_{OC}) * k$$

$$= 1 * 81.4 * 1.25$$

$$= \mathbf{101.8\ V}$$

$$N_{CCP} = \frac{CC(I_R)}{I_{Max}}$$

$$= \frac{74.91}{50}$$

$$= \mathbf{1.5 \approx 2\ parallel\ controllers}$$

Two parallel connected MPPT charge controllers with a minimum voltage rating above 101.8V, a maximum input current above or equal to the minimum current rating of 74.91 A and the charge current rating above 80.63 A have to be utilized for subgrid A-C. The charge current value was calculate utilizing the maximum power generated by the PV array and the systems bus voltage rating.

3.7.2 Microgrid subgrid D

$$CC(I_R) = N_P * PV(I_{SC}) * k \qquad CC(V_R) = N_S * PV(V_{OC}) * k$$

$$= 10 * 6.57 * 1.25 \qquad = 1 * 81.4 * 1.25$$

$$= \mathbf{82.12\ A} \qquad = \mathbf{101.8\ V}$$

$$N_{CCP} = \frac{CC(I_R)}{I_{Max}}$$

$$= \frac{82.12}{50}$$

$$= \mathbf{1.6 \approx 2\ parallel\ controllers}$$

Two parallel connected MPPT charge controllers with a minimum voltage rating above 101.8V, a maximum input current above or equal to the minimum current rating of 82.12 A and the charge current rating above 89.58 A have to be utilized for subgrid D. The charge current value was calculate utilizing the maximum power generated by the PV array and the systems bus voltage rating.

3.8 PVSYST vs. Calculation Results for PV Array and Battery Storage Sizing

Table 3.11 shows the comparison between the calculated and PVSyst simulated results of the PV system design. The results include daily demand, peak power, PV array sizing, and battery sizing. The PVSyst suggested results are more or less similar to calculated results for PV array peak power and daily energy demand. However, the PVSyst suggested battery global capacity and number of batteries required to meet the suggested demand differ.

The difference is caused by the fact that an estimated 20% of DC losses were considered when calculations were done which covers all possible aspects of losses that may occur including but not limited to PV array losses, DC-DC converter losses, DC cable losses, which differ from the losses that are assigned by PVSyst based on the PV module characteristics, converter characteristics, and battery technology characteristics. The difference between the loss estimated

for calculations and PVSyst suggested loss caused the battery storage system design results to be different.

Table 3.11 PVSyst results vs. calculated results of the microgrid subgrids.

	SUBGRID							
	A-C				D			
PV ARRAY	**DAILY ENERGY DEMAND**							
	CALCULATED		PVSYST		CALCULATED		PVSYST	
	15300 W		15300 W		16227 W		16227 W	
	PV ARRAY PEAK POWER							
	3754.60 W		3755 W		3982.10 W		3975 W	
	PV PANEL NOMINAL POWER							
	430 W				430 W			
	NUMBER OF PV PANELS							
	9		9		10		9	
BATTERY STORAGE	**BATTERY CAPACITY**							
	64 Ah				64 Ah			
	GLOBAL CAPACITY							
	CALCULATED		PVSYST		CALCULATED		PVSYST	
	1971.65 Ah		1406 Ah		2091.11 Ah		1491 Ah	
	NUMBER OF BATTERIES							
	CALCULATED		PVSYST		CALCULATED		PVSYST	
	String	Parallel	String	Parallel	String	Parallel	String	Parallel
	1	30	1	22	1	33	1	24

3.9 Cable Sizing

Cable size selection is a vital step to avoid oversizing and undersizing cables. Inefficient cable sizing can lead to large losses, immoderate heat, and fire when the cable is undersized while oversizing is a waste of money. For efficient energy distribution, cable length and cross-sectional area need to be properly determined, cable length (C_L)can be determined by physically measuring the distance between the components of the system, and the cable cross-sectional area (C_A) can be determined by utilizing Eq. (3.10) [59]. ρ represent the copper cable standard resistivity at 20℃ is $1.72x\ 10^{-8}\ m\ \Omega$, this is the measure of how much the copper cable opposes the flow of electrical current through it. Furthermore, cable cross-sectional area may vary in distinct locations of the

system since the current varies with location. Cables need to be water resistant and UV-protected [59].

$$C_A = \frac{C_L * \rho * I_c}{V_D} \text{ x } 2 \quad \textbf{(3.10)}$$

C_A – Cable cross sectional area
ρ – Cable resistivity
C_L – Cable length
I_C – Cable Maximum current
V_D – Cable Voltage drop

Figure 3.4 Microgrid subgrid A, B, C & D locations

Fig. 3.4 illustrates the location of the microgrid subgrids and the households that will be connected to each microgrid subgrid. The distance between each microgrid subgrid and households was determined through Google Maps and listed in Table 3.15. Table 3.12 illustrates the maximum current rating for location 1 (between PV array and DC-DC converter) and location 2 (Between DC-DC converter and BES) for each microgrid subgrid. The voltage drop across all cables was kept at 2%, the voltage drop recommended [69]. Table 3.13 illustrates the 2% voltage drop value, the calculated cable cross-sectional area, and the standard cable cross-sectional area. The standard

cross-sectional area for the cable was selected based on the chart [70] to conform with the SANS 10142-1 compulsory wiring specifications.

Furthermore, maximum current ratings for each category were determined and listed in Table 3.14. The maximum current rating, distance, and an allowable voltage drop of (V_D) 2% were utilized to determine the cross-sectional area for the wire required. Table 3.15 illustrates the length of the cable, the 2% voltage drop value and the cross-sectional area for cables between the microgrid subgrids and households.

Table 3.12 Maximum current ratings for locations 1 and 2.

Microgrid subgrid	Location 1	Maximum current	Location 2	Maximum current
A	PVA1 to DC-DC Conv.	73.91	DC-DC Conv. to BES	100
B	PVA2 to DC-DC Conv.	73.91	DC-DC Conv. to BES	100
C	PVA3 to DC-DC Conv.	73.91	DC-DC Conv. to BES	100
D	PVA4 to DC-DC Conv.	82.12	DC-DC Conv. to BES	100

Table 3.13 Cross-sectional area and voltage drop percentage for locations 1 and 2

Microgrid subgrid	Location 1			
	Distance(m)	CCSA (mm^2) Calculated	CCSA (mm^2) Selected	VD 2%
A-C	10	15.61	25	0.96
D	10	17.35	25	0.96
	Location 2			
A-C	10	35	35	0.96
D	10	35	35	0.96

Table 3.14 Maximum current ratings for location 3

Category	Location 3	Maximum Current
1	Microgrid subgrid – Household	25.65
2	Microgrid subgrid – Household	37.65
3	Microgrid subgrid – Household	91.65
4	Microgrid subgrid – Household	67.5
5	Microgrid subgrid – Household	84.98

Table 3.15 Cross-sectional area and voltage drop for location 3.

Location 3										
A										
Household	**1**	**2**	**3**	**4**	**5**	**6**	**7**	**8**	**9**	**10**
Distance	50	52	55	82	97	141	146	159	161	183
CATEGORY	3	3	2	2	2	2	1	1	1	1
VD 2%	0.96	0.96	0.96	0.96	0.96	0.96	0.96	0.96	0.96	0.96
Calculated Cable Cross Sectional Area										
CCSA (mm^2)	160.4	166.8	72.5	108.1	127.8	185	131.1	142.7	144.5	164.3
Selected Standard Cable Cross sectional Area close to the calculated value										
CCSA (mm^2)	185	185	95	120	150	185	150	150	150	185
B										
Distance(m)	39	46	77	86	91	123	148	154	156	161
CATEGORY	3	3	2	2	2	2	1	1	1	1
VD 2%	0.96	0.96	0.96	0.96	0.96	0.96	0.96	0.96	0.96	0.96
Calculated Cable Cross Sectional Area										
CCSA (mm^2)	125.1	147.6	101.5	113.3	119.9	162.1	132.9	138.3	140.1	144.5
Selected Standard Cable Cross sectional Area close to the calculated value										
CCSA (mm^2)	150	150	120	120	120	185	150	150	150	150
C										
Distance(m)	21	35	53	71	74	101	105	115	121	132
CATEGORY	3	3	2	2	2	2	1	1	1	1
VD 2%	0.96	0.96	0.96	0.96	0.96	0.96	0.96	0.96	0.96	0.96
Calculated Cable Cross Sectional Area										
CCSA (mm^2)	67.4	112.3	69.8	93.6	97.5	133.1	94.3	103.2	108.6	118.5
Selected Standard Cable Cross sectional Area close to the calculated value										
CCSA (mm^2)	**70**	**120**	**70**	**95**	**120**	**150**	**95**	**120**	**120**	**120**
D										
Distance(m)	46	53	62	72	91	104	133	149	156	199
CATEGORY	3	5	4	2	2	2	1	1	1	1
VD 2%	0.96	0.96	0.96	0.96	0.96	0.96	0.96	0.96	0.96	0.96
Calculated Cable Cross Sectional Area										
CCSA (mm^2)	147.6	157.6	146.5	94.9	119.9	137.1	119.4	133.8	140.1	178.7
Selected Standard Cable Cross sectional Area close to the calculated value										
CCSA (mm^2)	150	185	150	95	120	150	120	150	150	185

3.10 Summary

Proper sizing and choice of location are vital for designing an optimal microgrid system [17]. In this chapter, the location meteorological data was presented and it aided the sizing of system components required to implement the proposed microgrid subgrids. The subgrids were also simulated on PVSyst to compare the results obtained with calculated results.

.

CHAPTER 4 SYSTEM DESIGN AND SIMULATION MODELLING.

4.1 Introduction

This chapter focuses on the design and Matlab/Simulink model simulation of the proposed system components. The proposed distributed PV array system will comprise various stages with different but vital functions which are the PV array, non-isolated DC-DC converters, BES, and the energy management system for power-sharing. Moreover, the microgrid including all the components will be simulated, all simulation results and discussion are presented in Chapter 5.

Furthermore, the aim is to provide a RE system that is optimum for users. PV arrays will be the source of RE, the buck-boost DC-DC converter will link the PV array and the system bus regulating the source voltage to 48V DC. Since PV energy can only be harvested during the presence of solar radiation, a BES system and the power sharing management system will be utilized to supplement the system's demand during low or absent solar radiation periods.

4.2 Buck – Boost Converter

The non-isolated unidirectional DC-DC converter that links the PV array and the local bus will be designed to operate in two modes (Buck or Boost) independently. When the PV array sourced voltage is greater than the required bus voltage the buck-boost will operate as a buck converter and when the PV array sourced voltage is less than the required bus voltage the buck-boost will operate as the boost converter regulating the system bus voltage to 48V DC. In [71-79] different DC-DC converters are explored in terms of design and operation, the following sub sections explain the operation of the buck and boost DC-DC converters separately.

Eqs. (4.1) and (4.2) will be applied in the following sections to derive the important parameters of the DC-DC converter. Eq. (4.1) expresses the voltage across the inductor which is directly proportional to the rate of change of current passing through it [80, 81]. Eq. (4.2) expresses capacitor current which is directly proportional to the rate of change of voltage [81].

$$V_L = L\frac{di_L}{dt} \quad \textbf{(4.1)}$$

$$i_c = C\frac{dV_{out}}{dt} \quad \textbf{(4.2)}$$

L – Inductor
V_L – Voltage across the inductor
i_{D0} – Current passing through the Inductor
C – Capacitor
i_c – Capacitor current
V_{out} – Output voltage

4.2.1 Buck Converter

The buck converter is a DC-DC voltage converter with an output voltage that is less than the input voltage [71, 73, 75]. Fig. 4.1(a) shows an asynchronous non-isolated buck converter circuit diagram with the MOSFET switch (S) as a controlled switch and diode (D0) as an uncontrolled switch. The operation of the buck converter circuit can be analyzed based on two states (ON and OFF). The ON state is represented by Fig. 4.1(b), when S is switched on for the *DT* period, the input current flows through the switch, inductor, capacitor, and load. The OFF state is represented by Fig. 4.1(c), when S is switched off for a period of (*1- D)T* the inductor discharges for a continuous flow of current to the load through freewheeling diode **(**D0) [82].

T – Switching period
D – Duty Cycle
DT – Switch ON period
(1 – D)T – Switch OFF period

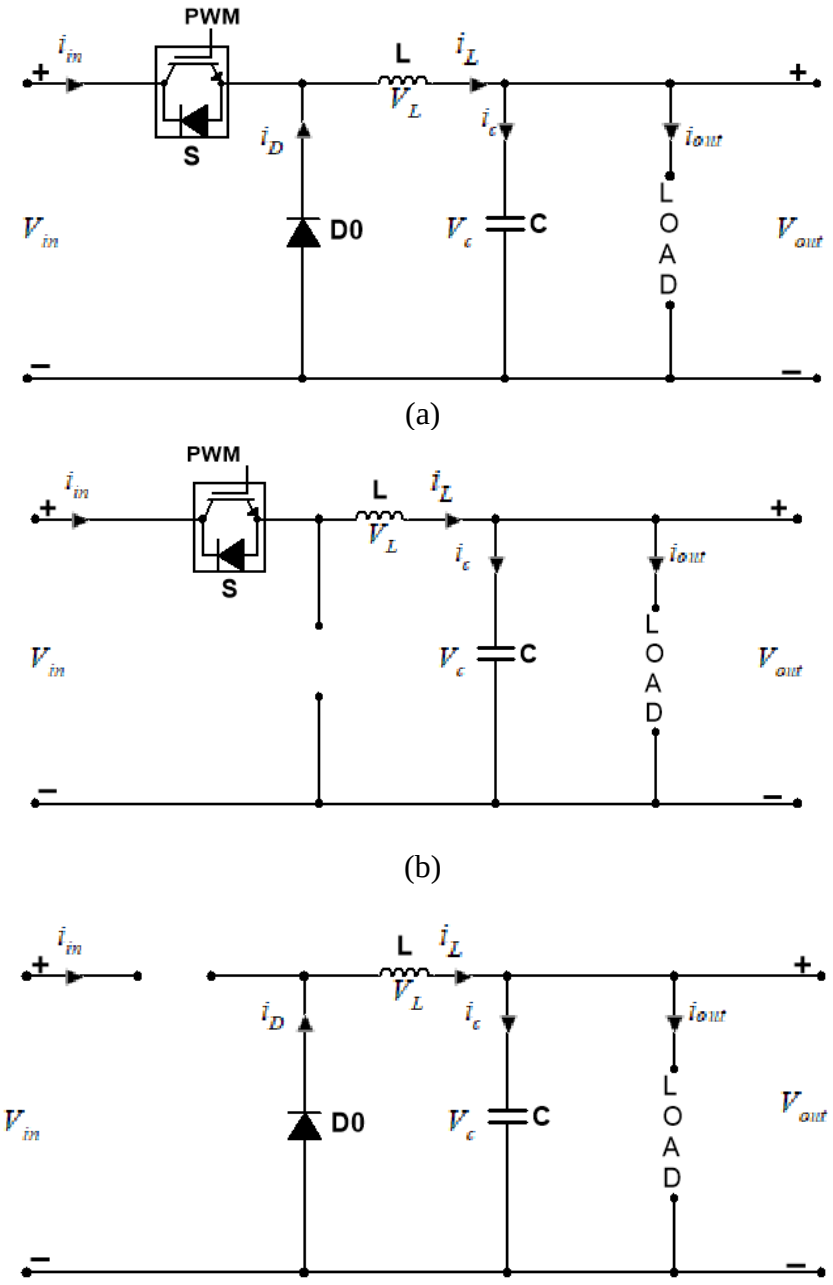

Figure 4.1 (a) Buck converter conventional circuit, (b) Buck converter ON state, (c) Buck converter OFF state.

4.2.1.1 Buck Converter Parameters

On-Time Change in Inductor Current

During the ON state as illustrated by Fig. 4.1 (b), the voltage across the inductor (V_L) is expressed with Eq. (4.3) when applying Kirchhoff's Voltage Law (KVL) [81]. During this state, the inductor is charged, and the current flows to the capacitor and load. Assumptions are made that the inductor current rises linearly for a continuous flow of current to the load, Eq. (4.3) is substituted into Eq. (4.1) to derive the change in inductor current (Δi_L) during the ON state and is expressed in Eq. (4.6).

$$V_L = V_{in} - V_{out} \tag{4.3}$$

$$\frac{di_L}{dt} = \frac{V_L}{L} = \frac{V_{in} - V_{out}}{L} \tag{4.4}$$

$$\Delta i_L = \int_0^{DT} \frac{V_L}{L} dt \tag{4.5}$$

$$\Delta i_L = \frac{V_{in} - V_{out}}{L} * DT \tag{4.6}$$

V_{in} – Input voltage
Δi_L – Change in inductor current

Off-Time Change in Inductor Current

During the OFF state, the voltage across the inductor when switch S is switched OFF as shown in Fig. 4.1 (c), is expressed with Eq. (4.7) when applying KVL. The current discharged by the inductor has reversed polarity, this can be explained by Lenz's law. Lenz's law states that an induced current flows in the direction that opposes the change in the circuit that produces it [83]. The discharged current flows to the load and through forward biased diode D0. Assumptions are made that the inductor current drops linearly and Eq. (4.8) is utilized to find the change in inductor current (Δi_L) during the OFF state and expressed in Eq. (4.10).

$$0 = V_L + V_{out}$$

$$V_L = -V_{out} \tag{4.7}$$

$$L\frac{di_L}{dt} = -V_{out} \tag{4.8}$$

$$\frac{di_L}{dt} = \frac{-V_{out}}{L}$$

$$\Delta i_L = \int_{DT}^{T} \frac{-V_{out}}{L}\, dt \tag{4.9}$$

$$\Delta i_L = -\frac{V_{out}}{L} * (1 - D)T \tag{4.10}$$

Peak-to-Peak Change in Inductor Current

The total switching period (T) for the buck converter is the sum of the ON switching period and the OFF switching period as expressed by Eq. (4.11). Utilizing Eqs. (4.6) and (4.10), DT and $(1 - D)T$ are derived and substituted as expressed in Eq. (4.12). The peak-to-peak change in inductor current is derived from Eq. (4.12) and expressed by Eq. (4.13).

$$T = DT + (1 - D)T \tag{4.11}$$

$$T = \frac{\Delta i_L L}{V_{in} - V_{out}} + \frac{\Delta i_L L}{V_{out}} \tag{4.12}$$

$$= \frac{\Delta i_L L V_{in}}{V_{out}(V_{in} - V_{out})}$$

$$\Delta i_L = \frac{V_{out}(V_{in} - V_{out})}{fLV_{in}} \tag{4.13}$$

f – Switching frequency

Peak-to-Peak Capacitor Ripple Voltage

The equation for capacitor ripple voltage (Δv_c) is expressed in Eq. (4.14). The capacitor (C) charges during the last half of the ON state and begins to discharge during the first half of the OFF state of the power transistor of the buck converter [82]. Eq. (4.15) is utilized to derive the capacitor change in charge (ΔQ) for the buck converter. Substituting Eq. (4.13) into Eq. (4.16) and substituting the results into Eq. (4.14), the capacitor ripple voltage can be expressed in Eq. (4.18) [80].

Furthermore, Fig. 4.2 illustrates the charging and discharging of the capacitor. When the inductor current is above average voltage, the capacitor charges and when it is below average, the capacitor discharges. Steady state operation is assumed which means the amount of charge sent to the capacitor is equal to the amount of charge taken from the capacitor. The capacitor's discharge area is utilized to calculate the change in charge in Eq.(4.15) [84, 85].

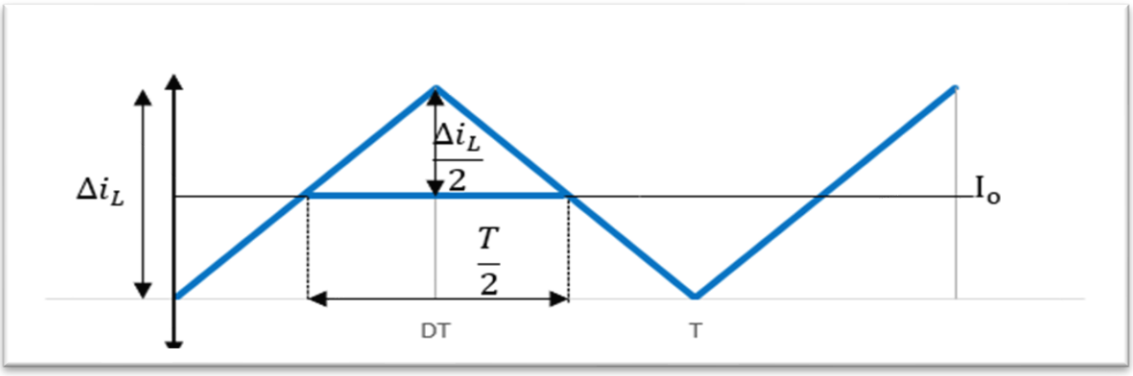

Figure 4.2 Inductor Current Waveform

$$\Delta v_c = \frac{\Delta Q}{C} \tag{4.14}$$

$$\Delta Q = \Delta Area = \frac{1}{2} h * b \tag{4.15}$$

$$\Delta Q = \frac{1}{2} * \frac{\Delta i_L}{2} * \frac{T}{2}$$

$$= \frac{\Delta i_L T}{8} = \frac{\Delta i_L}{8f} \tag{4.16}$$

$$\Delta Q = \frac{V_{out}(V_{in} - V_{out})}{8f^2 L V_{in}} \tag{4.17}$$

$$\Delta v_c = \frac{V_{out}(V_{in} - V_{out})}{8LCf^2 V_{in}} \tag{4.18}$$

Output Voltage and Duty Cycle

The buck converter output voltage is expressed in Eq. (4.20) and the duty cycle is expressed in Eq. (4.21). These equations are derived based on the inductor voltage-second balance, assuming steady state operation and continuous conduction mode. When the converter is operating in a steady state operation, the sum of the voltage across the inductor during the ON state, and the OFF state is zero [80, 82]. Since the voltage across the inductor is directly proportional to the rate of change of current passing through it, as expressed by Eq. (4.1), Eq. (4.19) represents the voltage-second balance of the inductor which is utilized to derive the output voltage and duty cycle equations.

Voltage-second Balance

$$\Delta i_L(ON\ Time) + \Delta i_L(OFF\ Time) = 0 \quad \textbf{(4.19)}$$

$$\frac{(V_{in} - V_{out}) * DT}{L} + \frac{(-V_{out}) * (1 - D)T}{L} = 0$$

$$V_{in} * D - V_{out} * D = V_{out} - V_{out} * D$$

$$V_{out} = V_{in} * D \quad \textbf{(4.20)}$$

$$D = \frac{V_{out}}{V_{in}} \quad \textbf{(4.21)}$$

4.2.2 Boost Converter

The boost converter is a DC-DC voltage converter with an output voltage that is greater than the input voltage [71-73, 78]. Fig. 4.3(a) illustrates the asynchronous non-isolated boost converter circuit diagram, S represents the MOSFET which is the controlled switch and the diode (D0) is the uncontrolled switch. The boost converter is a switching circuit, its operation is divided into two States (ON and OFF). The first state (ON) is represented by Fig. 4.3(b), when S is switched ON for a period of *DT* the input current flows through the inductor (L) and switch (S). The second state (OFF) is represented by Fig. 4.3(c) when S is switched OFF for a period of *(1- D)T* the inductor is discharged acting as a source in conjunction with the input source which maintains the flow of current to the load through the freewheeling diode (D0) [82].

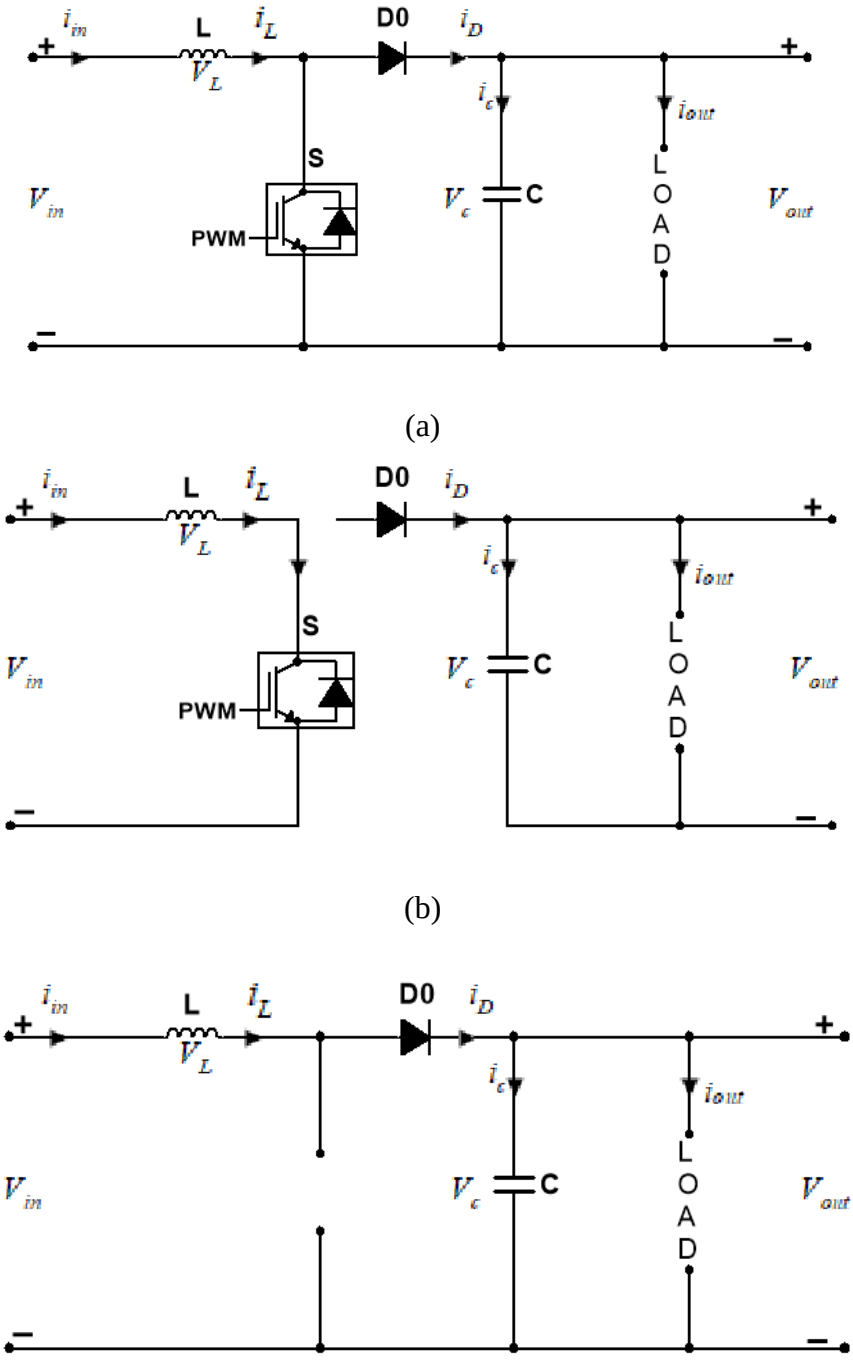

Figure 4.3 (a) Boost converter circuit diagram, (b) Boost converter ON state, (c) Boost converter OFF state.

4.2.2.1 Boost Converter Parameters

On-Time Change in Inductor Current

During switch S ON state the inductor voltage is equal to the input voltage, expressed in Eq. (4.22) when applying KVL. Since our DC-DC converter design will have a continuous flow of current to the load, the current through the inductor is assumed to be rising linearly. The inductor ripple current (Δi_L) during the switch S ON state can be derived from substituting Eq. (4.22) into Eq. (4.1) and expressed with Eq. (4.24).

$$V_L = V_{in} \tag{4.22}$$

$$\frac{di_L}{dt} = \frac{V_L}{L} = \frac{V_{in}}{L} \tag{4.23}$$

$$\Delta i_L = \int_0^{DT} \frac{V_{in}}{L} dt = \frac{V_{in}}{L} * DT \tag{4.24}$$

Off-Time Change in Inductor Current

During the OFF state of switch S, the inductor voltage (V_L) is expressed with Eq. (4.25) when applying KVL. Eq. (4.26) is derived from substituting Eqs. (4.25) into Eq. (4.1). The current through the inductor is assumed to be falling linearly and can be derived from Eq. (4.26). Utilizing Eq. (4.26) the inductor ripple current (Δi_L) during the OFF state can be derived and expressed by Eq. (4.28).

$$V_L = V_{in} - V_{out} \tag{4.25}$$

$$\frac{di_L}{dt} = \frac{V_L}{L} = \frac{V_{in} - V_{out}}{L} \tag{4.26}$$

$$\Delta i_L = \int_{DT}^{T} \frac{V_{in} - V_{out}}{L} dt \tag{4.27}$$

$$= \frac{V_{in} - V_{out}}{L} * (1 - D)T \tag{4.28}$$

Peak-to-Peak Change in Inductor Current

The inductor ripple current Eqs. (4.24 & 4.28) are utilized to derive DT and $(1 - D)T$ equations as expressed in Eq. (4.29). Utilizing Eq. (4.29) the peak-to-peak inductor ripple current is derived and expressed with Eq. (4.30).

$$T = DT + (1 - D)T \tag{4.29}$$

$$= \frac{\Delta i_L L}{V_{in}} + \frac{\Delta i_L L}{V_{out} - V_{in}}$$

$$= \frac{\Delta i_L L V_{out}}{V_{in}(V_{out} - V_{in})}$$

$$\Delta i_L = \frac{V_{in}(V_{out} - V_{in})}{f L V_{out}} \tag{4.30}$$

Peak-to-Peak Capacitor Ripple Voltage

The conventional equation for capacitor ripple voltage (Δv_c) is expressed in Eq. (4.31). The change in charge (ΔQ) is calculated by Eq. (4.32). Substituting Eq. (4.33) into Eq. (4.31) will result in Eq. (4.35) which expresses the peak-to-peak capacitor ripple voltage. Moreover, Fig. 4.4 illustrates the charging and discharging of the output capacitor of the boost converter. When the diode current (i_D) is below average the capacitor discharges and when the diode current is above average the capacitor charges. Steady state operation is assumed and the amount of charge sent to the capacitor is equal to the amount of charge taken from the capacitor. The capacitor's discharge area is utilized to calculate the change in charge in Eq. (4.32) [86, 87].

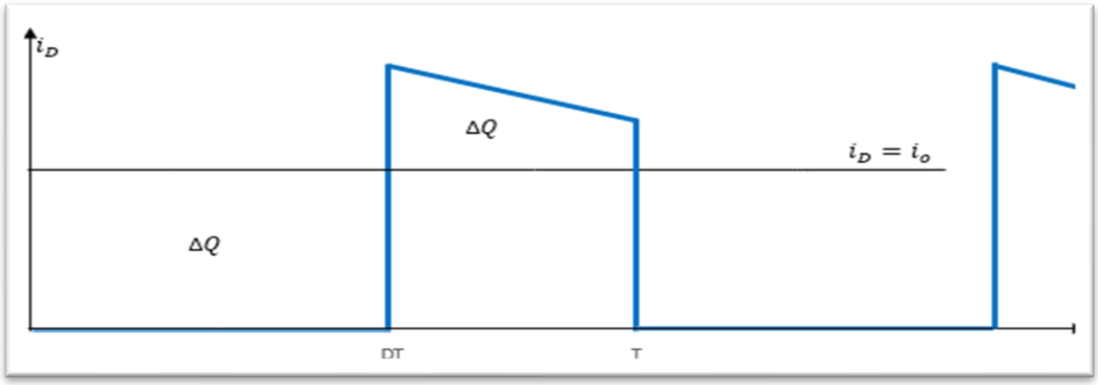

Figure 4.4 Boost Converter Diode Current Waveform

$$\Delta v_c = \frac{\Delta Q}{C} \tag{4.31}$$

$$\Delta Q = Area\ of\ rect. \tag{4.32}$$

$$= w * l$$

$$= i_D * DT \tag{4.33}$$

$$\Delta v_c = \frac{i_{out}}{C} * DT \tag{4.34}$$

$$= \frac{i_{out} * D}{fC} \tag{4.35}$$

i_D – Current across the diode
w – current across the diode value
l – ON switching period value

Average Output Voltage and Duty Cycle

The boost converter output voltage expressed in Eq. (4.37) and duty cycle expressed in Eq. (4.38) is derived from the inductor voltage-second balance from Eqs. (4.24) and (4.28) when steady state operation is assumed.

$$\Delta i_L(ON\ State) + \Delta i_L(OFF\ State) = 0 \tag{4.36}$$

$$\frac{V_{in}}{L} * DT + \frac{V_{in} - V_{out}}{L} * (1 - D)T = 0$$

$$V_{in} * D = -V_{in} + V_{out} + D * V_{in} - D * V_{out}$$

$$V_{out} = \frac{V_{in}}{1 - D} \tag{4.37}$$

$$D = \frac{V_{out} - V_{in}}{V_{out}} \tag{4.38}$$

4.3 Small signal Modeling

The small signal modeling approach was applied to the buck and boost operations of the Buck-Boost converter. This approach enables a designer to analyze how small variations of the input voltage, current, and duty cycle affect the output voltage utilizing transfer functions [88, 89]. Transfer functions are further utilized to design feedback control. Sections 4.3.1 and 4.3.2 cover the small signal modeling of the buck and boost operations of the non-isolated unidirectional buck-boost converter.

Moreover, steps were followed to derive the small signal model of the buck and boost operations of the converter.

I. **Step 1** – This step includes deriving inductor voltage and capacitor current equations during the ON and OFF states as expressed by Eqs. (4.1), (4.7), (4.22), (4.25), (4.39), (4.40), (4.45) and (4.46). These equations are utilized in stage 2 to determine the steady state operation of the converter.

II. **Step 2** – Averaging inductor voltage by applying inductor voltage sec balance and averaging the capacitor current by applying capacitor charge balance, expressed by Eqs. (4.41), (4.43), (4.47) and (4.49). This stage determines the steady state operating point of the converter.

III. **Step 3** – Perturbation is a small variation from a known or assumed value often around steady state operating point. This can be achieved by replacing average time variant signal with average DC and small signal component. This step is vital before engaging with step

4, perturbations of the operating point are introduced and then expressed in the converters steady state equations.

IV. **Step 4** – Linearization simplifies complex differential equations into linear equations to simplify the process of deriving analytic solutions or to apply control techniques. To achieve step 4, the equation obtained after step 3 is analyzed, the steady state DC component variables that are highlighted in green, and the nonlinear variables highlighted in red are removed. Eqs. (4.42), (4.44), (4.48) and (4.50) are linearized equations which enables the designer to analyze the system's response to perturbation which is very helpful in control systems design and it also enables the use of linear stability analysis techniques to assess the stability of the system.

4.3.1 Buck Converter

ON – Time steady state

$$\begin{aligned} V_L &= V_{in} - V_{out} \\ i_c &= i_L - i_{out} \\ &= i_L - \frac{V_{out}}{R_L} \end{aligned} \quad \textbf{(4.39)}$$

i_{out} – Output current
R_L – Load resistor

OFF – Time steady state

$$\begin{aligned} V_L &= -V_{out} \\ i_c &= i_L - i_{out} \\ &= i_L - \frac{V_{out}}{R_L} \end{aligned} \quad \textbf{(4.40)}$$

Inductor Voltage.Sec balance

$$L\frac{dI_L}{dt} = D(t)(V_{in}(t) - V_{out}(t)) + (1-D)(t)(-V_{out}(t)) \quad \textbf{(4.41)}$$

Perturbation V(t) = V + v.

$$L\frac{d(I_L + \tilde{\imath}_L)}{dt} = \left(D + \tilde{\mathrm{d}}\right)((V_{in} + \tilde{v}_{in}) - (V_{out} + \tilde{v}_{out})) + \left(1 - \left(D + \tilde{d}\right)\right)(-(V_{out} - \tilde{v}_{out}))$$

Linearization

$$= DV_{in} + D\tilde{v}_{\text{in}} + \tilde{d}V_{in} + \tilde{d}\tilde{v}_{\text{in}} - DV_{out} - D\tilde{v}_{out} - \tilde{d}V_{out}$$

$$- \tilde{d}\tilde{v}_{out} - V_{out} - \tilde{v}_{out} + \mathrm{D}V_{out} + \mathrm{D}\tilde{v}_{out} + \tilde{d}V_{out} + \tilde{d}\tilde{v}_{out}$$

$$= DV_{in} - V_{out} + D\tilde{v}_{\text{in}} + \tilde{d}V_{in} - \tilde{v}_{out} + \tilde{d}\tilde{v}_{\text{in}}$$

$$= D\tilde{v}_{\text{in}} + \tilde{d}V_{in} - \tilde{v}_{out}$$

$$L\frac{d\tilde{\imath}_{\mathrm{L}}}{d_t} = D\tilde{v}_{\text{in}} + \tilde{d}V_{in} - \tilde{v}_{out} \qquad \textbf{(4.42)}$$

$\tilde{v}_{\text{in}}$ – Input voltage perturbation
$\tilde{v}_{out}$ – Output voltage perturbation
$\tilde{d}$ – Duty cycle perturbation
$\tilde{\imath}_{\mathrm{L}}$ – Inductor current perturbation

Capacitor Charge Balance

$$C\frac{dV_C}{dt} = D(t)\left(I_L(t) - \frac{V_{out}(t)}{R_L(t)}\right) + (I_L(t) - \frac{V_{out}(t)}{R_L(t)})(1-D)(t) \qquad \textbf{(4.43)}$$

Perturbation V(t) = V + v

$$C\frac{d(V_{out} + \tilde{v}_{out})}{dt} = \left(D + \tilde{\mathrm{d}}\right)(I_L + \tilde{\imath}_{\mathrm{L}} - \frac{V_{out}}{R_L} - \frac{\tilde{v}_{out}}{R_L}) + \left(1 - \left(D + \tilde{d}\right)\right)(I_L + \tilde{\imath}_{\mathrm{L}} - \frac{V_{out}}{R_L} - \frac{\tilde{v}_{out}}{R_L})$$

Linearization

$$= DI_L + D\tilde{\imath}_{\mathrm{L}} + \tilde{d}I_L + \tilde{d}\tilde{\imath}_{\mathrm{L}} - \tilde{d}\frac{V_{out}}{R_L} - \tilde{d}\frac{\tilde{v}_{out}}{R_L} - D\frac{V_{out}}{R_L} - D\frac{\tilde{v}_{out}}{R_L} + I_L + \tilde{\imath}_{\mathrm{L}} - \frac{V_{out}}{R_L} -$$

$$\frac{\tilde{v}_{out}}{R_L} - DI_L - Di_L - dI_L - di_L + D\frac{V_{out}}{R_L} + D\frac{\tilde{v}_{out}}{R_L} + d\frac{V_{out}}{R_L} + d\frac{\tilde{v}_{out}}{R_L}$$

$$= I_L - \frac{V_{out}}{R_L} + \tilde{\imath}_{\mathrm{L}} - \frac{\tilde{v}_{out}}{R_L}$$

$$= \tilde{\imath}_{\mathrm{L}} - \frac{\tilde{v}_{out}}{R_L}$$

$$C\frac{d\tilde{v}_{out}}{dt} = \tilde{\imath}_{\mathrm{L}} - \frac{\tilde{v}_{out}}{R_L} \qquad \textbf{(4.44)}$$

4.3.2 Boost Converter

ON – Time steady state

$$V_L = V_{in}$$

$$I_c = -I_{out}$$

$$= -\frac{V_{out}}{R_L} \quad \textbf{(4.45)}$$

OFF – Time steady state

$$V_L = V_{in} - V_{out}$$

$$I_c = I_L - I_{out}$$

$$= I_L - \frac{V_{out}}{R_L} \quad \textbf{(4.46)}$$

Inductor Voltage.sec balance

$$L\frac{dI_L}{dt} = D(V_{in}) + (1-D)(V_{in} - V_{out}) \quad \textbf{(4.47)}$$

Perturbation V(t) = V + v.

$$L\frac{d(I_L + \tilde{\imath}_L)}{dt} = (D + \tilde{d})(V_{in} + \tilde{v}_{in}) + \left(1 - \left(D + \tilde{d}\right)\right)((V_{in} + \tilde{v}_{in}) - (V_{out} + \tilde{v}_{out}))$$

Linearization

$$= \left(D + \tilde{d}\right)(V_{in} + \tilde{v}_{in}) + \left(1 - \left(D + \tilde{d}\right)\right)(V_{in} + \tilde{v}_{in} - (V_{out} + \tilde{v}_{out})$$

$$= DV_{in} + D\tilde{v}_{in} + \tilde{d}V_{in} + \tilde{d}\tilde{v}_{in} + V_{in} + \tilde{v}_{in} - V_{out} - \tilde{v}_{out} - DV_{in}$$
$$- D\tilde{v}_{in} + DV_{out} + D\tilde{v}_{out} - \tilde{d}V_{in} - \tilde{d}\tilde{v}_{in} + \tilde{d}V_{out} + \tilde{d}\tilde{v}_{out}$$

$$= DV_{in} - DV_{in} + DV_{out} + V_{in} - V_{out} + D\tilde{v}_{in} - D\tilde{v}_{in} + \tilde{d}V_{in} + \tilde{v}_{in}$$

$$-\tilde{v}_{out} + D\tilde{v}_{out} - \tilde{d}V_{in} + \tilde{d}V_{out} + \tilde{d}\tilde{v}_{in} - \tilde{d}\tilde{v}_{in} + \tilde{d}\tilde{v}_{out}$$

$$= \tilde{v}_{in} - \tilde{v}_{out} + D\tilde{v}_{out} + \tilde{d}V_{out}$$

$$L\frac{d\tilde{\imath}_L}{dt} = \tilde{v}_{in} + \tilde{d}V_{out} - \tilde{v}_{out}(1-D) \quad \textbf{(4.48)}$$

Capacitor Charge Balance

$$C\frac{dV_{out}}{d_t} = D\left(-\frac{V_{out}}{R_L}\right) + (I_L - \frac{V_{out}}{R_L})(1-D) \tag{4.49}$$

Perturbation V(t) = V + v.

$$C\frac{d(V_{out}+\tilde{v}_{out})}{d_t} = (D+\tilde{d})(-\left(\frac{V_{out}}{R_L}+\frac{\tilde{v}_{out}}{R_L}\right)) + \left(1-(D+\tilde{d})\right)(I_L+\tilde{\imath_L}-\left(\frac{V_{out}}{R_L}+\frac{\tilde{v}_{out}}{R_L}\right))$$

Linearization

$$= -d\frac{V_{out}}{R_L} - d\frac{\tilde{v}_{out}}{R_L} - D\frac{V_{out}}{R_L} - D\frac{\tilde{v}_{out}}{R_L} + I_L + \tilde{\imath}_L - \frac{V_{out}}{R_L} - \frac{\tilde{v}_{out}}{R_L} - DI_L$$

$$- D\tilde{\imath}_L - \tilde{d}I_L - \tilde{d}\tilde{\imath}_L + D\frac{V_{out}}{R_L} + D\frac{\tilde{v}_{out}}{R_L} + \tilde{d}\frac{V_{out}}{R_L} + \tilde{d}\frac{\tilde{v}_{out}}{R_L}$$

$$= I_L - DI_L - \frac{V_{out}}{R_L} + \tilde{\imath}_L - D\tilde{\imath}_L - \tilde{d}I_L - \frac{\tilde{v}_{out}}{R_L} - \tilde{d}\tilde{\imath_L}$$

$$=\tilde{\imath}_L(1-D) - \tilde{d}I_L - \frac{\tilde{v}_{out}}{R_L}$$

$$C\frac{d\tilde{v}_{out}}{d_t} = \tilde{\imath}_L(1-D) - \tilde{d}I_L - \frac{\tilde{v}_{out}}{R_L} \tag{4.50}$$

4.4 Frequency Domain DC-DC Converter Modeling

Laplace transforms are utilized to translate the time domain equations to frequency domain equations. The translated equations are then utilized to derive the transfer functions for the system. The transfer function describes a correlation between the input and the output of the system. Moreover, transfer functions play a vital role in designing a feedback controller for the DC-DC converter. In Section 4.3 small signal model equations for both buck and boost operations of the converter are derived, these equations are in the time domain.

The Laplace transform will be utilized to translate the equations to the frequency domain. Furthermore, the frequency domain equations will be utilized to derive the transfer functions of the converter for the buck and boost operations. The transfer functions derived will provide a

platform to design a feedback controller for the converter utilizing frequency response techniques based on a small signal model.

4.4.1 Buck Converter Transfer Function

The time domain Eqs. (4.42) and (4.44) are translated to frequency domain Eqs. (4.51) and (4.52) to obtain a transfer function for the buck converter [90, 91]. The simultaneous method is utilized in the process of deriving the transfer functions in Eq. (4.56 – 4.58).

Laplace Transform

$$sL\tilde{\imath}_{\mathrm{L}} = D\tilde{v}_{\mathrm{in}} + \tilde{d}V_{in} - \tilde{v}_{out} \tag{4.51}$$

$$sC\tilde{v}_{out} = \tilde{\imath}_{\mathrm{L}} - \frac{\tilde{v}_{out}}{R_L} \tag{4.52}$$

$$\tilde{\imath}_{\mathrm{L}} = \tilde{v}_{out}(sC + \tfrac{1}{R_L}) \tag{4.53}$$

Substitute 4.53 to 4.51

$$sL\tilde{v}_{out}\,(sC + \frac{1}{R_L}) = D\tilde{v}_{\mathrm{in}} + \tilde{d}V_{in} - \tilde{v}_{out}$$

$$\tilde{v}_{out}\left(s^2LC + \frac{sL}{R_L} + 1\right) = D\tilde{v}_{\mathrm{in}} + \tilde{d}V_{in} \tag{4.54}$$

$$\tilde{v}_{out} = \tilde{v}_{\mathrm{in}}\frac{D}{s^2LC + \frac{sL}{R_L} + 1} + \tilde{d}\frac{V_{in}}{s^2LC + \frac{sL}{R_L} + 1}$$

$$\tilde{v}_{out} = \frac{\tilde{\imath}_{\mathrm{L}}}{sC + \frac{1}{R_L}} \tag{4.55}$$

Substitute 4.55 to 4.51

$$sL\tilde{\imath}_{\mathrm{L}} = D\tilde{v}_{\mathrm{in}} + \tilde{d}V_{in} - \frac{\tilde{\imath}_{\mathrm{L}}}{sC + \frac{1}{R_L}}$$

$$\tilde{\imath}_{\mathrm{L}}\left(\frac{s^2LC + \frac{sL}{R_L} + 1}{sC + \frac{1}{R_L}}\right) = D\tilde{v}_{\mathrm{in}} + \tilde{d}V_{in}$$

$$\tilde{\imath}_{\mathrm{L}} = \tilde{v}_{\mathrm{in}}\frac{D(sC + \frac{1}{R_L})}{s^2LC + s\frac{L}{R_L} + 1} + \tilde{d}\frac{V_{in}(sC + \frac{1}{R_L})}{s^2LC + s\frac{L}{R_L} + 1}$$

Transfer Functions Eqs.

Controlled output

$$\mathrm{G_{vd}}(s) = \frac{\tilde{v}_{out}}{\tilde{d}}|_{\tilde{v}_{\mathrm{in}}=0} = \frac{\mathrm{V_{in}}}{s^2LC + s\frac{L}{R_L} + 1} \quad \textbf{(4.56)}$$

lined to output

$$\mathrm{G_{vg}}(s) = \frac{\tilde{v}_{out}}{\tilde{v}_{\mathrm{in}}}|_{\tilde{d}=0} = \frac{D}{s^2LC + s\frac{L}{R_L} + 1} \quad \textbf{(4.57)}$$

Duty cycle to the inductor's current

$$\mathrm{G_{id}}(s) = \frac{\tilde{\imath}_{\mathrm{L}}}{\tilde{d}}|_{\tilde{v}_{\mathrm{in}}=0} = \frac{\mathrm{V_{in}}}{R_L} * \frac{sR_LC + 1}{s^2LC + s\frac{L}{R_L} + 1} \quad \textbf{(4.58)}$$

4.4.2 Boost Converter Transfer Function

The small signal modeled time domain boost operation Eqs. (4.48) and (4.50) are translated to frequency domain Eqs. (4.59) and (4.60) to obtain a transfer function for the boost converter [90, 91]. The simultaneous method is utilized in the process of deriving the transfer functions expression for boost operation.

Laplace Transform

$$sL\tilde{\imath}_{\mathrm{L}} = \tilde{v}_{\mathrm{in}} + \tilde{d}V_{out} - \tilde{v}_{out}\acute{D} \tag{4.59}$$

$$sC\tilde{v}_{out} = \tilde{\imath}_{\mathrm{L}}\acute{D} - \tilde{d}I_L - \frac{\tilde{v}_{out}}{R_L} \tag{4.60}$$

$$\tilde{\imath}_{\mathrm{L}} = \frac{\tilde{v}_{\mathrm{in}} + \tilde{d}V_{out} - \tilde{v}_{out}\acute{D}}{sL} \tag{4.61}$$

Substitute 4.61 to 4.60

$$sC\tilde{v}_{out} = \left(\frac{\tilde{v}_{\mathrm{in}} + \tilde{d}V_{out} - \tilde{v}_{out}\acute{D}}{sL}\right)\acute{D} - \tilde{d}I_L - \frac{\tilde{v}_{out}}{R_L}$$

$$\tilde{v}_{out}\left(sC + \frac{\acute{D}^2}{sL} + \frac{1}{R}\right) = \frac{\acute{D}\tilde{v}_{\mathrm{in}}}{sL} + \frac{\tilde{d}V_{out}\acute{D} - sLI_L\tilde{d}}{sL}$$

$$\tilde{v}_{out} = \tilde{v}_{\mathrm{in}}\frac{\acute{D}}{s^2LC + s\frac{L}{R_L} + \acute{D}^2} + \tilde{d}\frac{\acute{D}V_{out} - sLI_L}{s^2LC + s\frac{L}{R_L} + \acute{D}^2}$$

Eq. (4.62) was derived from Eq. (4.60)

Substitute 4.62 to 4.59

$$\tilde{v}_{out} = \frac{R_L\tilde{\imath}_L\acute{D} - R_L\mathrm{dI_L}\acute{D}}{R_LsC + 1} \tag{4.62}$$

$$sL\tilde{\imath}_{\mathrm{L}} = \tilde{v}_{\mathrm{in}} + \tilde{d}V_{out} - \frac{R_L\tilde{\imath}_L\acute{D} - R_L\mathrm{dI_L}}{R_LsC + 1} * \acute{D}$$

$$\tilde{\imath}_{\mathrm{L}}\left(\frac{s^2R_LLC + sL + R_L\acute{D}^2}{R_LsC + 1}\right) = \tilde{\mathrm{v}}_{\mathrm{in}} + \tilde{d}V_{out} + \frac{R_L\mathrm{dI_L}\acute{D}}{R_LsC + 1}$$

$$\tilde{\imath}_{\mathrm{L}} = \tilde{v}_{\mathrm{in}}\frac{1}{R_L} * \frac{R_LsC + 1}{s^2LC + s\frac{L}{R_L} + \acute{D}^2} + \tilde{d}\frac{V_{out}}{R_L} * \frac{R_LsC + 2}{s^2LC + s\frac{L}{R_L} + \acute{D}^2}$$

Transfer Functions

Controlled output

$$\mathrm{G_{vd}}(s) = \frac{\tilde{v}_{out}}{\tilde{d}}|_{\tilde{v}_{in}=0} = \frac{\acute{D}V_{out} - sLI_L}{s^2LC + s\frac{L}{R_L} + \acute{D}^2} = \frac{V_{out}}{\acute{D}^2} * \frac{\acute{D} - s\frac{LI_L}{V_{out}}}{s^2\frac{LC}{\acute{D}^2} + s\frac{L}{R_L\acute{D}^2} + 1} \quad \textbf{(4.63)}$$

lined to output.

$$\mathrm{G_{vg}}(s) = \frac{\tilde{v}_{out}}{\tilde{v}_{in}}|_{d=0} = \frac{\acute{D}}{s^2LC + s\frac{L}{R_L} + \acute{D}^2} = \frac{\acute{D}}{\acute{D}^2}\frac{1}{s^2\frac{LC}{\acute{D}^2} + s\frac{L}{R_L\acute{D}^2} + 1} \quad \textbf{(4.64)}$$

Duty cycle to Inductor current

$$\mathrm{G_{id}}(s) = \frac{\tilde{\imath}_{\mathrm{L}}}{\tilde{d}}|_{\tilde{v}_{in}=0} = \frac{V_{out}}{R_L} * \frac{R_LCs + 2}{s^2LC + s\frac{L}{R_L} + \acute{D}^2} = \frac{V_{out}}{R_L\acute{D}^2} * \frac{R_LCs + 2}{s^2\frac{LC}{\acute{D}^2} + s\frac{L}{\acute{D}^2R_L} + 1} \quad \textbf{(4.65)}$$

4.5 Converter Design

The PV array generated voltage, which is the input voltage to the buck-boost converter varies. This is due to the changes in irradiance and temperature. The converter linking the PV array and the DC bus will play a vital role in regulating the bus voltage to 48V DC. Parameters for the buck and boost operations design of the converter are calculated based on the assumption that the maximum and minimum input voltage is constant, the converter is operating in a steady state, continuous conduction mode, and no losses are accounted for.

Furthermore, the proposed system will use a 2-switch buck-boost non-inverting unidirectional DC-DC converter. The converter will be designed to operate with only two modes (buck or boost) [74-77, 79]. The mode of operation will be selected depending on the status of the bus voltage. If the bus voltage is $>$ 48 V DC buck operation will be selected, however, when the bus voltage is $<$ 48

V DC boost operation will be selected. Moreover, the duty cycle controls the 2 MOSFET switches to achieve the desired converter output voltage, and the duty cycle values for the buck and boost operations are calculated utilizing Eqs. (4.21) and (4.38).

The converter passive components values were calculated. The inductor equations for both buck and boost operations are derived from Eqs. (4.13) and (4.30), whereas the equations to calculate the capacitor value for both the buck and boost operations are derived from Eqs. (4.18) and (4.35). Moreover, the inductor ripple current is estimated to be 20% of the input current and the capacitor ripple voltage is estimated to be 1% of the output voltage. Table 4.1 illustrates important specifications that will aid the process of mathematically designing a converter.

Table 4.1 Subgrid A-D system specifications for DC-DC Buck-Boost converter design

System Specifications		
Microgrid subgrid	**A-C**	**D**
Daily Demand PV Array output power (w)	15300	16227
PV Array Maximum Peak output power (w)	3754.60	3982.10
PV Array Maximum Peak output current (A)	54.99	61.10
PV Array maximum output voltage (v)	70.4	70.4
PV Array minimum output voltage (v)	10	10
Converter Maximum output voltage (v)	48	48
Converter Maximum output current (A)	78	83
Converter Minimum output current (A)	5.6	5.3
Switching frequency (KHz)	25	25
Load Resistance (Ω)	0.62	0.58

Buck Duty Cycle

$$D = \frac{V_{out}}{V_{in}}$$

$$= \frac{48}{70.4}$$

$$= 0.68$$

Boost Duty Cycle

$$D = \frac{V_{out} - V_{in}}{V_{out}}$$

$$= \frac{48 - 10}{48}$$

$$= 0.79$$

Subgrids A-C

Buck Operation

$$L > \frac{V_{out}(V_{in} - V_{out})}{f_s V_{in} \Delta i_L}$$

$$> \frac{48(70.4 - 48)}{25x10^3 * 70.4 * 10.9}$$

$$> 56x10^{-6}$$

Boost Operation

$$L > \frac{V_{in}(V_{out} - V_{in})}{f V_{out} \Delta i_L}$$

$$> \frac{10(48 - 10)}{25x10^3 * 48 * 10.9}$$

$$> 29x10^{-6}$$

Chosen value

$$L = 60x10^{-6}$$

$$C > \frac{V_{out}(V_{in} - V_{out})}{8 * L * f_s^2 * \Delta v_c}$$

$$> \frac{1 - 0.68}{8 * 60x10^{-6}(25x10^3)^2 * 0.48/48}$$

$$> 7.5x10^{-3}$$

$$C > \frac{D * I_{out}}{f_s * \Delta v_c}$$

$$> \frac{0.79 * 78}{25x10^3 * 0.48}$$

$$> 5.1x10^{-3}$$

Chosen value

$$C = 10x10^{-3}$$

Subgrid D

Buck Operation

$$L > \frac{V_{out}(V_{in} - V_{out})}{f_s V_{in} \Delta i_L}$$

$$> \frac{48(70.4 - 48)}{25x10^3 * 70.4 * 12.2}$$

$$> 50x10^{-6}$$

Boost Operation

$$L > \frac{V_{in}(V_{out} - V_{in})}{f V_{out} \Delta i_L}$$

$$> \frac{10(48 - 10)}{25x10^3 * 70.4 * 12.2}$$

$$> 18x10^{-6}$$

Chosen value

$$L = 60x10^{-6}$$

$$C > \frac{V_{out}(V_{in} - V_{out})}{8 * L * f_s^2 * \Delta v_c} \qquad C > \frac{D * I_{out}}{f_s * \Delta v_c}$$

$$> \frac{1 - 0.68}{8 * 60x10^{-6}(25x10^3)^2 * 0.48/48} \qquad > \frac{0.79 * 83}{25x10^3 * 0.48}$$

$$> 7.5x10^{-3} \qquad > 5.4x10^{-3}$$

Chosen value

$$C = 10x10^{-3}$$

4.5.1 Mathematical Modeling of DC-DC Converters Using a Transfer Function.

Buck and boost operation transfer functions were utilized to model and analyze the buck-boost converter in the S-domain. These transfer functions were derived in sections 4.4 and 4.5, and in this section, they will be simulated in MATLAB and Simulink to analyze the response of the buck-boost converter. The step response plot was used in analyzing the response of the buck-boost. The step response aids the process of analyzing closed-loop system behavior when a unit step input is applied to the designed system. The characteristics of the step response that will be analyzed are the rise time, overshoot, settling time, and steady state error.

Furthermore, controllers will be designed for the closed-loop buck-boost converter to adhere to certain design requirements and to obtain the desired response. The compensator for each operation was designed utilizing the control systems design computer application in MATLAB. The computer application allows the designer to graphically design a compensator for the system by adding poles/zeros in a closed loop system Bode and/or root locus plots.

Moreover, a closed Loop Bode Editor graphical tuning method was utilized for the design of the compensators for the buck and boost operations. The preferable design requirements were that the closed loop system with compensator bode plots needs to have a gain margin of 2-10 dB and a phase margin of 30-60 degrees [92] for a robust system. The desired step response characteristics of the compensated buck-boost converter were, that it needs to achieve ≤0.005 seconds rise time, ≤0.2 seconds settling time, 0% overshoot, and a steady state error of 0.

4.5.1.1 Buck Operation

The buck operation controlled input transfer function after substituting the converter LCR values is illustrated by Eq. (4.66).

$$\mathrm{G_{vd}}(s) = \frac{\mathrm{V_{in}}}{s^2LC + s\frac{L}{R_L} + 1}$$

$$\mathrm{G_{vd}}(s) = 70.4 * \frac{1}{6x10^{-7}s^2 + 9.7x10^{-5}s + 1} \quad \textbf{(4.66)}$$

The uncompensated unity feedback buck operation transfer function was simulated, the results indicated good rise time and settling time as per design requirements. However, the step response plot had an overshot percentage greater than $> 0\%$, and a steady state error > 0. A compensator is required to reduce the overshot to 0% and the steady state error to 0. The compensator was designed utilizing the control system designer app on MATLAB by adding a real pole and real zero to the bode plot of the buck operation closed-loop transfer function to achieve the required response. Eq. (4.67) expresses the transfer function of the compensator designed on the control system designer app.

Furthermore, a closed-loop transfer function of the buck operation and the designed compensator were simulated in Simulink to further observe and confirm the results obtained from the control systems designer App. Fig. 4.5 illustrates the Simulink simulation,

$$\mathrm{C}(s) = \frac{0.065107(s + 983)}{s + 0.8} \quad \textbf{(4.67)}$$

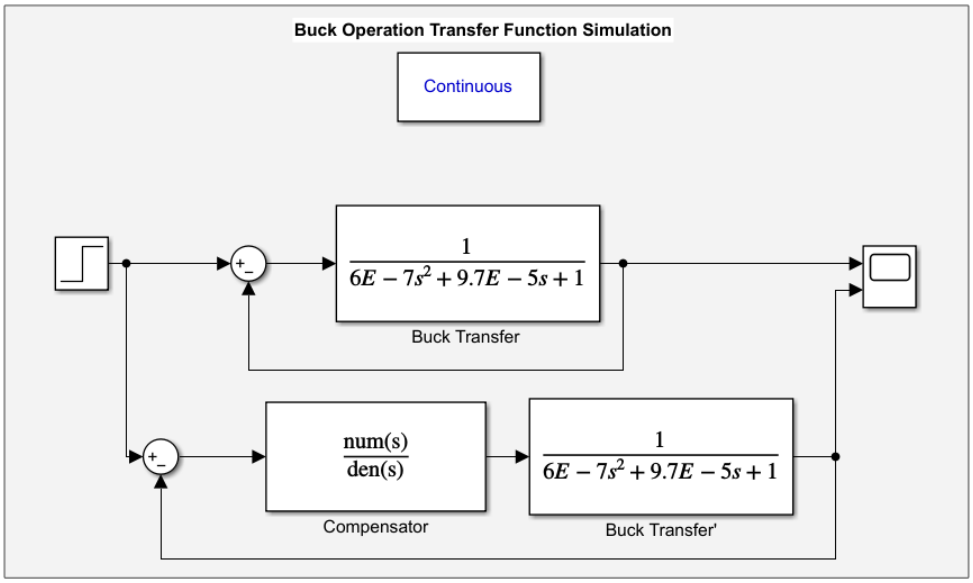

Figure 4.5 Buck Operation Transfer Function and Compensator Simulation on Simulink

4.5.1.2 Boost Operation

The boost controlled input transfer function is represented in Eq. (4.68) with substituted LCR values.

$$G_{vd}(s) = \frac{V_{in} - sLI_L}{s^2LC + s\frac{L}{R_L} + \acute{D}^2} = \frac{V_{out}}{\acute{D}^2} * \frac{\acute{D} - s\frac{LI_L}{V_{out}}}{s^2\frac{LC}{\acute{D}^2} + s\frac{L}{R_L\acute{D}^2} + 1}$$

$$G_{vd}(s) = \frac{48}{(1-0.79)^2} * \frac{(1-0.79) - 6.87x10^{-5}s}{1.4x10^{-5}s^2 + 2.19x10^{-3}s + 1} \quad \textbf{(4.68)}$$

The closed loop uncompensated controlled input transfer function with unit feedback for boost operation was simulated on MATLAB and Simulink, the results indicated an overshoot percentage greater than $> 0\%$ and a steady state error > 0. A compensator is required to reduce the overshot to 0% and reduce the steady state error to 0. The compensator was designed using the control system designer app on MATLAB by adding poles to the bode plot of the system to achieve the required response.

Furthermore, the transfer function for the designed compensator is expressed by Eq. (4.69). The closed-loop transfer function of the boost operation and a designed compensator were simulated in Simulink to further observe and confirm the results obtained from the control systems designer computer application. Fig. 4.6 illustrates the Simulink simulation.

$$C(s) = \frac{0.022727\ (s + 336.6)}{(s + 0.15)} \tag{4.69}$$

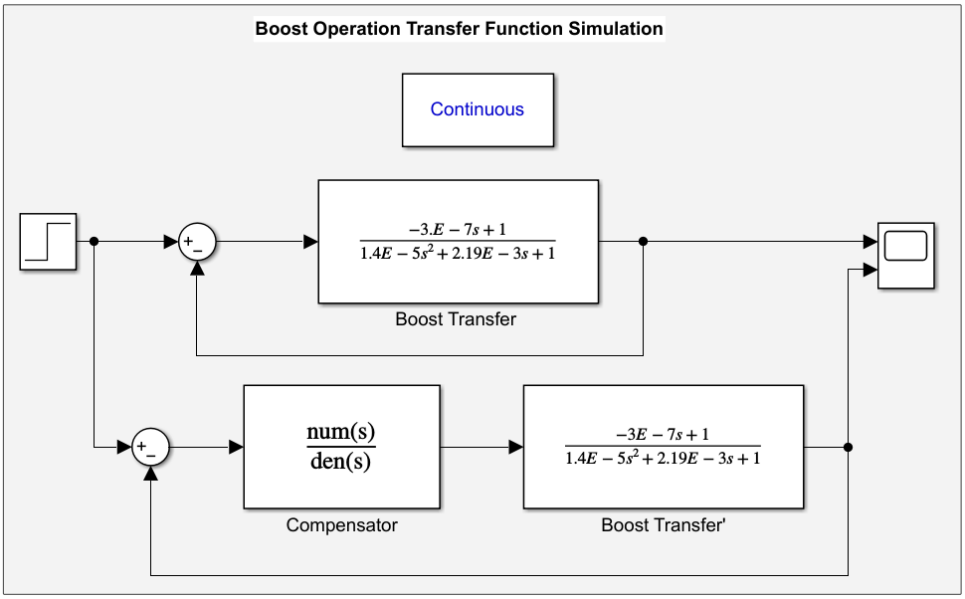

Figure 4.6 Boost Operation Transfer Function and Compensator Simulation on Simulink

4.5.2 Circuitry Modelling of the DC-DC Converter in Simulink

The circuitry model in Fig. 4.7 of the buck-boost converter was simulated on Simulink. The model was interfaced with the feedback controller as illustrated by Fig. 4.8 to regulate the output voltage to 48 DC [74-77, 79]. The feedback controller comprises of 3 parts:

I. Buck operation feedback control modeled with the compensator transfer function expressed by Eq. (4.67).
II. Boost operation feedback control modeled with the compensator transfer function expressed by Eq. (4.69).
III. Operation selector, the selector sends a feedback controller generated duty cycle to either the buck or boost switch depending on the ratio of 70.4 which is equal to the maximum

input voltage from the PV array and the bus voltage. If the ratio is ≥ 0.682 and < 1.45 the buck switch will operate with the feedback controller generated duty cycle and the boost switch will be switched OFF. If the ratio is < 0.682 the boost switch will operate with the feedback controller generated duty cycle and the buck switch will be switched ON.

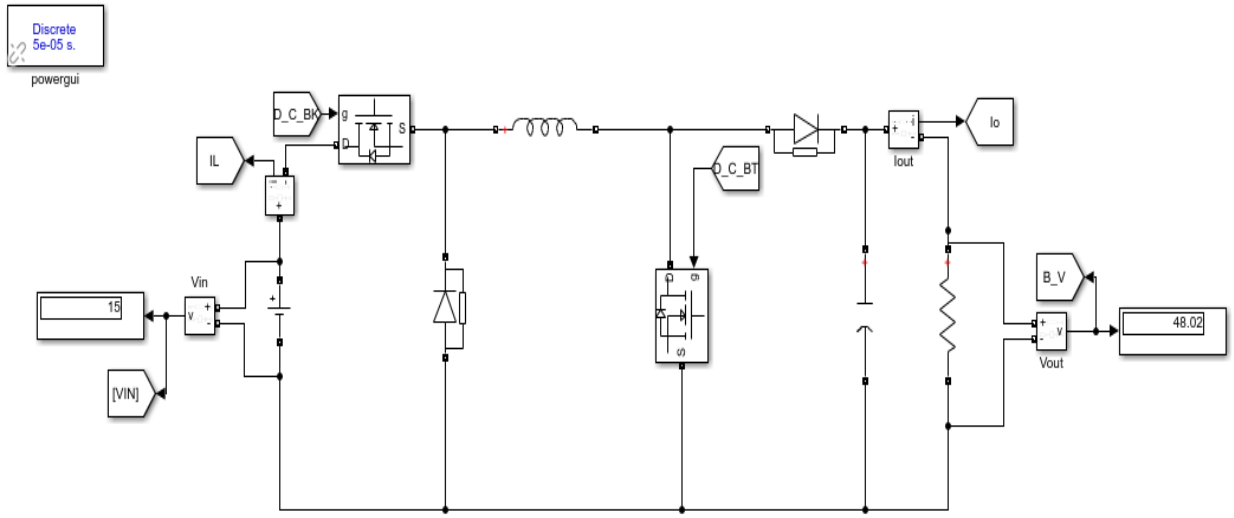

Figure 4.7 Buck-Boost converter Simulink circuitry model.

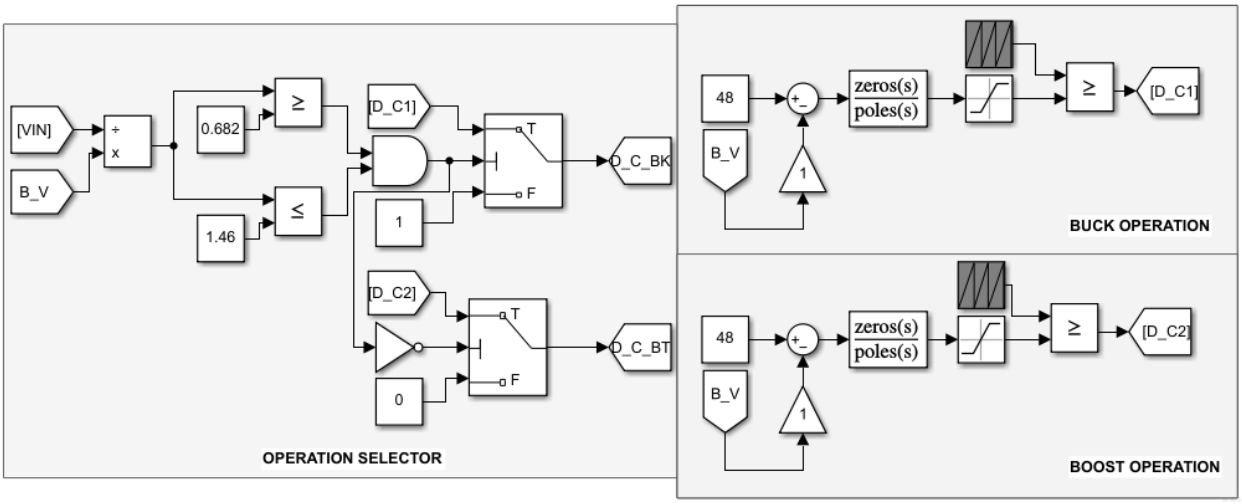

Figure 4.8 Feedback controller

4.6 MPPT Design

The perturb and observe MPPT algorithm will be utilized to harvest the maximum power from the PV panels. P&O MPPT optimizes PV array output power by continuously perturbing the operating voltage or current of the PV array and keeping track of the output power for each iteration [40, 43, 93-95]. If there is a difference between the current power and the previous power the duty cycle will perturbed up or down depending on the power difference. Fig. 4.9 illustrates the operation of the P&O MPPT algorithm. Fig. 4.10 illustrates the MPPT controller, the MPPT controller generates a duty cycle to control the buck-boost power switches making sure maximum power is harvested from the PV arrays.

The buck-boost controlled switches are controlled by the generated duty cycle one at a time as illustrated by Fig. 4.10. If the ratio between the Bus voltage and the PV array generated voltage is ≥ 0.682 and <1.45 the buck switch will operate with the MPPT controller generated duty cycle and the boost switch will be switched OFF, else the boost switch will operate with the MPPT controller generated duty cycle and the buck switch will be switched ON. The MPPT controller, PV array, and buck-boost converter were simulated in Simulink to observe and validate the operation of the MPPT controller illustrated in Fig. 4.10. Fig. 4.11 illustrates the MPPT controlled buck-boost converter. The results from the simulation are illustrated in Fig. 5.10 - 5.14 in Chapter 5.

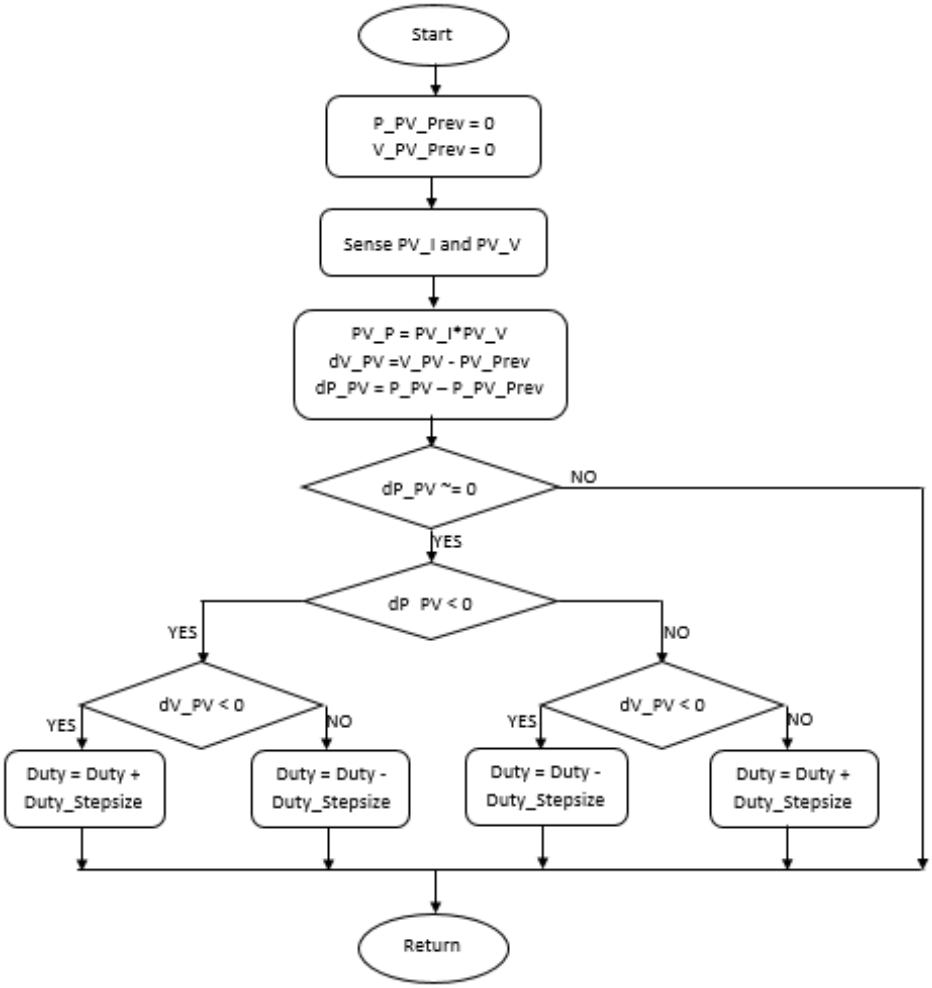

Figure 4.9 MPPT Flow Chart [40, 43, 93-95]

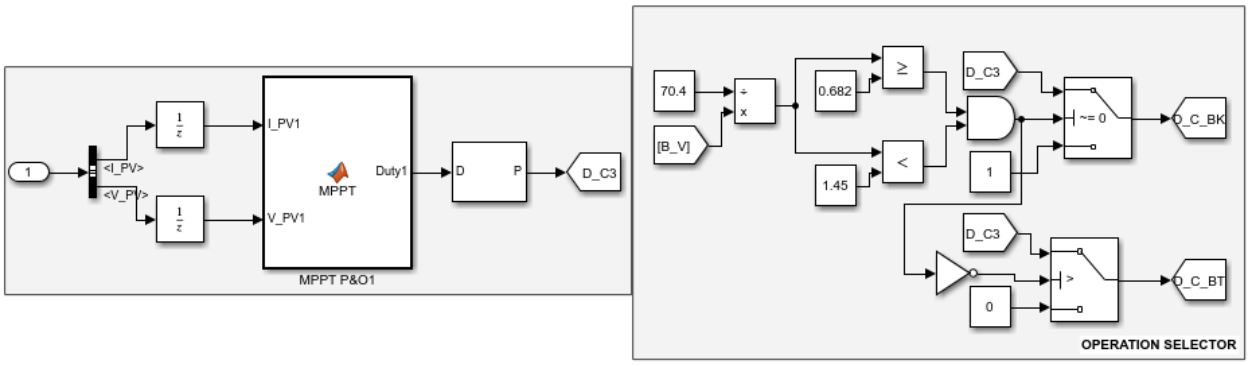

Figure 4.10 MPPT controller Simulink Model

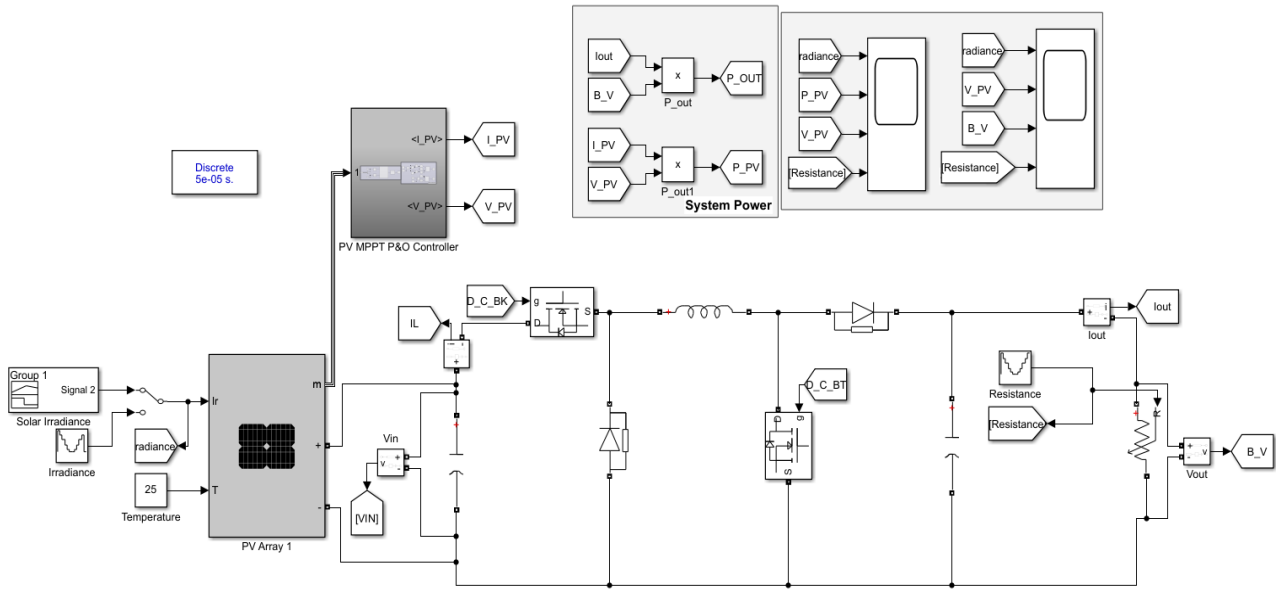

Figure 4.11 PV array with an MPPT controlled buck-boost converter.

4.7 MPPT-Feedback Controller

The MPPT controller and the Feedback controller are unified by the PI controller which generates an output that is utilized to generate the duty cycle to drive the buck-boost power switches [96]. Fig 4.12 illustrates the MPPT-Feedback controller Simulink model, which unifies the MPPT controller and the feedback controller. The MPPT-Feedback controller enables the PV system to harvest maximum power while regulating the Bus voltage to 48V DC. The designed MPPT-Feedback controller was simulated on Simulink and the results can be observed in Chapter 5, Fig. 5.13 and Fig. 5.14.

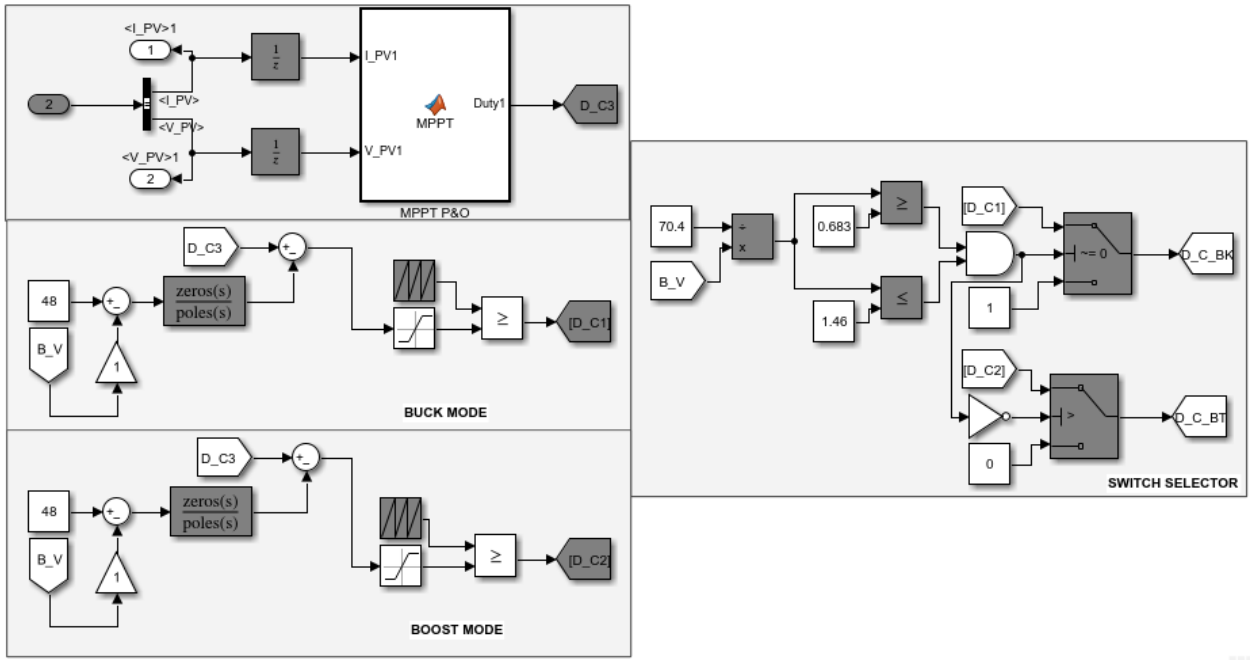

Figure 4.12 MPPT-Feedback Controller Simulink Model.

4.8 Battery Energy Storage System BMS SIMULINK Simulation

The BES system will supply the energy demand to the loads when there is no power harvested from the PV array. Battery protection during charging and discharge is vital to avoid battery damage. Fig. 4.13 illustrates the Battery Management system (BMS) based on a charge controller SIMULINK model, the model working in conjunction with Fig. 4.14 to control the charging and discharging of batteries utilizing the duty ratio generated by Fig. 4.14. The generated duty ratio controls the bi-directional DC-DC converter to either charge or discharge the batteries depending on the status of the battery and bus voltage.

Furthermore, Fig. 4.14 has four sections, the charging mode control, the discharging mode control, the mode selector, and the duty ratio generator. Charging is controlled by a PI controller which has an input error signal generated by subtracting the actual battery voltage reading from the fully charged battery voltage reference value. This PI controller generates a reference signal for the charging of batteries. Discharging is also controlled by a PI controller which has an input error

signal generated by subtracting the actual bus voltage from the bus reference voltage. The PI controller then generates a reference signal for discharging batteries.

Moreover, the mode selector sends the charge or discharge reference signal to the pulse generator. The reference signal is subtracted from the actual battery current to generate the input error signal for the PI controller which will generate a required duty cycle for the bi-directional DC-DC converter depending on the battery and load voltage. The generated duty cycle will control the bi-directional DC-DC converter two switches to either charge or discharge the batteries depending on the reference signal selected by the mode selector.

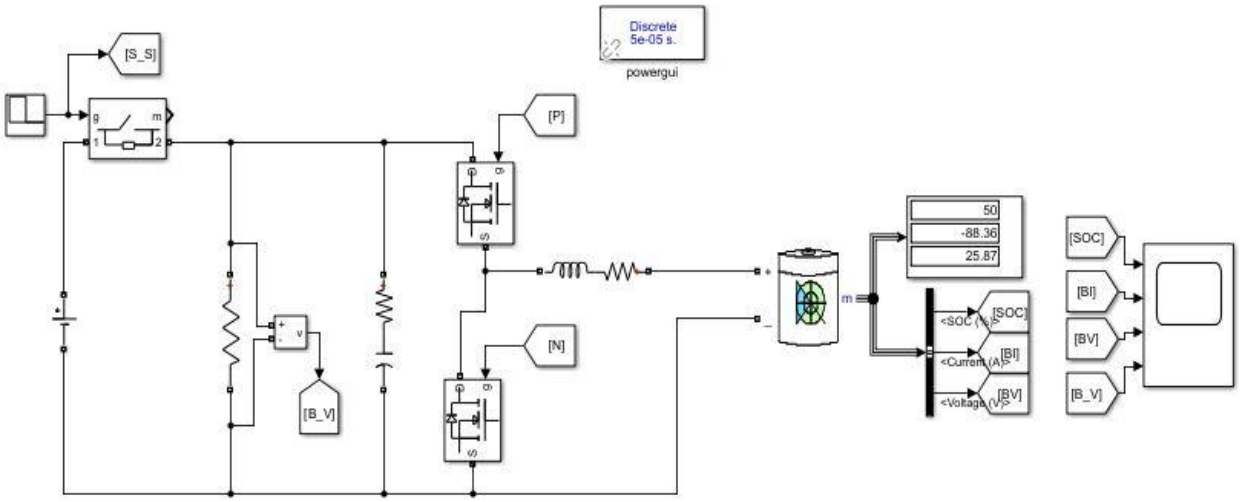

Figure 4.13 Battery charge controller

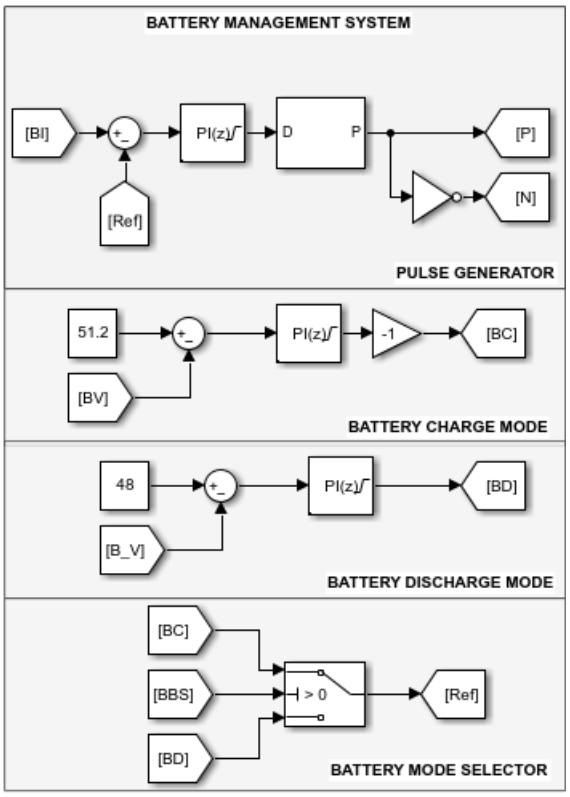

Figure 4.14 Battery Management System

4.9 DC Microgrid Control and Power Sharing

Implementation of the functional controller is crucial for the efficient operation and stability of the microgrid subgrids and a microgrid. The microgrid is operated in a hierarchical control strategy with two levels (Local and Global). The local control for each subgrid will regulate the local bus voltage utilizing local DERs, whereas the Global control will be responsible for power sharing among interconnected subgrids and regulate the local bus voltage for the subgrid in need.

Moreover, all four microgrid subgrids will be operated in four modes depending on the status of the DERs which include the PV array and the BES.

I. Mode 1: $P_{PV} > P_L \,\&\, SOC \geq 90\%$

This mode will be activated when power harvested from the primary source is greater than the power required by the demand and the SOC of the BES system is greater or equal to 90%. During this mode, the PV array will operate under MPPT-feedback control, and the BES system will be in idle mode to protect the batteries from overcharging.

II. Mode 2: $P_{PV} > P_L$ & $SOC < 90\%$

This mode will be activated when power harvested from the primary source (PV array) is greater than the power required by the demand and the SOC of the BES system is not fully charged. During this mode, the PV array operates under MPPT-feedback control to provide the load with power and charge BES.

III. Mode 3: $P_{PV} < P_L$ & $20\% < SOC < 90\%$

This mode will be activated when power harvested from the primary source is less than the power required by the demand and the BES system is charged. The PV array will operate under the MPPT-feedback control and together with the BES system will provide the load with power as long as the SOC $> 20\%$ or $P_{PV} < P_L$.

IV. Mode 4: $P_{PV} < P_L$ & $SOC < 20\%$

This mode will be activated when power harvested from the primary source is less than the power required by the demand and the BES system is not charged. The PV array will operate under the MPPT-feedback control together with the global bus if power is available, that will be the first alternative or the microgrid subgrid will have load shedding if there is no power being shared.

4.9.1 Microgrid subgrid Control

This section will discuss local control of the subgrid, which includes the control of a PV array and BES system during different modes of operation mentioned in Section 4.9. Moreover, a single microgrid subgrid illustrated in Fig. 4.15 will be simulated on Matlab/Simulink to observe the operation and response of the designed controllers to imposed changes.

4.9.1.1 Local Control

PV Array

Local control will be based on a decentralized control strategy. Each DER has a dedicated controller for the DC-DC converter that links it to the local DC bus. The DC-DC converter linking the PV array and DC bus will be controlled by the MPPT-feedback controller illustrated in Fig.4.12. If the subgrid is operating in mode I, the PV array DC-DC converter duty cycle will be generated by the MPPT-feedback controller since the power generated by the PV array is greater

than the demand, and the BES system will be fully charged. The MPPT-feedback controller will regulate the bus voltage.

Furthermore, if the subgrid is operating in mode II, the PV array DC-DC converter duty cycle will be generated by the MPPT-feedback controller. Power generated by the PV array is required for the load demand and BES system charging. During mode III and mode IV, the PV array DC-DC converter duty cycle will be generated by the MPPT-feedback controller, the power generated by the PV array is less than the power required by demand.

BES

BES system will idle during mode I, the BMS illustrated by Fig. 4.14 will make sure charging is halted to protect the batteries from overcharging. If the subgrid enters mode II, the bidirectional DC-DC converter linking the BES system to the DC bus will be controlled by the duty cycle generated by the BMS to enable charging of the BES, since the power generated by the PV array is enough to cater to the demand and BES system charging.

Moreover, during mode III the BMS will sense the DC bus voltage status to be less than 48V and generate the duty cycle to control the bidirectional DC-DC converter to enable BES system discharge to regulate the DC bus voltage since power generated by the PV array is not enough to meet the demand. During mode IV, the BES system will be disconnected since the $SOC < 20\%$ and the power generated by the PV array is not sufficient to meet the demand and charge the BES system.

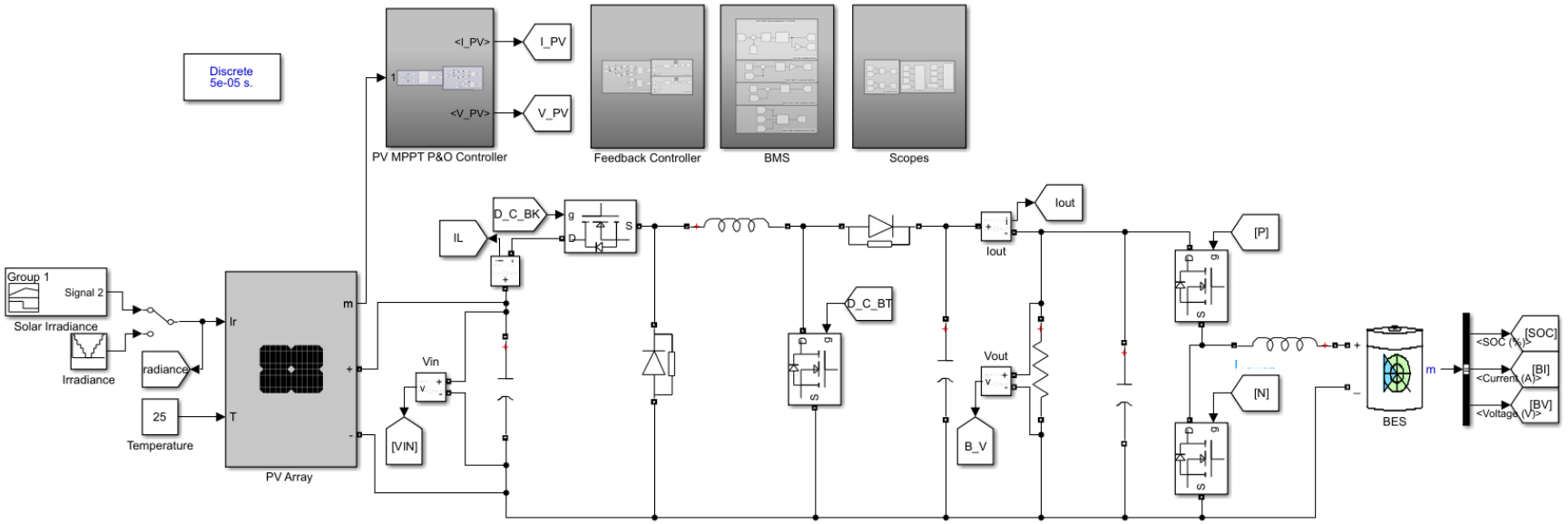

Figure 4.15 Microgrid Subgrid Simulink Simulation.

4.9.2 Microgrid Control

4.9.2.1 Global Control

Global control will oversee the power-sharing among the subgrids which is the critical aspect of the microgrid, and the process of power-sharing will be governed by the power-sharing management system (PSMS). The PSMS will be responsible for allowing the subgrid with excess power to share with a subgrid in need via a global DC bus that interconnects the subgrids through bidirectional DC-DC converters. Global control will employ a central control strategy based on DC Bus Signaling with the droop control method to achieve the goal of power sharing. The global controller continuously senses the local DC bus voltage and BES system SOC of each subgrid. Three conditions need to be met before the PSMS initiates sharing:

I. Initially, when there is a microgrid subgrid that is unable to meet the demand due to various technical or environmental reasons, an alert signal will be sent to the PSMS.
II. Then the PSMS will check if there is a microgrid subgrid with fully charged BES, and if there is,
III. It will proceed to do the third and final check on that microgrid subgrid if the power harvested from the primary source is greater than the demand.

If all three conditions are true, the PSMS will initiate power-sharing between the two microgrid subgrids, however, if one of the conditions is false the PSMS will not initiate power-sharing and the subgrid in need will enter load shedding.

4.9.2.2 Power Sharing Management System

The PSMS will be implemented on Matlab/Simulink utilizing the Matlab function for the control algorithm. The Matlab function will take as an input the state of each subgrid to keep track of the status of each subgrid. The PSMS is comprised of various parts which include the global control monitor (GCM), priority selector (PS), surplus subgrid monitor (SSM), the part that keeps track of the subgrid with surplus power illustrated by Fig. 4.17.

Moreover, the GCM continuously senses the DC bus voltage and the BES system SOC of the subgrids to keep track of the state of subgrid operation, the GCM is illustrated in Fig. 4.16. The GCM model is implemented on Simulink. The operation of the GCM is described below:

The GCM continuously senses the local bus voltage and SOC for each subgrid, depending on the outcome after checking specific actions will be implemented.

I. If local bus voltage is $\geq$ 48V & SOC $>$ 20%, no action will be taken as the subgrid is self-sustaining.
II. If local bus voltage is $\geq$ 48V & SOC $<$ 20%, no action will be taken as the subgrid is self-sustaining.
III. If a local bus voltage is $<$ 48V & SOC $<$ 20%, action will be taken as the subgrid is not self-sustaining.

Furthermore, a PS will be implemented to prioritize the sharing of power utilizing the first come, first served (FCFS) scheduling. The first alert is to be sent to the PS containing the subgrid ID which will alert the GC that the subgrid has transitioned to mode IV. This will be the first subgrid to receive power if it is available on the global DC bus, the global DC bus gets its power from one of the subgrids with surplus power.

Moreover, once the GC is alerted concerning a subgrid that is not self-sustaining, the GC will check if any of the subgrids have surplus power utilizing an SSM. The SSM illustrated in Fig. 4.17 will check the local DC bus voltage and SOC for each subgrid to identify the subgrid that can assist. If the SSM identifies that there is a subgrid that has surplus energy, an alert containing the subgrid ID will be sent to the GC to initiate power sharing between the subgrid noted by the GCM, PS, and the subgrid noted by the SSM. The sharing monitor is illustrated in Fig. 4.17.

The sharing subgrid will continue to share its power for as long as:

I. Surplus power is still available.
II. Subgrid accepting power still requires power.

The sharing subgrid will stop sharing its power when:

I. Its demand increases beyond the supply.
II. Subgrid accepting power becomes self-sustaining.

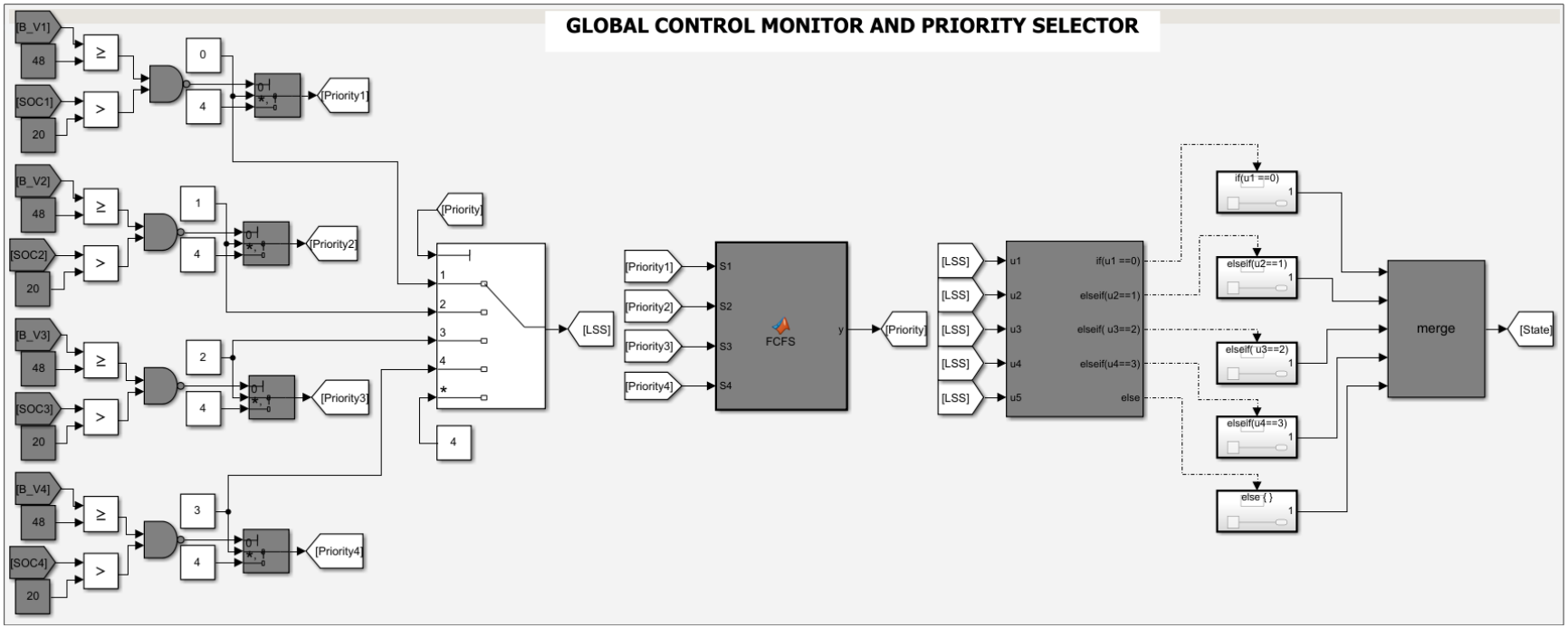

Figure 4.16 Global Control Monitor and Priority Selector.

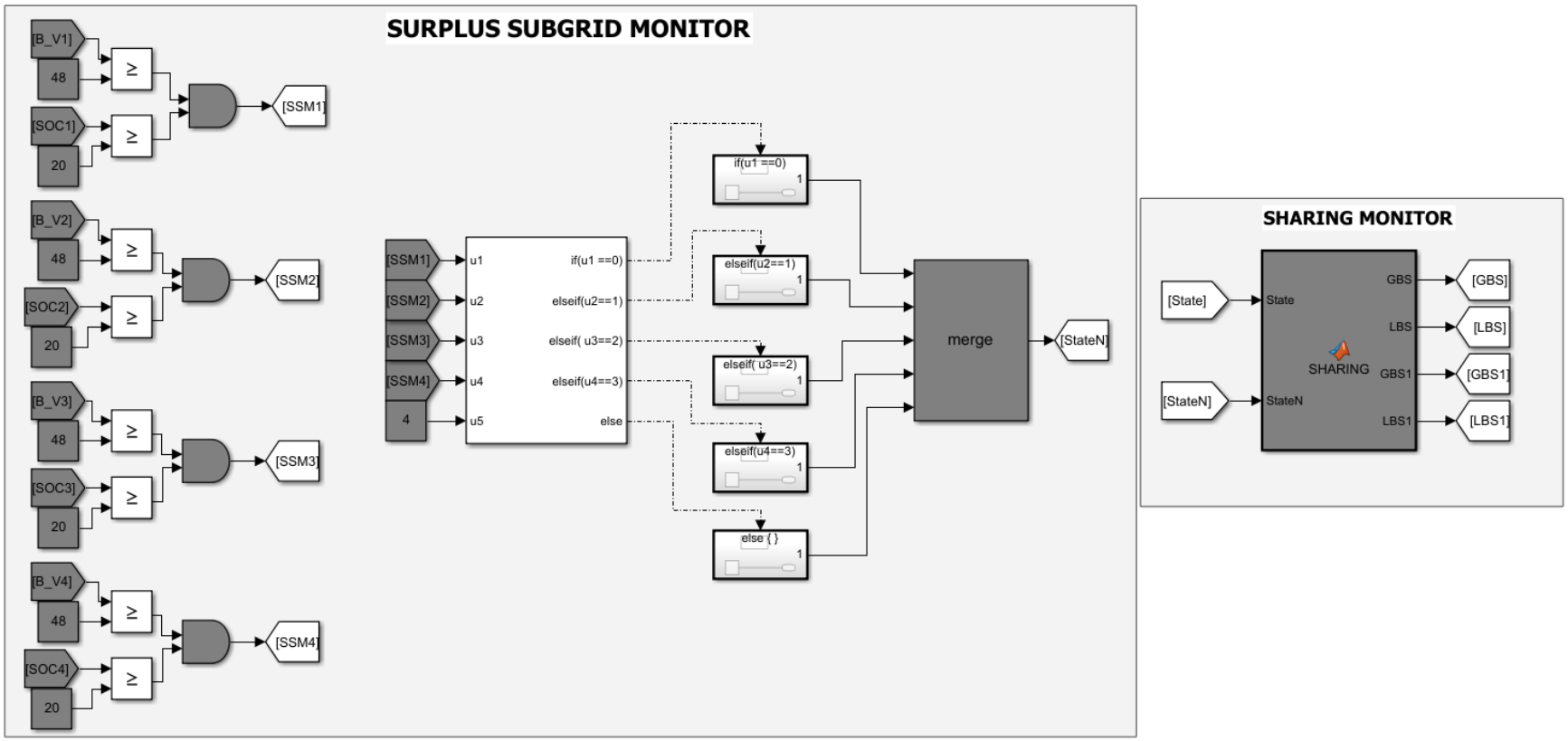

Figure 4.17 Surplus Subgrid Monitor and Sharing Monitor Simulink Model.

4.10 Microgrid Simulation

The research aims to implement a distributed 48V DC PV standalone microgrid which is optimum for its users. Fig. 4.18 illustrates the microgrid which is implemented from four interconnected microgrid subgrids, the interconnection allows power-sharing among the subgrids. The subgrids are implemented utilizing the components discussed in Chapters 3 and 4. The microgrid was simulated on MATLAB/Simulink based on different scenarios to observe the response of the implemented system.

Scenario 1

All 4 subgrids are self-sustaining.

Scenario 2

Observing what happens when 1 subgrid is not self-sustaining and none of the other subgrids have excess power to share. D has 20% SOC which is the shutdown SOC for the selected battery pack for all microgrid subgrids. Subgrids A, B, and C are fully occupied with their dedicated load demand and have no excess power to share. Moreover, a subgrid can only share power when power is harvested from the primary source (PV Array) and the BES system is fully charged.

Scenario 3

Faulty primary source, observing what happens when a primary source fault is imposed on subgrid D, in such a way that subgrid D is unable to harvest the power from the primary source and the BES system is disconnected due to low SOC.

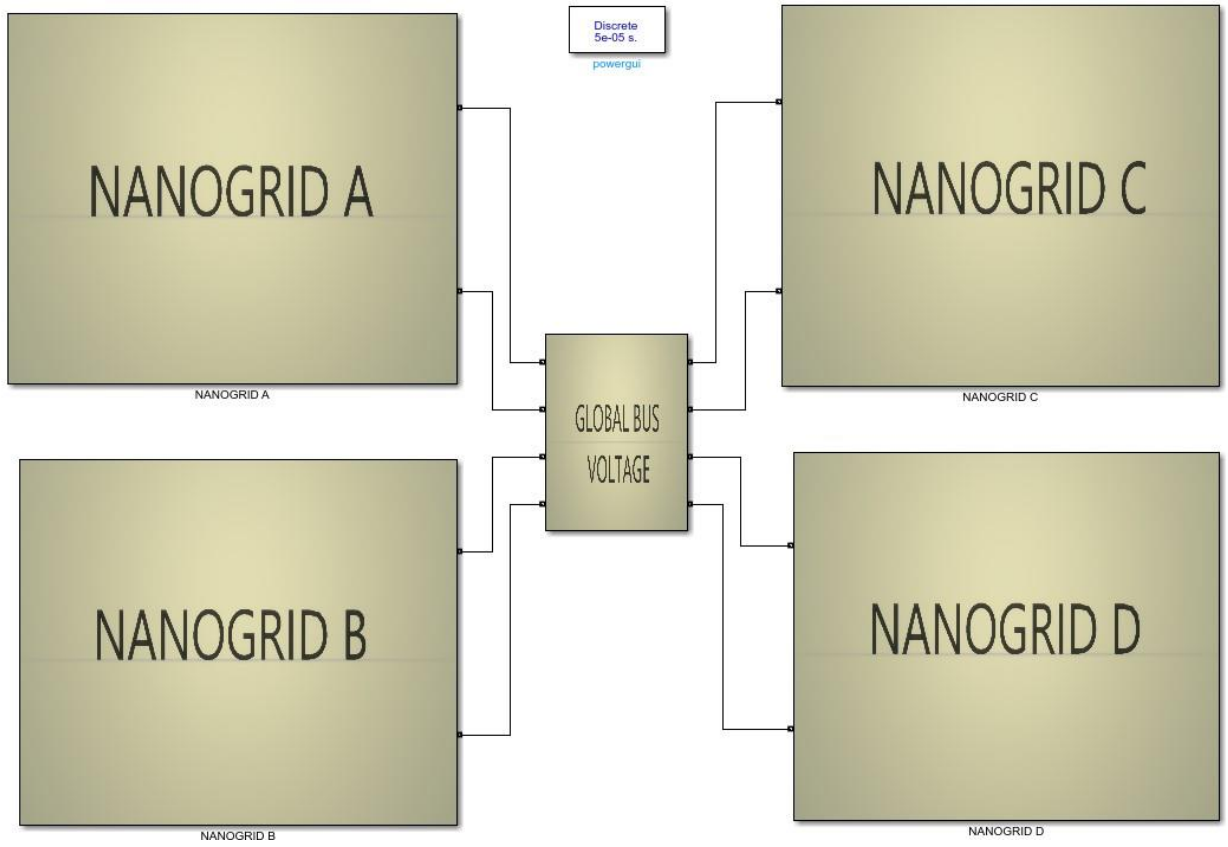

Figure 4.18 Microgrid Simulation on SIMULINK

4.11 Summary

In this Chapter, the proposed system based on the sizing requirements obtained in Chapter 3 was designed and simulated on MATLAB/SIMULINK. All the system components were simulated and the control technique algorithms were developed and simulated for both local power sharing control and global power sharing control. The results of the simulations will be presented and discussed in Chapter 5.

CHAPTER 5 RESULTS AND DISCUSSION

This chapter will present the results obtained from MATLAB and Simulink simulations. The simulations were done for individual components of the microgrid, and the results are illustrated and discussed in sections 5.1 – 5.3. Moreover, the microgrid including all the components was simulated and the results are illustrated and discussed in sections 5.4 – 5.5.

5.1 Buck Boost Converter

5.1.1 Buck Operation Transfer Function Results

Fig. 5.1 illustrates the buck operation closed-loop transfer function step response without the compensator acquired from MATLAB. The buck operation is stable as can be observed in Fig. 5.2 since the phase margin (PM) is positive, the gain margin (GM) is positive and the gain crossover frequency (ωgc) is less than the phase crossover frequency (ωpc). However, the PM and the GM values do not meet the design requirements. Moreover, the closed-loop step response rise time is 0.000538 seconds, the settling time is 0.0474 seconds, the plant has a good rise and settling time. However, the steady-state error is 0.5.

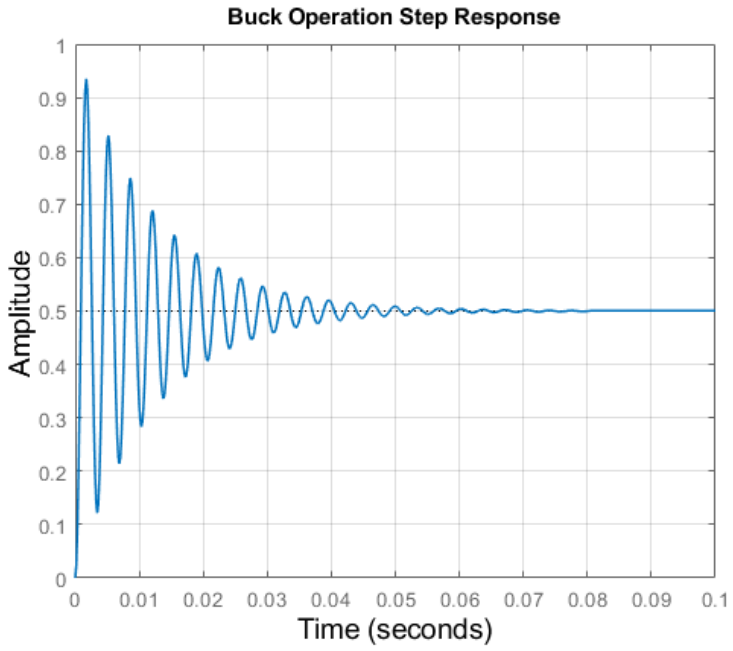

Figure 5.1 Buck Operation Transfer Function without Compensator Closed Loop Step Response Plot.

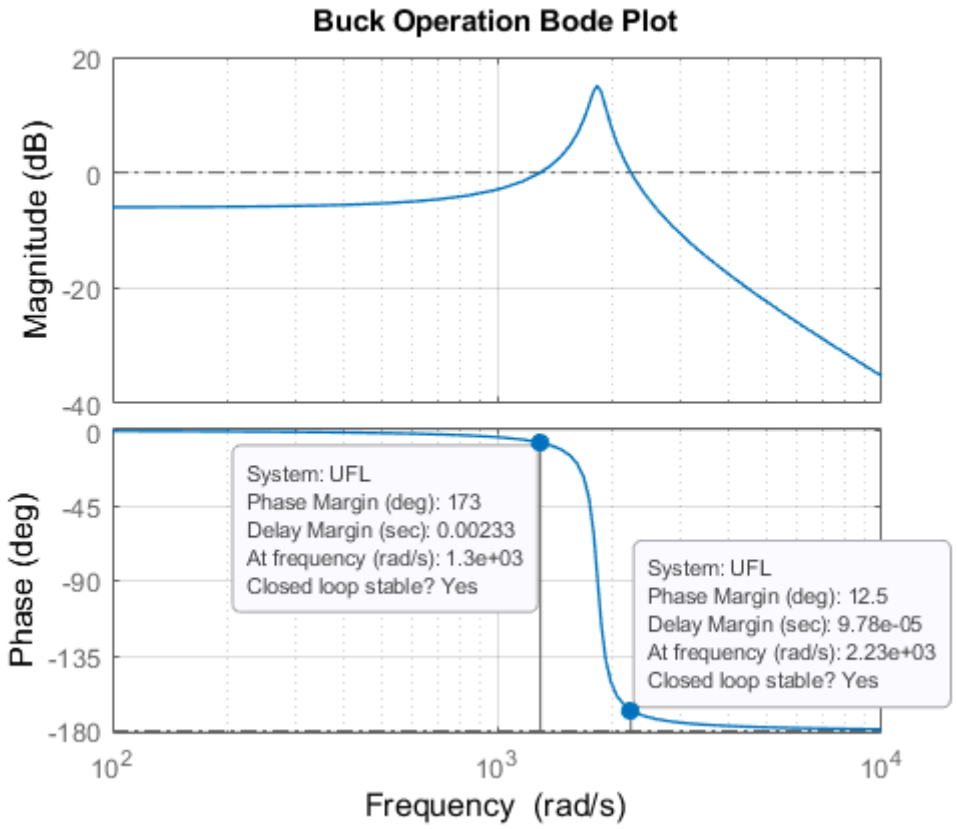

Figure 5.2 Buck Operation Transfer Function without Compensator Closed Loop Bode plot

Fig. 5.3 & 5.4 illustrate the step response and the bode plot for the buck operation closed-loop transfer function with a compensator. The compensator working in conjunction with the system transfer function was able to achieve the desired characteristics on the step response, the overshoot is 0%, the steady state error is 0, the rise time is 0.0496 seconds, with a settling time of 0.0899 seconds. The buck operation is stable as it can be observed from the Bode plot characteristics the $PM = 57.8^{o}$, $GM = 6.14\ dB$, and the $\omega pc > \omega gc$. Moreover, the design requirements for the closed-loop system were achieved.

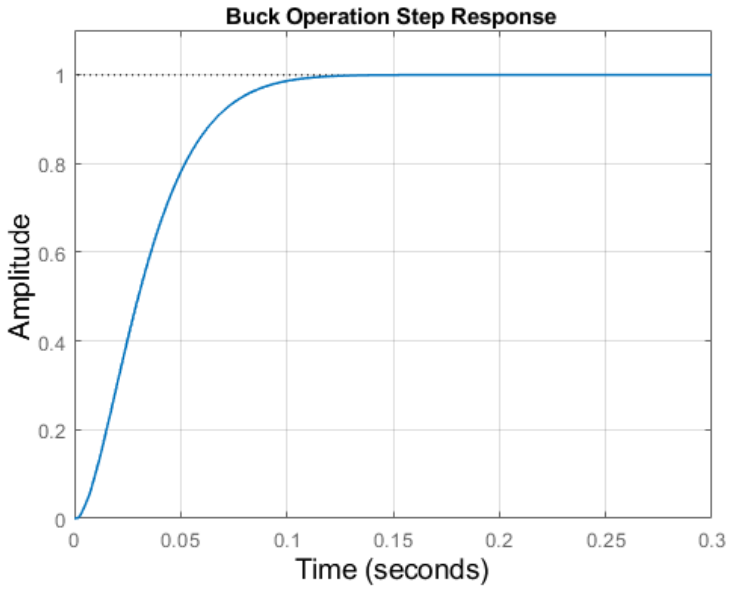

(a)

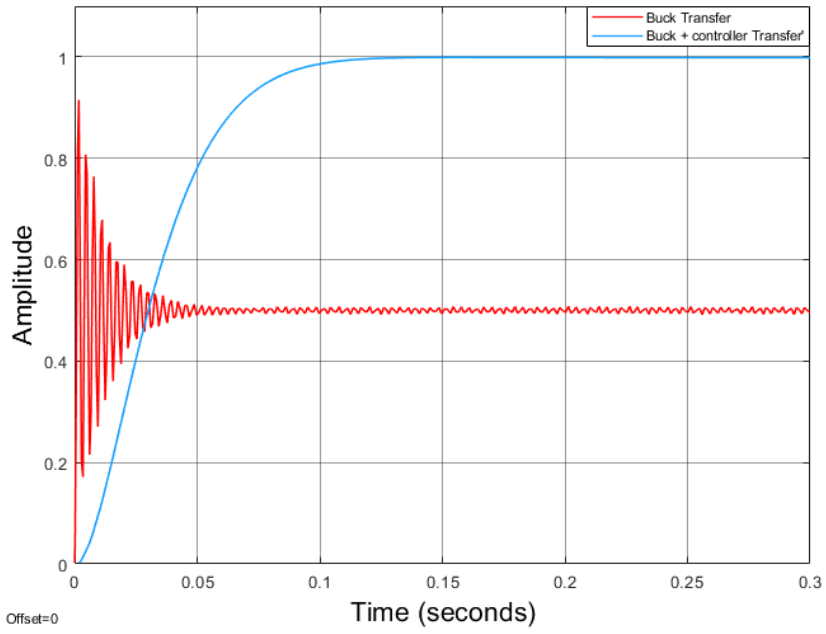

(b)

Figure 5.3 Buck Operation Step Response Transfer function with Controller/ Compensator. (a) Buck + Controller/ Compensator Transfer MATLAB Plot (b) Buck transfer and Buck + Controller/ Compensator Transfer Simulink Simulation Plot.

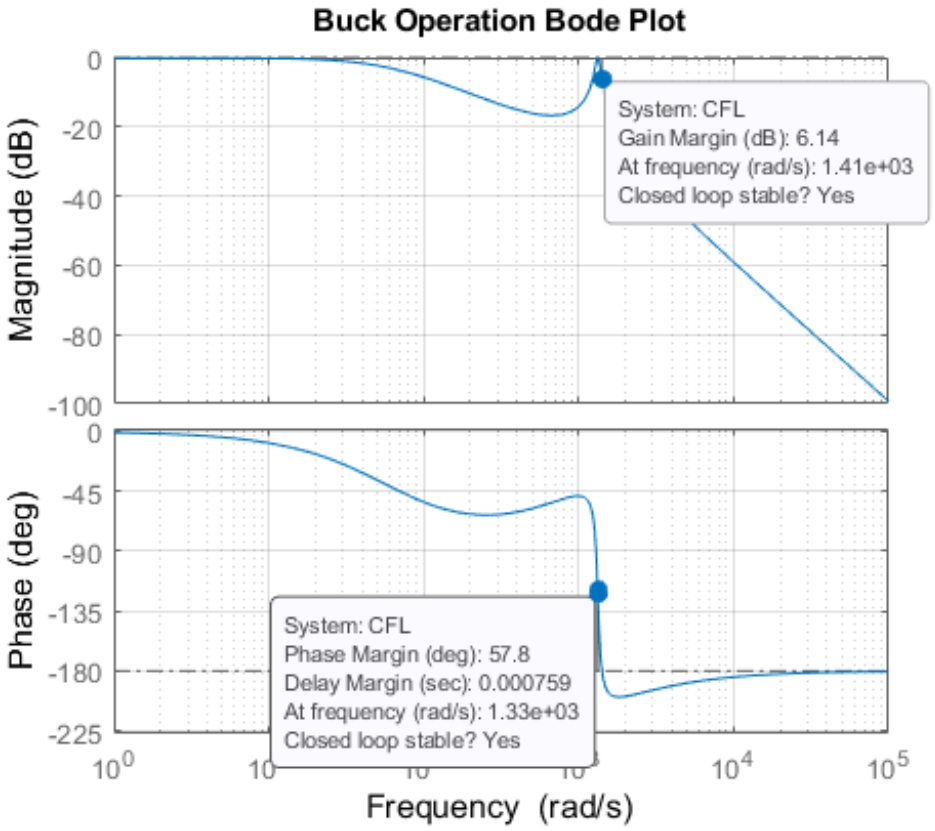

Figure 5.4 Buck Operation Transfer Function with Compensator Bode Plot.

5.1.2 Boost Operation Transfer Function Results

Fig. 5.5 illustrates the boost operation closed-loop transfer function step response without a compensator acquired from MATLAB. The boost operation is stable as can be observed in Fig. 5.6 since the phase margin (PM) is positive, the gain margin (GM) is positive, and the gain crossover frequency (ωgc) is less than the phase crossover frequency (ωpc). However, the PM and the GM values do not meet the design requirements. Moreover, the closed-loop step response rise time is 0.00251 seconds, the settling time is 0.568 seconds, the plant has a good rise. However, the steady-state error is, 0.5 and the rise is $>$ 0.2 seconds.

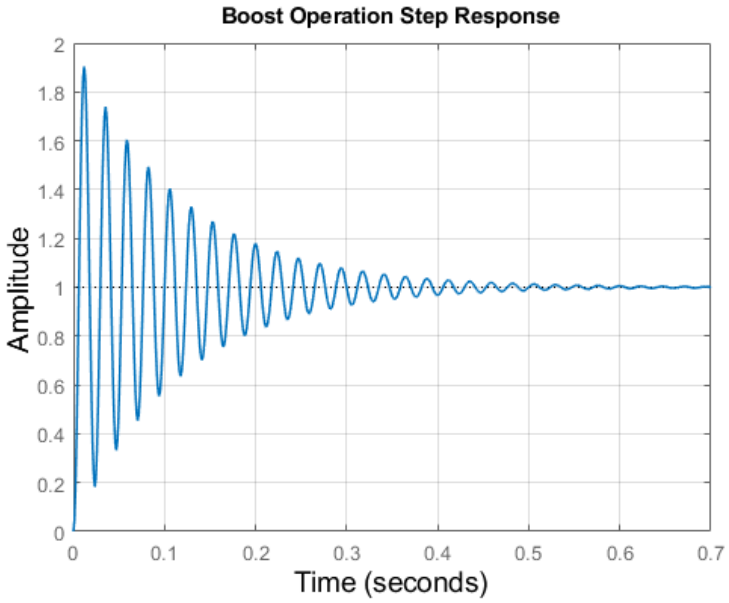

Figure 5.5 Boost Operation Closed-Loop Transfer Function without Compensator Step Response Plot

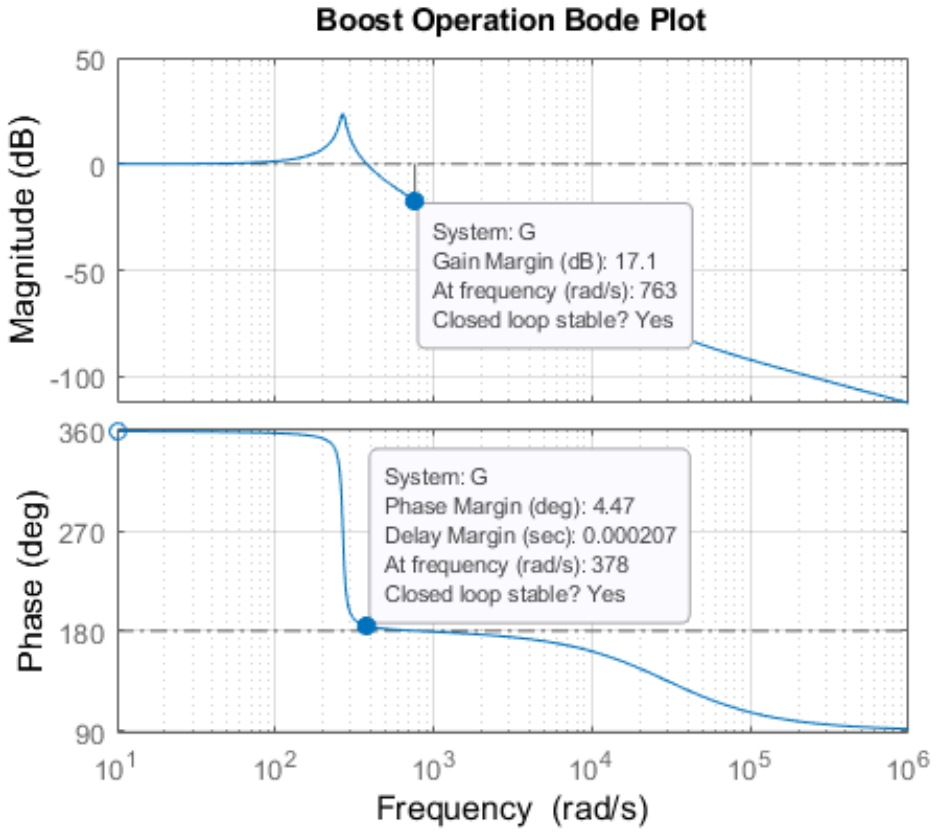

Figure 5.6 Boost Operation Closed-Loop Transfer Function without Compensator Bode Plot.

Fig. 5.7 & 5.8 illustrate the step response and the bode plot for the boost operation closed-loop transfer function with a compensator. The compensator working in conjunction with the transfer function was able to achieve the desired characteristics on the step response, the overshoot is 0%, the steady state error is 0, the rise time is 0.0747 seconds, with a settling time of 0.1084 seconds. The boost operation is stable as it can be observed from the Bode plot characteristics the $PM = 41.3^{o}$, $GM = 2.56\,dB$, and the $\omega pc > \omega gc$. Moreover, the design requirements for the closed loop boost operation were achieved.

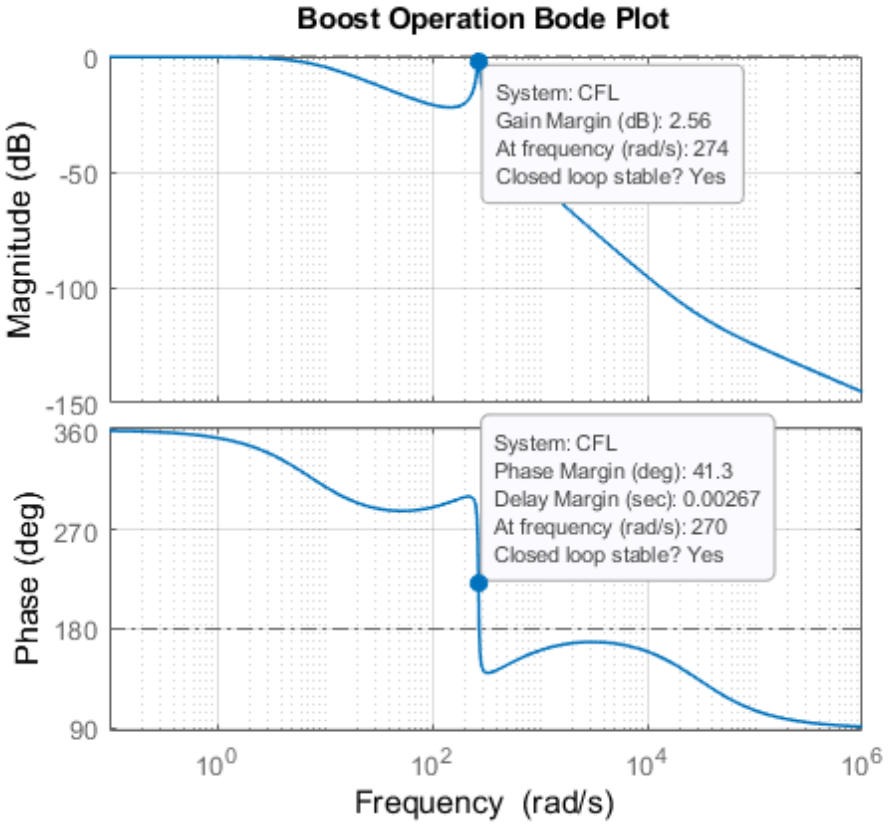

Figure 5.7 Boost Operation Closed-Loop Transfer Function with Compensator Bode Plot.

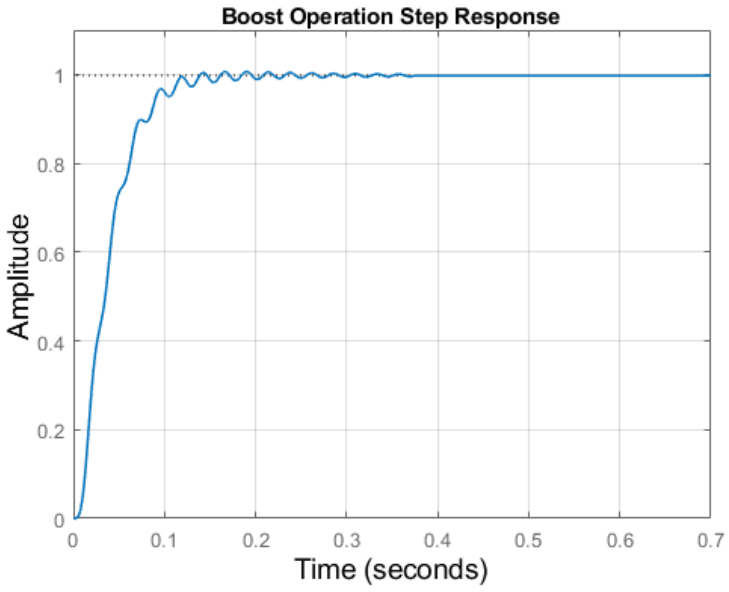

(a)

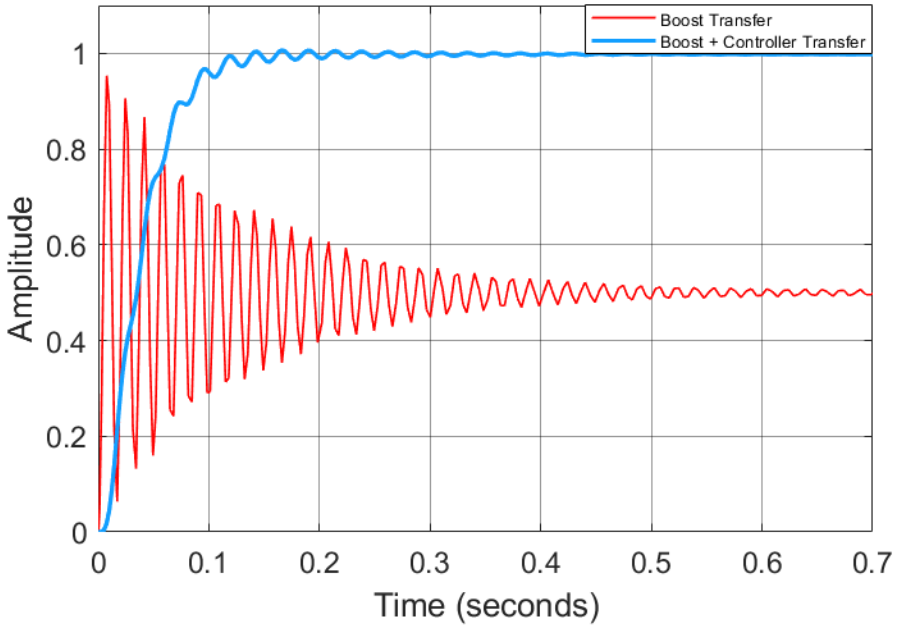

(b)

Figure 5.8 Boost Operation Step Response Transfer Function with a controller/ Compensator. (a) Boost + Controller/ Compensator Transfer MATLAB Plot. (b) Boost Transfer and Boost + Controller/ Compensator Transfer Simulink Simulation Plot.

5.1.3 Buck – Boost Circuitry Model Simulink Results

Fig. 5.9 illustrates and Table 5.1 presents the simulation results of the Simulink buck-boost DC-DC converter circuitry model in Fig. 4.7 working in conjunction with the feedback controller in Fig. 4.8. The simulation is conducted to validate the response of the boost and buck operations of the DC-DC converter. The input voltage was varied from below system bus voltage 48V DC to above system bus voltage to observe if the converter and feedback controller would manage to regulate the system bus voltage to 48V DC. The DC-DC converter with feedback controller managed to regulate the system bus voltage by boosting an input voltage less than 48V DC and bucking an input voltage greater than 48V DC.

Table 5.1 Buck-Boost input and output voltage simulated results.

Variable Input Voltage		**Variable Load**	
V_{IN} **(v)**	V_{OUT} **(v)**	**Resistance (Ω)**	V_{OUT} **(v)**
100	48.05	10	48.05
70	48.05	8	48.05
50	48.05	6	48.05
30	48.05	4	48.05
15	47.8	2	48.05
15	47.6	2	48.05
30	48.05	4	48.05
50	48.05	6	48.05
70	48.05	8	48.05
100	48.05	10	48.05

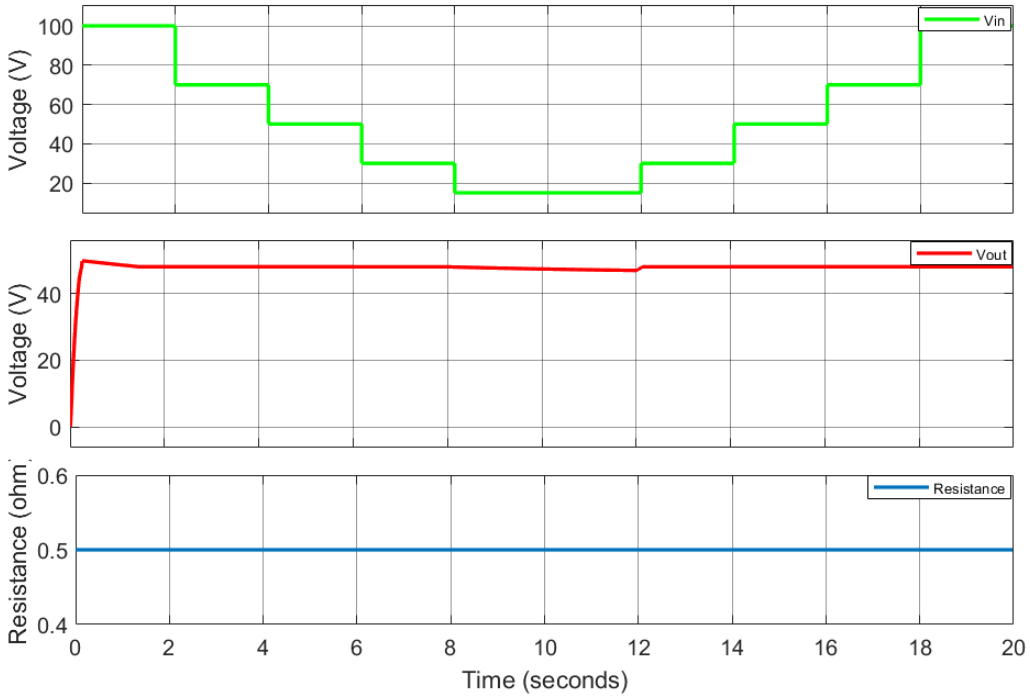

(a)

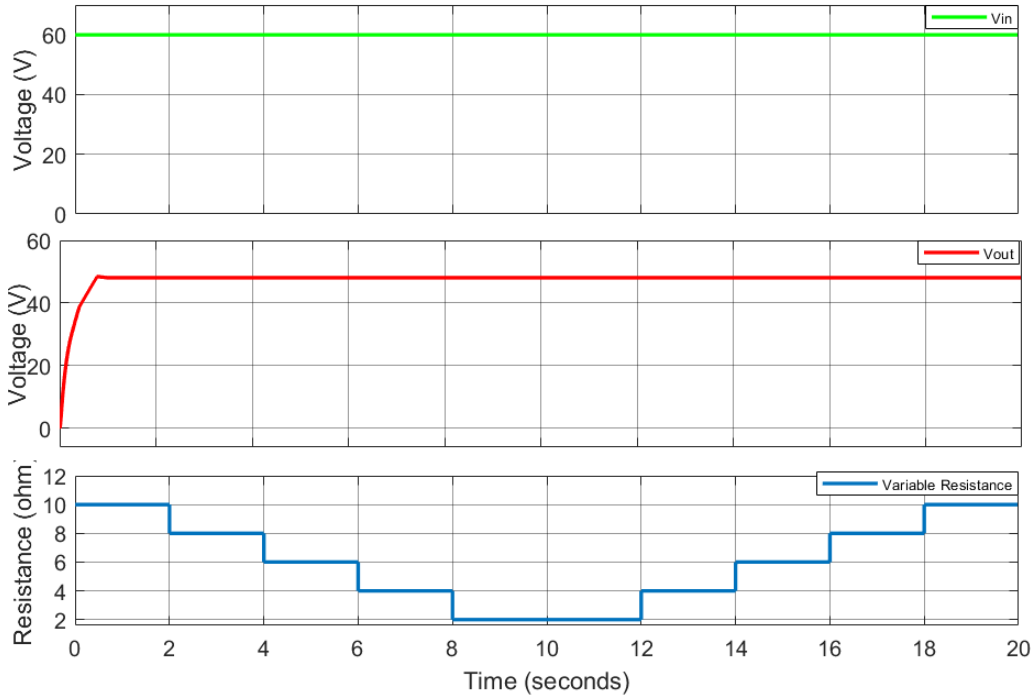

(b)

Figure 5.9 Buck-Boost DC-DC converter with a feedback controller. (a) Variable Input Voltage. (b) Variable Load.

5.2 MPPT P&O and MPPT-Feedback Controller Results

Fig. 5.10 – 5.14 illustrates the response of the MPPT controller when solar radiation changes. To test and observe the response of Fig. 4.10 the MPPT controller, solar radiation input for the PV array was first varied from a maximum of 1000 W/m^2 in steps of 200 to a minimum of 0 W/m^2 and back to 1000 W/m^2 as illustrated by Fig. 5.10(a) and 5.13(a). The second test was conducted with the hourly average GHI of the selected location obtained from [56] as illustrated by Fig. 5.10(b) and 5.13(b). Furthermore, the MPPT response was tested while varying the load as illustrated by Fig. 5.11 and 5.14.

The PV array harvested the maximum power when solar radiation changes due to environmental changes, indicating the efficient operation of the MPPT controller algorithm implemented in Fig. 4.10. Table 5.2 compares the simulated PV array output with MPPT in Fig. 5.10 (b) and the ideal MPP PV array output illustrated by Fig. 5.15, the ideal MPP results for the array were pulled from the PV array block in Simulink. The difference in output power for different solar radiation levels is too small which indicates that the MPPT controller has high efficiency.

Furthermore, the MPPT controller was unified with the feedback controller. Unifying the two controllers enables the PV array system to harvest the maximum power while regulating the Bus voltage [96]. It can be observed in Fig. 5.12 that the MPPT controlled PV array can harvest maximum power but fails to regulate the Bus voltage. Fig. 5.13 illustrates the results of the MPPT controller working in conjunction with the feedback controller, Fig. 5.14 illustrates the results when the load is varied. It can be observed that even when the load is varied the MPPT-Feedback controller was able to achieve the desired results. The MPPT-feedback controller which unifies the maximum power harvest and voltage regulation is illustrated in Fig 4.12.

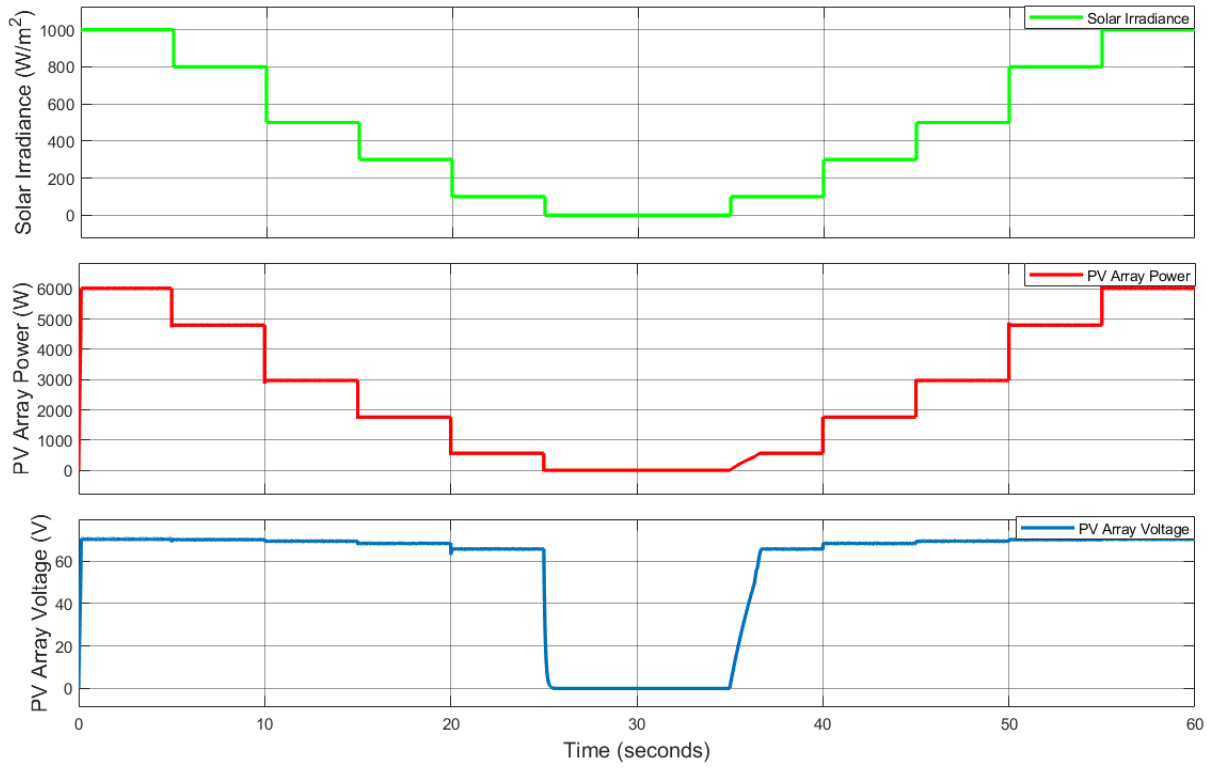

(a)

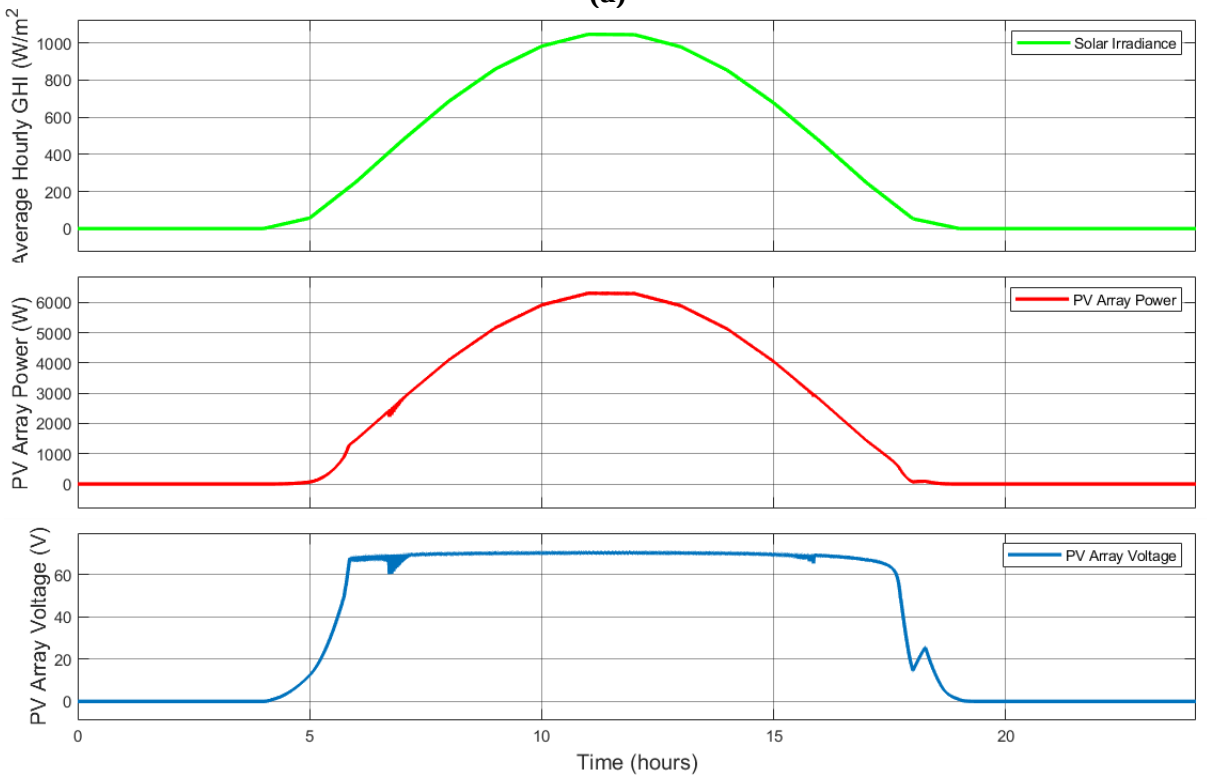

(b)

Figure 5.10 Buck-Boost DC-DC converter with MPPT controller without BES and feedback controller. (a) Self-generated Solar irradiance. (b) monthly hourly average irradiance data for September.

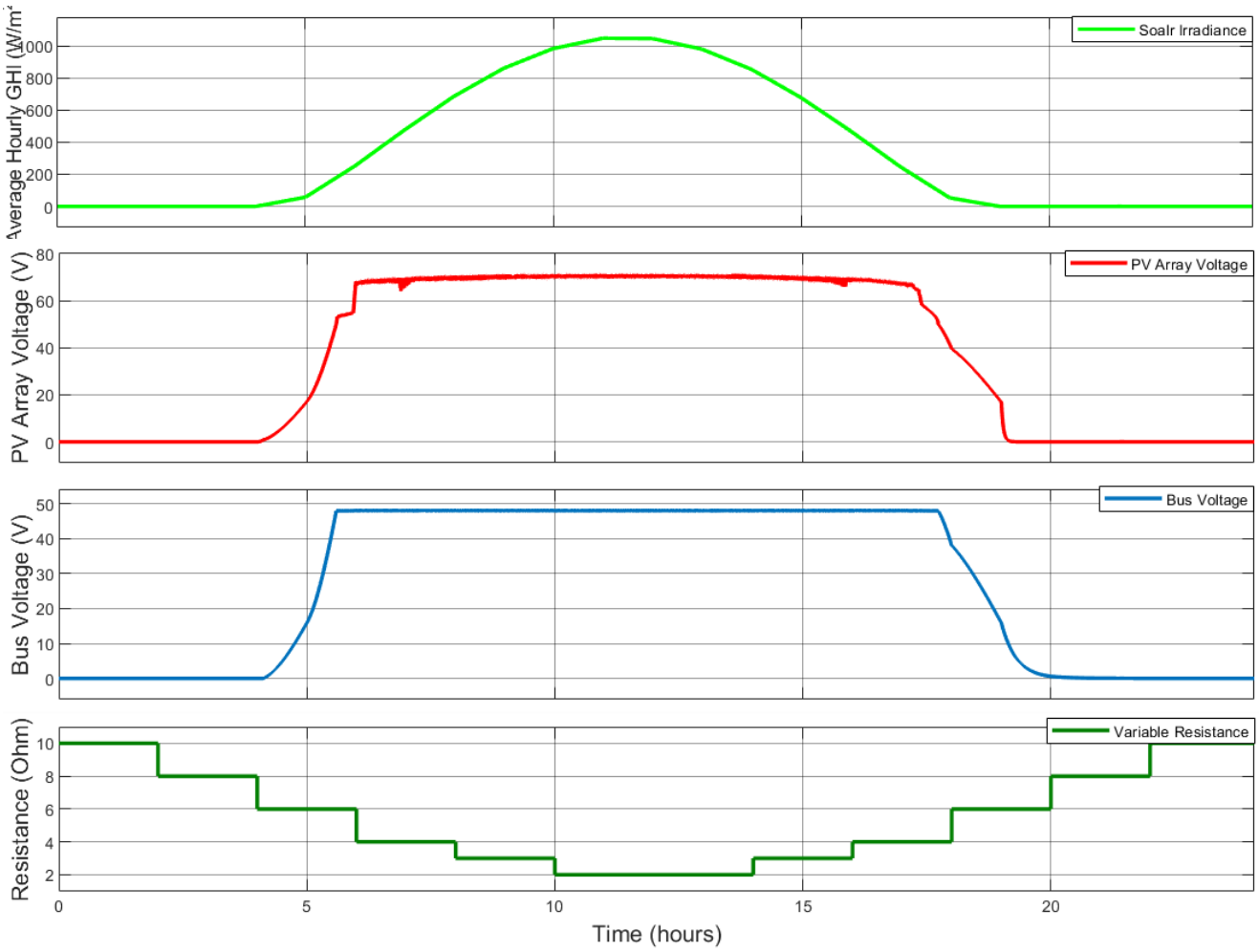

Figure 5.11 Buck-Boost DC-DC converter with MPPT controller without BES and feedback controller. Variable load simulation

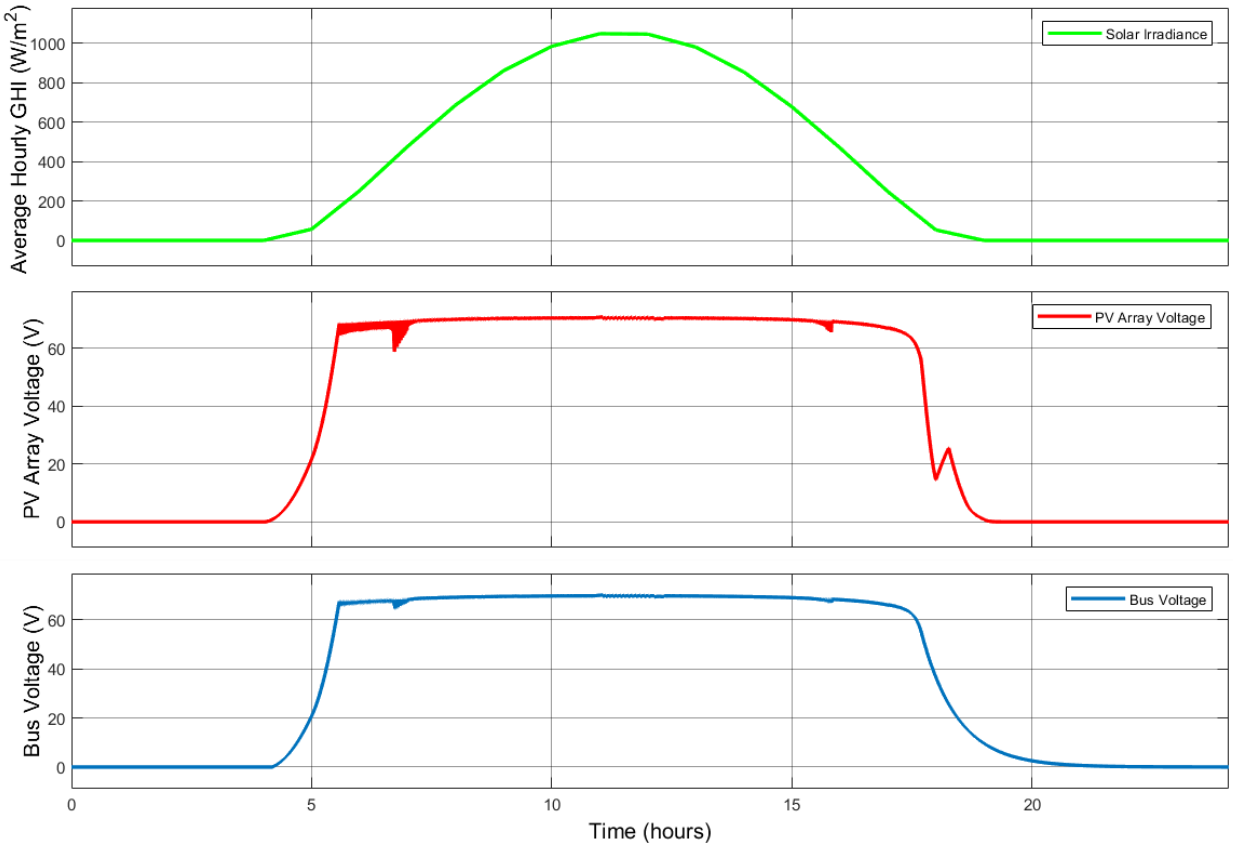

Figure 5.12 Buck-Boost DC-DC converter with MPPT controller without BES and feedback controller. Bus voltage when MPPT controller is utilized.

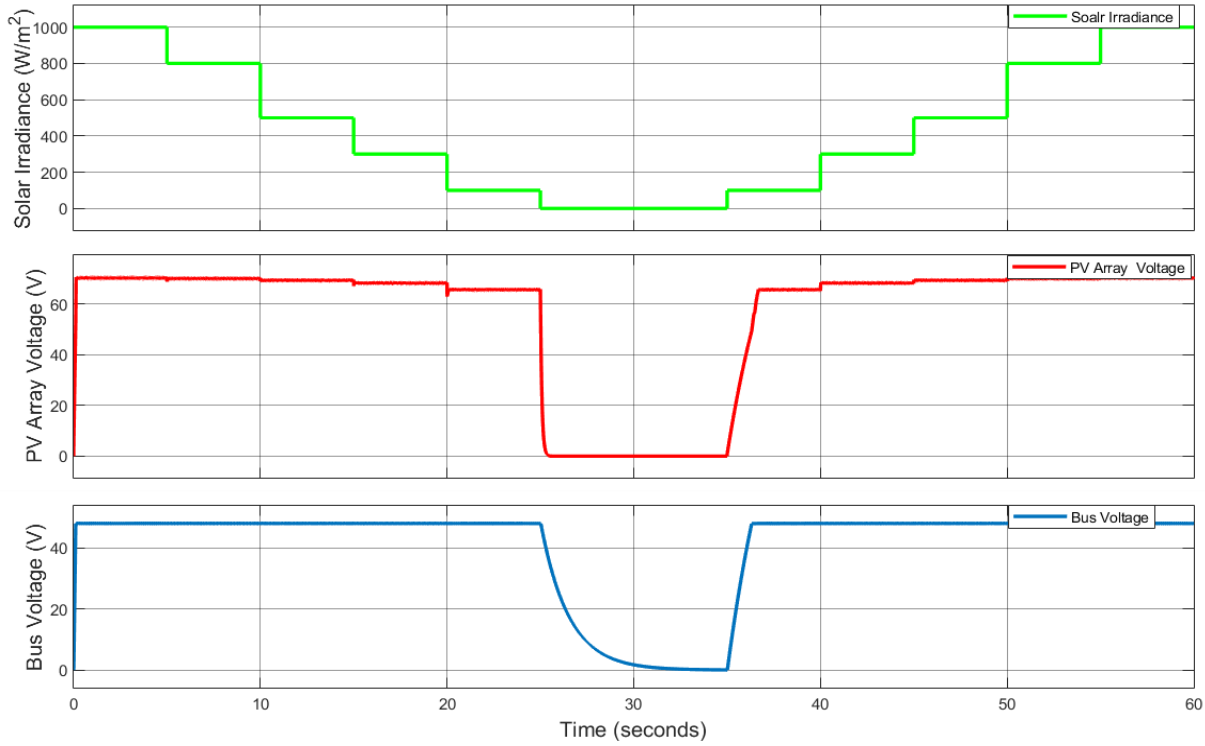

(a)

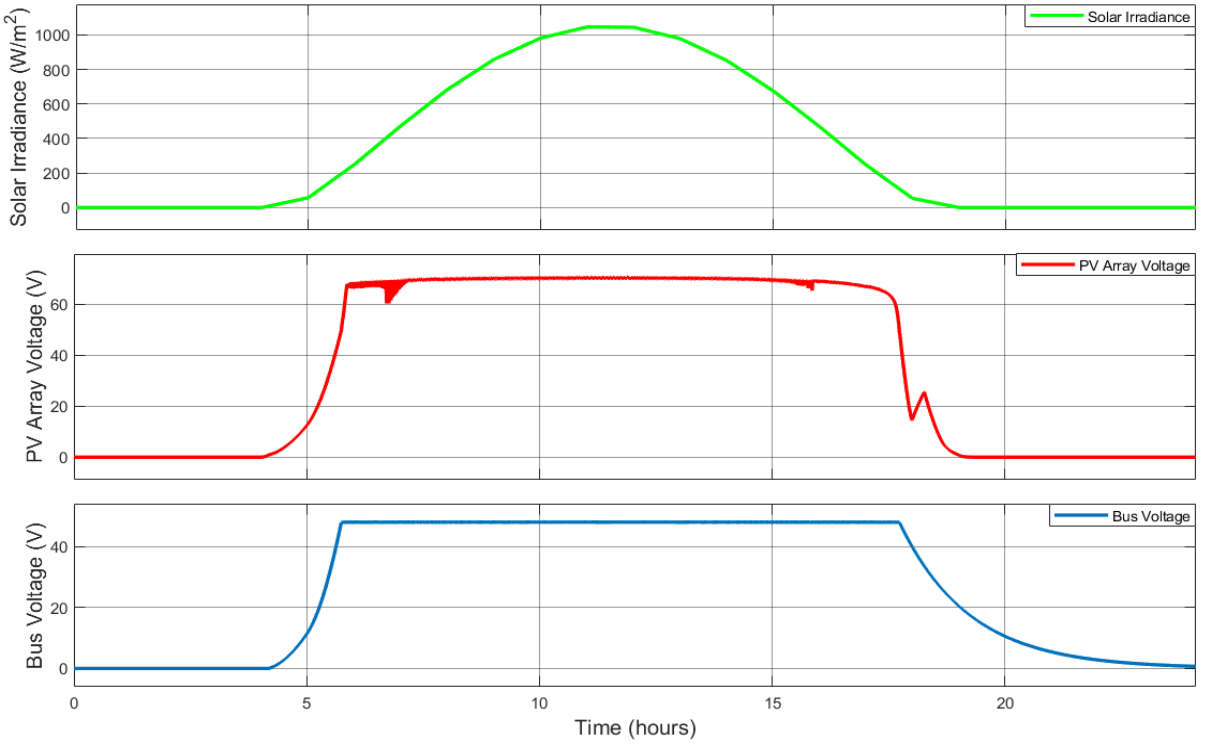

(b)

Figure 5.13 Buck-Boost DC-DC converter with MPPT controller working in conjunction with feedback controller, Observing PV voltage and Bus voltage. (a) Self-generated Solar irradiance, (b) monthly hourly average irradiance data for September.

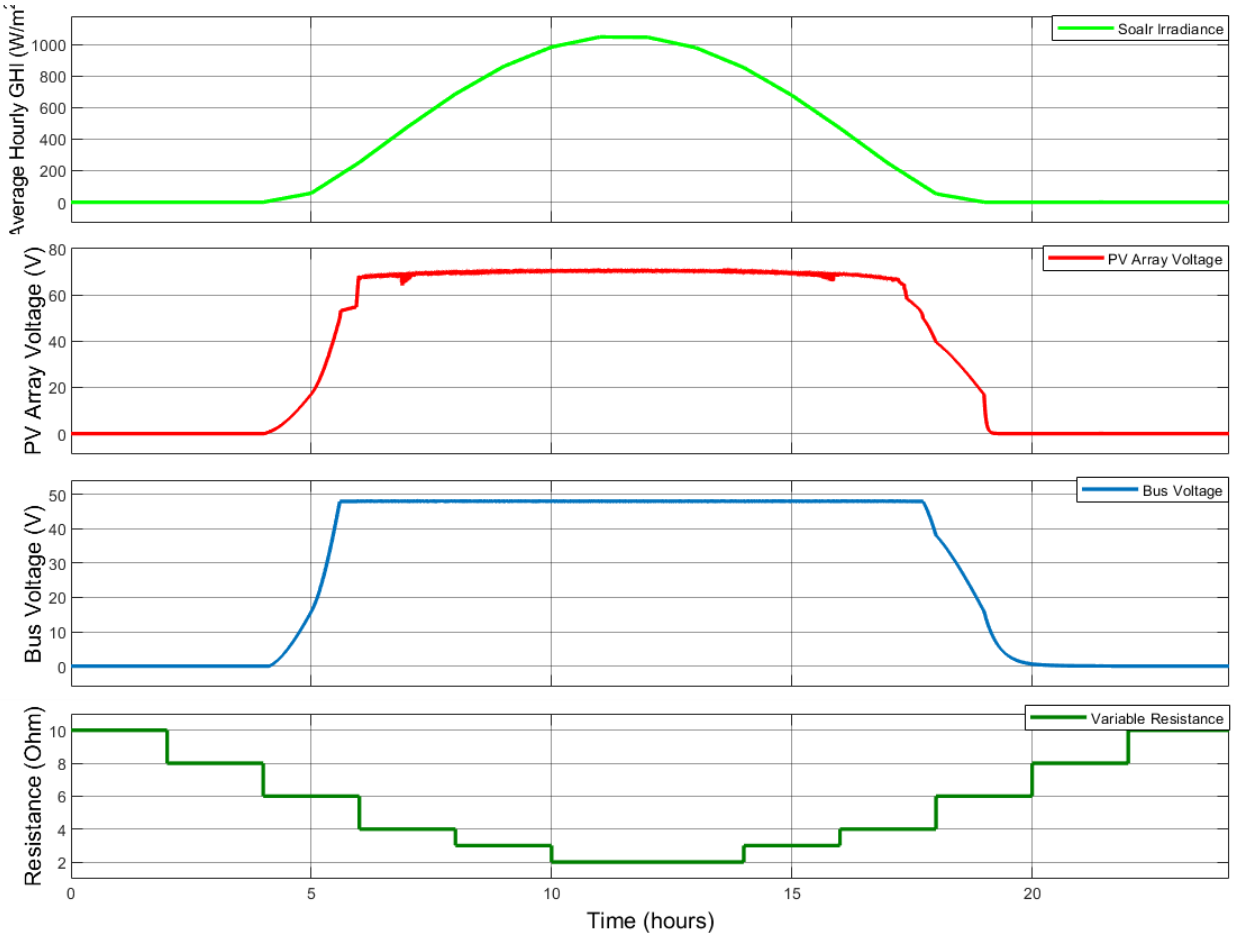

Figure 5.14 Buck-Boost DC-DC converter with MPPT controller working in conjunction with feedback controller, Observing PV voltage and Bus voltage. Variable load simulation.

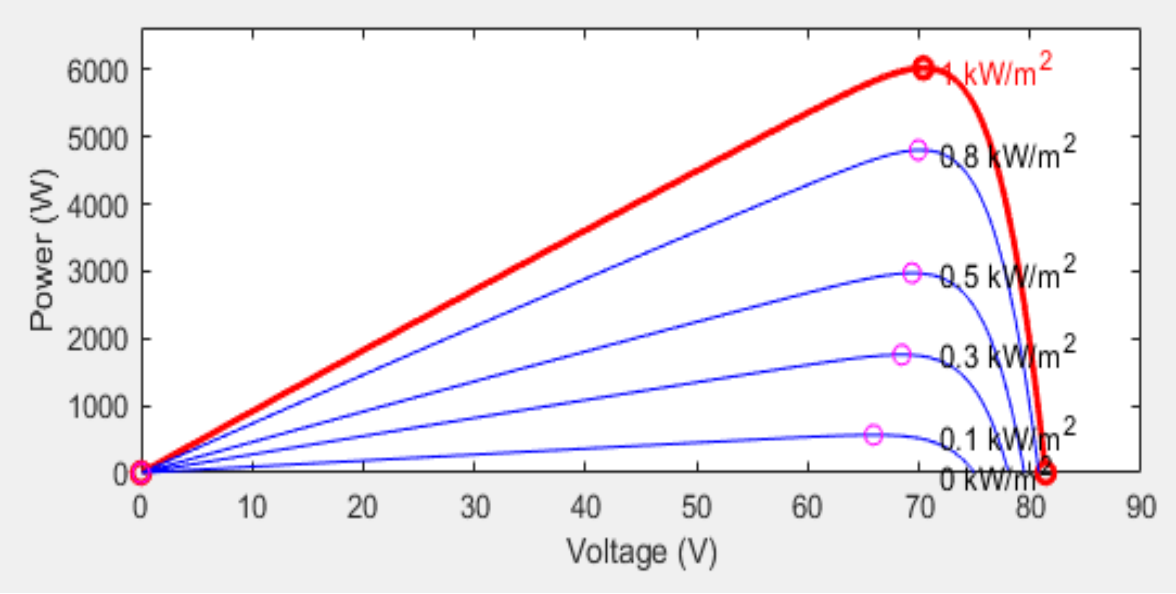

Figure 5.15 Ideal MPP graph for the designed PV array

Table 5.2 Comparison of Array ideal MPP and MPPT function

IDEAL MPP			MATLAB FUNCTION MPP		
IRRADIANCE	PV_P MPP	PV_V MPP	PV_P MPP	PV_V MPP	V_OUT
1000	6022	70.4	6020	70.66	48.05
800	4801	69.9	4804	69.9	48.05
500	2971	69.4	2973	69.5	48.05
300	1757	68.5	1758	68.5	48.05
100	563	65.5	564	65.8	48.05
0	0	0	0	0	0

5.3 Battery Energy Storage BMS Results

The BES system charge controller SIMULINK model was simulated, and the results are illustrated in Fig. 5.16. The simulation occurred for 10 hours, for the first 5 hours the switch between the source and the load was closed illustrated in Fig. 4.13 allowing power from the source to cater to the load and charge the BES. The last 5 hours the switch was opened and there was no power flowing from the source to the loads, the BES system took over and supplied power to the loads. During the transition from the source power to the BES system power a small undershoot can be observed on the bus voltage plot.

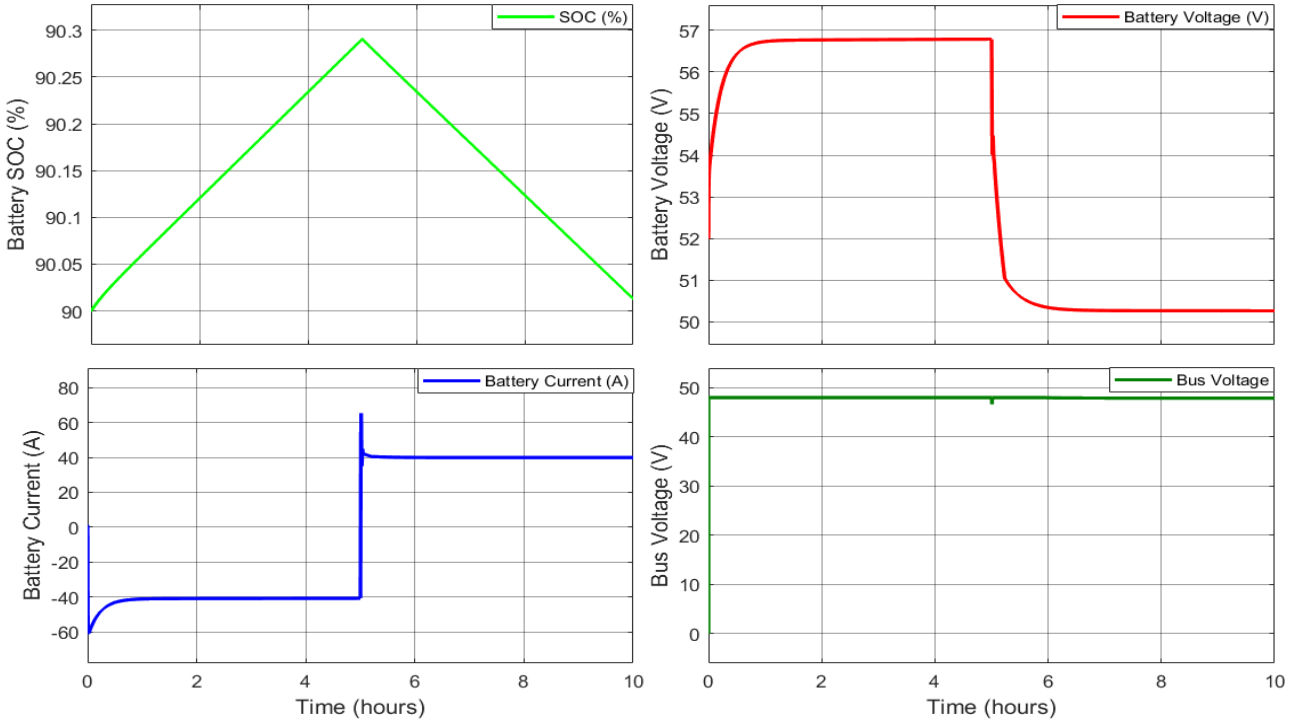

Figure 5.16 Battery Charge Controller and Battery Management System Results.

5.4 Microgrid Subgrid Results

A microgrid subgrid was simulated by combining the components designed and simulated in Chapter 4, the PV array, DC-DC converter, MPPT-feedback controller, and the BMS. The simulation aimed to observe the response of the components working in conjunction to provide optimum service to the user. The results of the simulation are illustrated in Fig. 5.17, during the period when the PV array was unable to harvest enough power for the loads, the BES system with enough capacity was discharged to supplement the PV array shortcoming.

Moreover, during the 6h00-17h59 period, mode 2 was activated, because enough power was harvested from the PV array, and during the 18h00 – 5h59 period mode 3 was activated as power harvested from the PV array was not enough for the demand, the BES system was discharged to supplemented and cover the load demand.

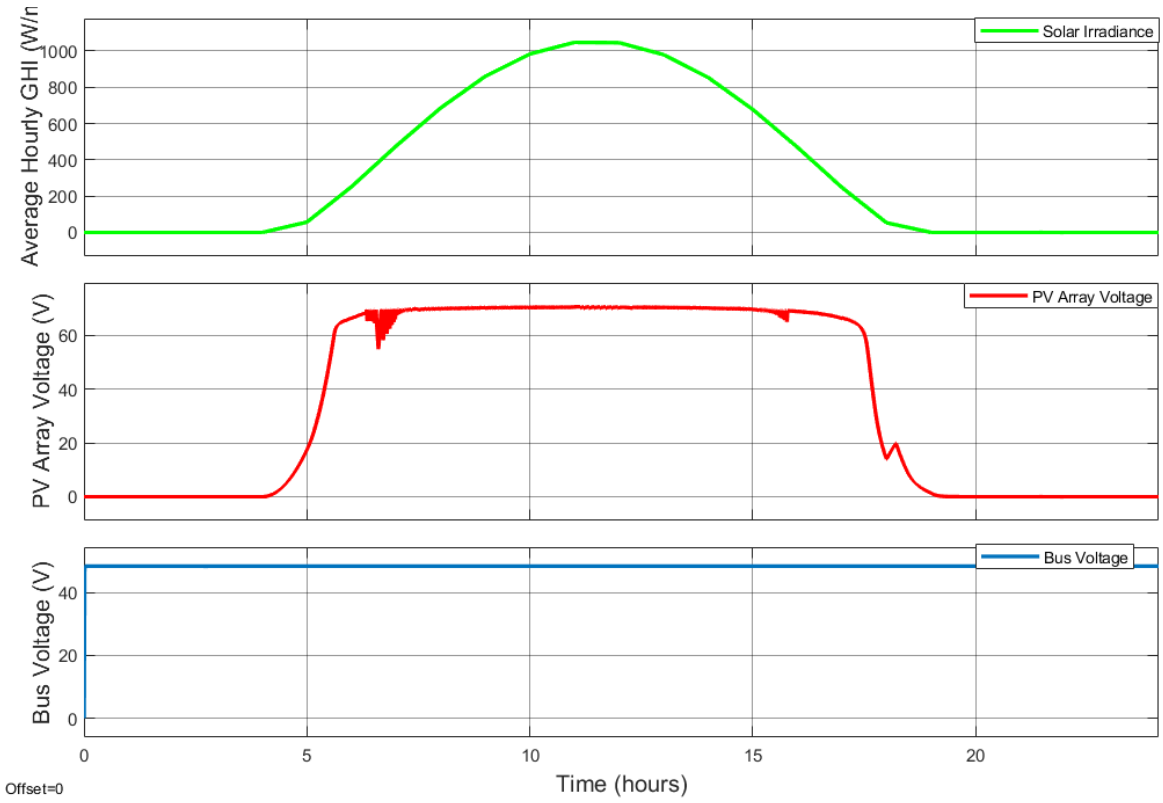

Figure 5.17 Microgrid Simulation Results with battery backup.

5.5 Power-sharing Microgrid Results

This section illustrates and discusses the results obtained from simulating the 3 scenarios discussed in section 4.9. The results observed show that the PSMS Simulink model responds very well to changes imposed on the subgrids.

Scenario 1

Fig. 5.18 illustrates the results for this scenario. It can be observed all subgrids are self-sustaining when no changes are imposed that affect the operation. The local control for subgrids can be observed from Fig. 5.18, from 18h00 to 05h59 the local DC bus voltage is regulated by the BES system, and the subgrids are operating in mode III. From 06h00 to 17h59 the local bus voltage is regulated by the PV array system and the subgrid is operating in Mode II then Mode I.

Scenario 2

Fig. 5.19 illustrates the results for this scenario. It can be observed that the subgrid D BES system was disconnected due to low SOC which led to the subgrid failing to self-sustain during 00h00-05h59 period when no power was harvested from the PV arrays, the subgrid was operating in mode IV. Power sharing was not initiated since during this period power harvested from PV arrays was less than demand, however as the PV array began to generate more power due to an increase in solar irradiance subgrid D transitioned from mode VI to mode II from 06h00-17h59 and further transitioned to mode III from 18h00.

Scenario 3

Fig.5.20 illustrates the results obtained for this scenario. It can be observed subgrid D experienced a technical fault at the harvest side, though solar irradiance was available for electricity to be harvested from the sun, however, subgrid D was unable to harvest the electricity. Around 12h00 the PSMS initiated power sharing since subgrid A BES was fully charged, then subgrid D transitioned from mode VI to mode III assisted by the excess power shared by subgrid A. During 12h00-17h59 subgrid D demand was catered for with power shared by subgrid D, however from 18h00 sharing had to be halted since subgrid A power harvested from the primary source was less than the load demand and subgrid D transitioned to mode III then back to mode VI.

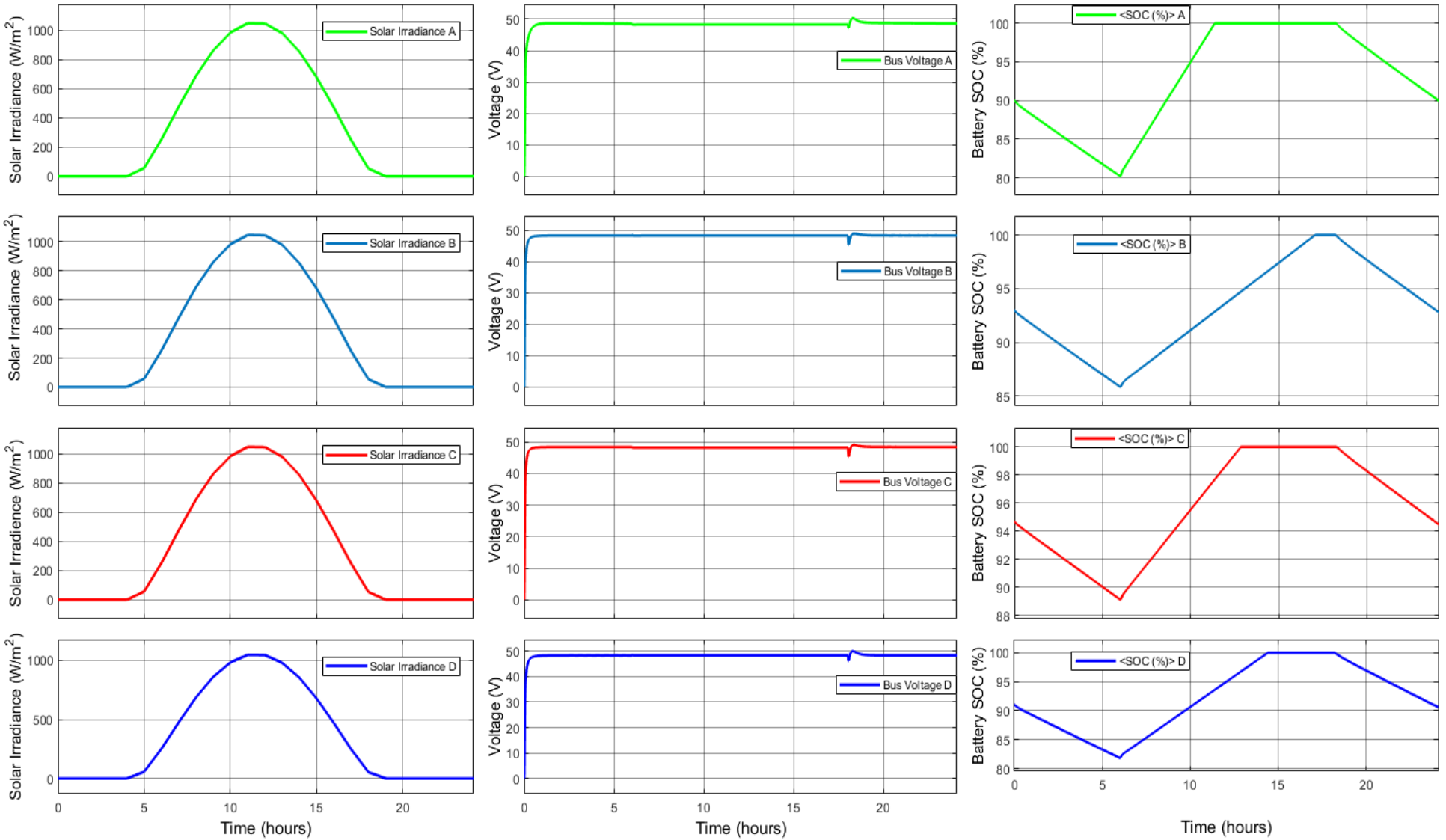

Figure 5.18 Microgrid Simulink Model Simulation Results for Scenario 1

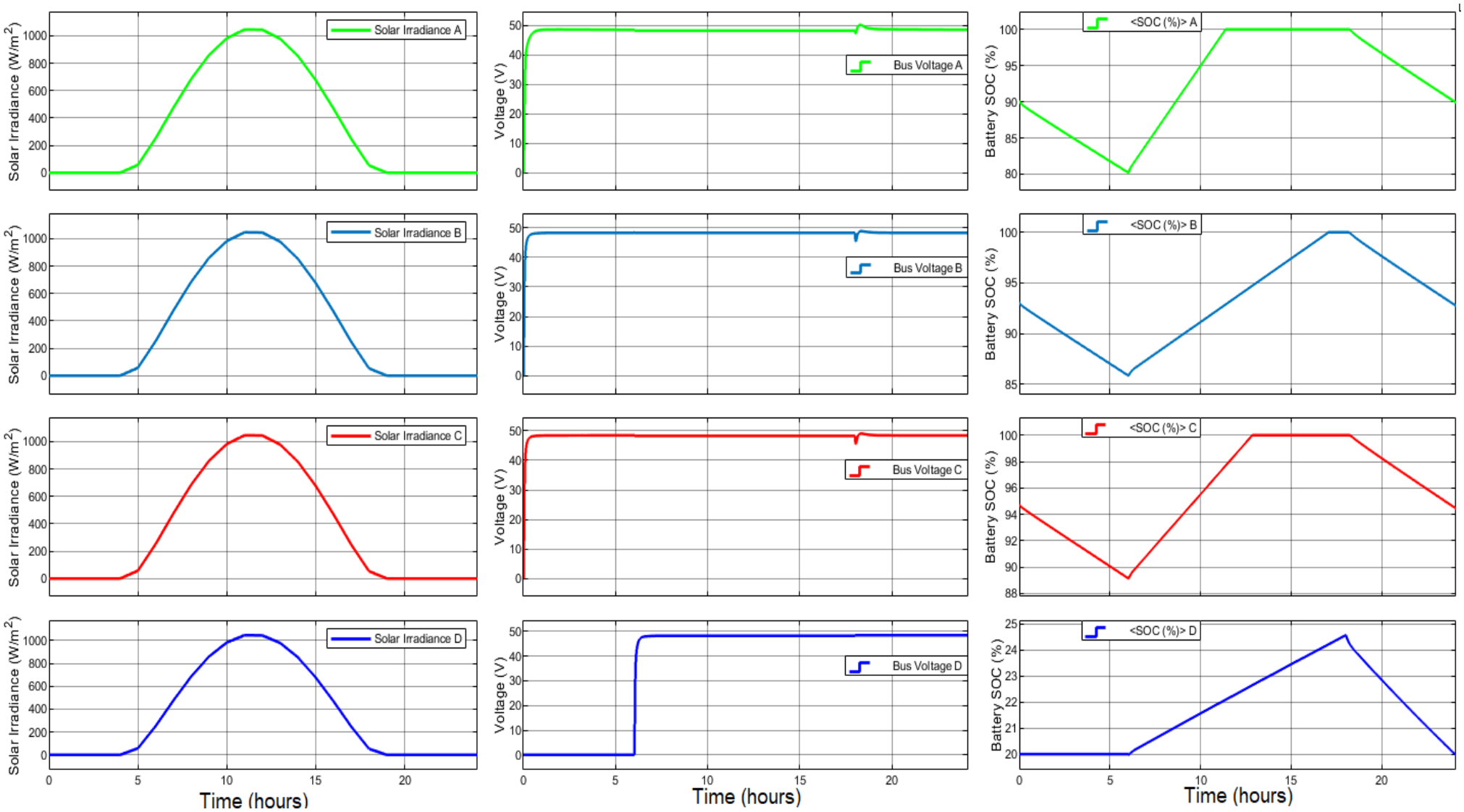

Figure 5.19 Microgrid Simulink Model Simulation Results for Scenario 2

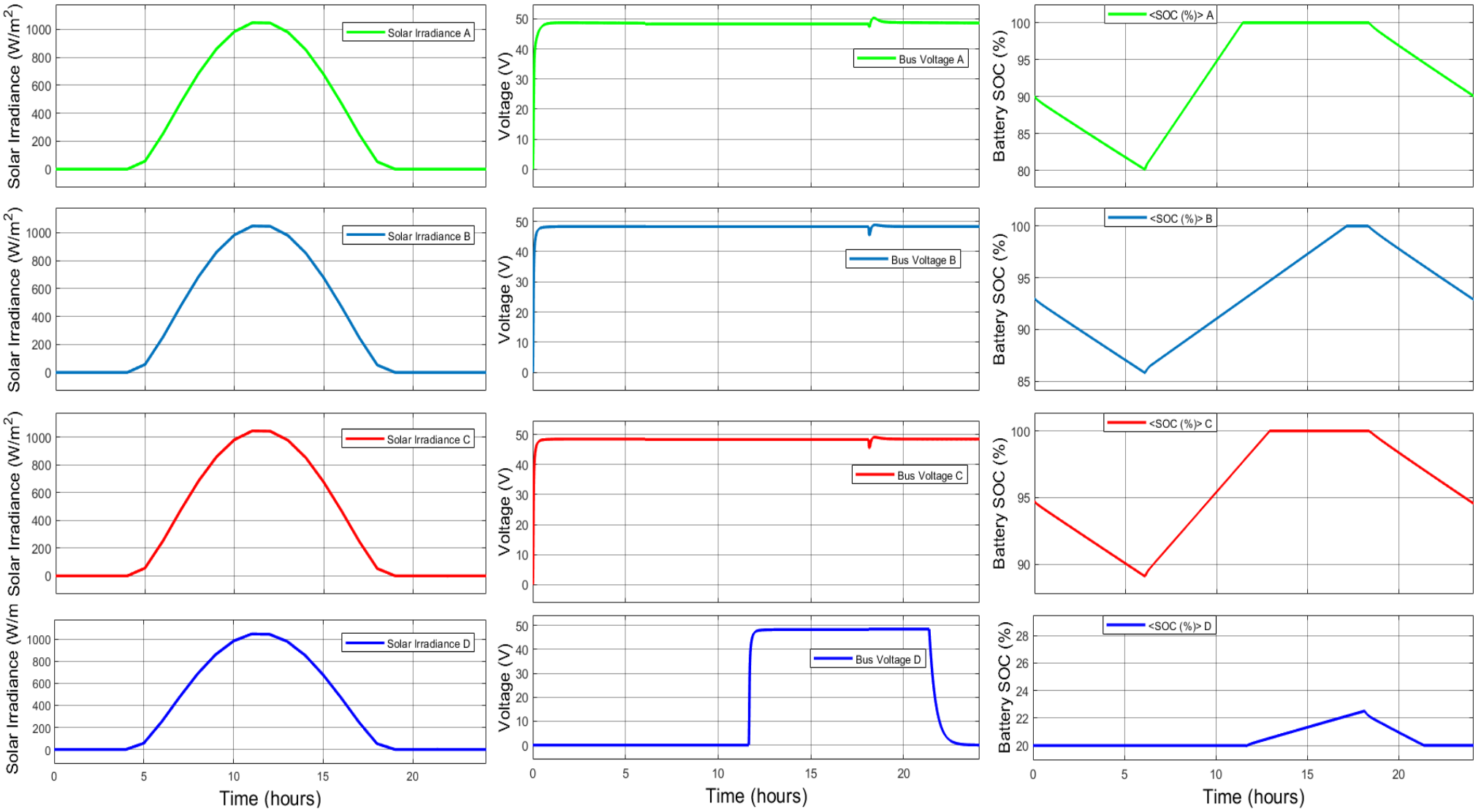

Figure 5.20 Microgrid Simulink Model Simulation Results for Scenario 3

CHAPTER 6 CONCLUSION

6.1 Summary

The research presented an intelligent standalone DC microgrid design with multiple subgrids based on renewable DER. The proposed design aimed to implement an optimum PV standalone DC microgrid that has no link whatsoever with the utility grid. To achieve such a system, proper planning and design are vital steps followed in implementing the microgrid. The design can be applied to electrify rural areas and areas that want to disconnect from the power grid to save the environment.

Efforts are being made to move away from energy generated from fossil fuels to protect the environment. Implementation of RERs is one of the efforts. Even though some of the RERs are intermittent, researchers present new and improved designs now and then to ensure RERs are optimum for users. The ability of the proposed interconnected subgrids to share power is beneficial for users, especially the users of the subgrid that is not self-sustaining due to some technical faults.

The results showed favorable benefits to the users of the subgrid that may be affected, while they wait for technicians to fix the fault, other subgrids with surplus power can sustain them. The designed PSMS facilitates power sharing and requires no communication network infrastructure which is cheap, and easy to implement. The PSMS monitors all subgrids and initializes power sharing if necessary, and if conditions are met for both the sharing and accepting subgrid.

The control of each subgrid is vital for a successful implementation of the PSMS, local controller Simulink models were designed and simulated to observe their response to changes. The local control includes the MPPT controller and feedback controller both for the PV array control and the BMS for BES system control. The results obtained verified that the local control was able to regulate the local DC bus voltage.

Moreover, the proposed microgrid components were simulated on Simulink to verify that the desired design indeed enables power sharing between subgrids when certain conditions are met. Global control is the drive behind the PSMS. The results obtained from simulations verified that

the PSMS was able to initiate and cut power sharing based on command signals generated by the global control.

A. Future Work

Future work will include practically designing a small scale renewable DERs DC microgrid that will apply the PSMS.

Bibliography

[1] *Integrated Resource Plan 2019*. [Online] Available: http://www.energy.gov.za/IRP/2019/IRP-2019.pdf. (Accessed: 12-12-2020).

[2] E. El Shenawy, A. Hegazy, and M. Abdellatef, "Design and optimization of stand-alone PV system for Egyptian rural communities," *International Journal of Applied Engineering Research*, vol. 12, no. 20, pp. 10433-10446, 2017. [Online]. Available: https://www.ripublication.com/ijaer17/ijaerv12n20_168.pdf. (Accessed: 29-01-2022).

[3] Solagis. "Solar Resource Map." Solargis. https://solargis.com. (Accessed: 11-11-2021).

[4] G. Arunkumar, D. Elangovan, P. Sanjeevikumar, J. B. H. Nielsen, Z. Leonowicz, and P. K. Joseph, "DC grid for domestic electrification," *Energies*, vol. 12, no. 11, p. 2157, 2019. [Online]. Available: https://www.mdpi.com/1996-1073/12/11/2157. (Accessed: 12-03-2020).

[5] F. Li, J. Qin, Y. Wan, and T. Yang, "Decentralized Cooperative Optimal Power Flow of Multiple Interconnected Microgrids via Negotiation," *IEEE Transactions on Smart Grid*, vol. 11, no. 5, pp. 3827-3836, 2020, doi: 10.1109/TSG.2020.2989929. (Accessed: 20-03-2020).

[6] D. Pullaguram, S. Mudaliyar, S. Mishra, and N. Senroy, "Isolated PV battery management system to power home appliances," presented at the 2017 7th International Conference on Power Systems (ICPS), 2017. [Online]. Available: https://ieeexplore.ieee.org/stamp/stamp.jsp?tp=&arnumber=8387390. (Accessed: 04-07-2020).

[7] DMRE. "Renewable Energy." Department: mineral resources and energy, Republic of South Africa https://www.energy.gov.za/files/esources/renewables/r_solar.html. (Accessed: 17-08-2020).

[8] N. L. Panwar, S. C. Kaushik, and S. Kothari, "Role of renewable energy sources in environmental protection: A review," *Renewable and Sustainable Energy Reviews*, vol. 15, no. 3, pp. 1513-1524, 2011, doi: https://doi.org/10.1016/j.rser.2010.11.037. (Accessed: 31-10-2020).

[9] M. Denchak, "Fossil Fuels: The Dirty Facts," Natural Resource Defense Council, 2022. [Online]. Available: https://www.nrdc.org/stories/fossil-fuels-dirty-facts#sec-whatis. (Accessed 01-06-2022).

[10] S. Bertrand, "Climate, Environmental, and Health Impacts of Fossil Fuels (2021)," 2021. [Online]. Available: https://www.eesi.org/papers/view/fact-sheet-climate-environmental-and-health-impacts-of-fossil-fuels-2021. (Accessed: 10-01-2023)

[11] A. Gani, "Fossil fuel energy and environmental performance in an extended STIRPAT model," *Journal of Cleaner Production*, vol. 297, p. 126526, 2021. [Online]. Available: https://doi.org/10.1016/j.jclepro.2021.126526 (Accessed: 15-02-2023).

[12] F. Martins, C. Felgueiras, M. Smitkova, and N. Caetano, "Analysis of fossil fuel energy consumption and environmental impacts in European countries," *Energies*, vol. 12, no. 6, p. 964, 2019. [Online]. Available: ttps://doi.org/10.3390/en12060964. (Accessed: 01-05-2023).

[13] O. Krishan and S. Suhag, "An updated review of energy storage systems: Classification and applications in distributed generation power systems incorporating renewable energy resources," *International Journal of Energy Research*, vol. 43, no. 12, pp. 6171-6210, 2019, doi: https://doi.org/10.1002/er.4285. (Accessed: 26-07-2022).

[14] N. Panwar, S. Kaushik, and S. Kothari, "Role of renewable energy sources in environmental protection: A review," *Renewable and sustainable energy reviews*, vol. 15, no. 3, pp. 1513-1524, 2011. (Accessed: 31-10-2020).

[15] V. Quaschning, *Understanding renewable energy systems*: Routledge, 2016. [Online]. Available: https://www.taylorfrancis.com/books/mono/10.4324/9781315769431/understanding-renewable-energy-systems-volker-quaschning. (Accessed on: 13-06-2020).

[16] A. A. Adenle, "Assessment of solar energy technologies in Africa-opportunities and challenges in meeting the 2030 agenda and sustainable development goals," *Energy Policy*, vol. 137, p. 111180, 2020. (Accessed: 16-03-2022).

[17] A. Rezaee Jordehi, "Allocation of distributed generation units in electric power systems: A review," *Renewable and Sustainable Energy Reviews*, vol. 56, pp. 893-905, 2016, doi: https://doi.org/10.1016/j.rser.2015.11.086. (Accessed: 29-12-2020).

[18] Y. Y. Adajah, S. Thomas, M. S. Haruna, and S. O. Anaza, "Distributed Generation (DG): A Review," presented at the 2021 1st International Conference on Multidisciplinary Engineering and Applied Science (ICMEAS), 2021. [Online]. Available: https://ieeexplore.ieee.org/stamp/stamp.jsp?tp=&arnumber=9692353. (Accessed: 15-07-2022).

[19] J. Kumar, A. Agarwal, and V. Agarwal, "A review on overall control of DC microgrids," *Journal of energy storage*, vol. 21, pp. 113-138, 2019. [Online]. Available: https://www.sciencedirect.com/science/article/pii/S2352152X18302019. (Accessed: 12-02-2021).

[20] S. Augustine, J. Quiroz, M. Reno, and S. Brahma, *DC Microgrid Protection: Review and Challenges*. 2018. (Accessed: 25-05-2021).

[21] D. Kumar, F. Zare, and A. Ghosh, "DC Microgrid Technology: System Architectures, AC Grid Interfaces, Grounding Schemes, Power Quality, Communication Networks, Applications and Standardizations Aspects," *IEEE Access*, vol. PP, pp. 1-1, 2017, doi: 10.1109/ACCESS.2017.2705914. (Accessed: 16-12-2021).

[22] V. Pires, A. J. Pires, and A. Cordeiro, "DC Microgrids: Benefits, Architectures, Perspectives and Challenges," *Energies*, vol. 16, p. 1217, 2023, doi: 10.3390/en16031217. (Accessed: 30-07-2023).

[23] M. Hamza, M. Shehroz, S. Fazal, M. Nasir, and H. A. Khan, "Design and analysis of solar PV based low-power low-voltage DC microgrid architectures for rural electrification," *2017 IEEE Power & Energy Society General Meeting, Chicago,IL*, 2017. [Online]. Available: http://ieeexplore.ieee.org/stamp/stamp.jsp?tp=&arnumber=8274134&isnumber=8273724. (Accessed: 25-10-2021).

[24] G. M. Bokanga, A. Raji, and M. T. Kahn, "Design of a low voltage DC microgrid system for rural electrification in South Africa," *Journal of Energy in Southern Africa*, vol. 25, no. 2, pp. 9-14, 2014. [Online]. Available: http://www.scielo.org.za/scielo.php?pid=S1021-447X2014000200002&script=sci_arttext&tlng=es. (Accessed: 10-10-2020).

[25] S. M. Bhagavathy and G. Pillai, "PV Microgrid Design for Rural Electrification," *Designs*, vol. 2, no. 3, September 2018. [Online]. Available: https://www.mdpi.com/2411-9660/2/3/33. (Accessed: 25-10-2020).

[26] P. Mohanty, K. R. Sharma, M. Gujar, M. Kolhe, and A. N. Azmi, "PV system design for off-grid applications," in *Solar Photovoltaic System Applications*: Springer, 2016, pp. 49-83. (Accessed: 23-04-2021).

[27] T. Khatib and D. H. Muhsen, "Optimal Sizing of Standalone Photovoltaic System Using Improved Performance Model and Optimization Algorithm," *Sustainability*, vol. 12, no. 6, p. 2233, 2020. [Online]. Available: https://www.mdpi.com/2071-1050/12/6/2233. (Accessed: 21-04-2022).

[28] K. Palaniappan, S. Veerapeneni, R. Cuzner, and Y. Zhao, "Assessment of the feasibility of interconnected smart DC homes in a DC microgrid to reduce utility costs of low income households," presented at the 2017 IEEE Second International Conference on DC Microgrids (ICDCM), 2017. [Online]. Available: https://ieeexplore.ieee.org/stamp/stamp.jsp?tp=&arnumber=8001087. (Accessed: 25-09-2020).

[29] S. C. Bhatia, *Advanced Renewable Energy Systems, Two-Volume Set*. Havertown, UNITED STATES: Woodhead Publishing India PVT. LTD, 2014. (Accessed: 30-06-2020).

[30] P. Denholm *et al.*, "Bright future: Solar power as a major contributor to the US grid," *IEEE Power and Energy Magazine*, vol. 11, no. 2, pp. 22-32, 2013. [Online]. Available: https://ieeexplore.ieee.org/stamp/stamp.jsp?tp=&arnumber=6466540. (Accessed: 22-11-2021).

[31] G. Goodstal, *Electrical theory for renewable energy* (no. Book, Whole). Andover;Clifton Park, N.Y;: Delmar, 2013. (Accessed: 25-03-2021).

[32] J. Eccles, "Don't let the sun go down: renewables," *Inside Mining*, vol. 7, no. 8, pp. 50-51, 2014. (Accessed: 24-11-2021).

[33] A. W. Campbell, "THERMOPEDIA," ed, 2011. (Accessed: 25-07-2022).

[34] P. A. Lynn, *Electricity from Sunlight : An Introduction to Photovoltaics*. New York, UNITED KINGDOM: John Wiley & Sons, Incorporated, 2010. (Accessed: 25-05-2020).

[35] G. D. Price, *Power Systems and Renewable Energy : Design, Operation, and Systems Analysis*. New York, UNITED STATES: Momentum Press, 2014. (Accessed: 06-08-2020).

[36] W. Xiao, *Photovoltaic Power System : Modeling, Design, and Control*, New York, UNITED KINGDOM: John Wiley & Sons, Incorporated, pp. 14-15, 2017. [Online]. Available: http://ebookcentral.proquest.com/lib/durbanut-ebooks/detail.action?docID=4856329. (Accessed: 17-07-2021).

[37] G. Price, *Renewable Power and Energy : Photovoltaic Systems*, New York, UNITED STATES: Momentum Press, 2018. [Online]. Available: http://ebookcentral.proquest.com/lib/durbanut-ebooks/detail.action?docID=5485377. (Accessed on: 25-04-2020).

[38] N. P. Grebenchikov, D. O. Varlamov, S. M. Zuev, R. A. Maleev, A. A. Skvortsov, and A. P. Grebenchikov, "Study of Solar Panel Charge Controllers," *Journal of Communications Technology and Electronics*, vol. 65, no. 9, pp. 1053-1061, 2020, doi: 10.1134/S1064226920080057. (Accessed: 15-01-2022).

[39] M. Sarvi and A. Azadian, "A comprehensive review and classified comparison of MPPT algorithms in PV systems," *Energy Systems*, vol. 13, no. 2, pp. 281-320, 2022. [Online]. Available: https://link.springer.com/article/10.1007/s12667-021-00427-x. (Accessed: 20-02-2023).

[40] A. N. A. Ali, M. H. Saied, M. Z. Mostafa, and T. M. Abdel-Moneim, "A survey of maximum PPT techniques of PV systems," presented at the 2012 IEEE Energytech, 2012. [Online]. Available: https://ieeexplore.ieee.org/abstract/document/6304652. (Accessed: 12-06-2021).

[41] D. Saravanan, D. Singh, S. Sinha, R. N. Shaw, and K. Prabu, "A Comprehensive Study of Well-Konown Maximum Power Point Tracking Techniques," in *2020 IEEE International Conference on Computing, Power and Communication Technologies (GUCON)*, pp. 829-837, doi: 10.1109/GUCON48875.2020.9231219, 2020. [Online]. Available: https://ieeexplore.ieee.org/document/9231219. (Accessed: 10-10-2022).

[42] Ö. F. TOZLU and H. ÇALIK, "A review and classification of most used MPPT algorithms for photovoltaic systems," *Hittite Journal of Science and Engineering*, vol. 8, no. 3, pp. 207-220, 2021. [Online]. Available: https://doi.org/10.17350/HJSE19030000231. (Accessed: 25-07-2022).

[43] A. S. Ahmed, B. A. Abdullah, and W. G. A. Abdelaal, "MPPT algorithms: Performance and evaluation," in *2016 11th International Conference on Computer Engineering & Systems (ICCES)*, pp. 461-467, 2016, doi: 10.1109/ICCES.2016.7822048. [Online]. Available: https://ieeexplore.ieee.org/document/7822048. (Accessed: 10-10-2021).

[44] M. M. Iqbal and K. Islam, "Design and simulation of a PV System with battery storage using bidirectional DC-DC converter using Matlab Simulink," *International Journal of scientific & Technology research*, vol. 6, no. 07, 2017. (Accessed: 12-03-2021).

[45] S. Jadhav, N. Devdas, S. Nisar, and V. Bajpai, "Bidirectional DC-DC converter in Solar PV System for Battery Charging Application," in *2018 International Conference on Smart City and Emerging Technology (ICSCET)*, pp. 1-4, 2018, doi: 10.1109/ICSCET.2018.8537391. (Accessed: 25-09-2021).

[46] K. Bharath, H. Choutapalli, and P. Kanakasabapathy, "Control of bidirectional DC-DC converter in renewable based DC microgrid with improved voltage stability," *International Journal of Renewable Energy Research (IJRER)*, vol. 8, no. 2, pp. 871-877, 2018. (Accessed: 21-09-2021).

[47] A. Werth, N. Kitamura, I. Matsumoto, and K. Tanaka, "Evaluation of centralized and distributed microgrid topologies and comparison to Open Energy Systems (OES)," presented at the 2015 IEEE 15th International Conference on Environment and Electrical Engineering (EEEIC), 2015. [Online]. Available: https://ieeexplore.ieee.org/stamp/stamp.jsp?tp=&arnumber=7165211. (Accessed: 19-08-2021).

[48] A. Werth, "Distributed DC Energy Network Using Interconnected Subgrids - A Peer-to-Peer Approach," 2016. [Online]. Available: https://www.researchgate.net/publication/332858244_Distributed_DC_Energy_Network_Using_Interconnected_Subgrids_-_A_Peer-to-Peer_Approach/citation/download. (Accessed: 12-08-2021).

[49] M. Lee, W. Choi, H. Kim, and B.-H. Cho, "Operation schemes of interconnected DC microgrids through an isolated bi-directional DC-DC converter," presented at the 2015

IEEE Applied Power Electronics Conference and Exposition (APEC), 2015. [Online]. Available: https://ieeexplore.ieee.org/stamp/stamp.jsp?tp=&arnumber=7104769. (Accessed: 19-08-2021).

[50] U. Vuyyuru, S. Maiti, and C. Chakraborty, "Active power flow control between dc microgrids," *IEEE Transactions on Smart Grid*, vol. 10, no. 5, pp. 5712-5723, 2019. [Online]. Available: https://ieeexplore.ieee.org/stamp/stamp.jsp?tp=&arnumber=8599070. (Accessed: 15-06-2021).

[51] P. Sanjeev, N. P. Padhy, and P. Agarwal, "Autonomous power control and management between standalone DC microgrids," *IEEE Transactions on Industrial Informatics*, vol. 14, no. 7, pp. 2941-2950, 2017. [Online]. Available: https://ieeexplore.ieee.org/stamp/stamp.jsp?tp=&arnumber=8107519. (Accessed: 12-05-2021).

[52] S. Konar and A. Ghosh, "Interconnection of islanded DC microgrids," presented at the 2015 IEEE PES Asia-Pacific Power and Energy Engineering Conference (APPEEC), 2015. [Online]. Available: https://ieeexplore.ieee.org/stamp/stamp.jsp?tp=&arnumber=7380986 (Accessed: 02-02-2021).

[53] N. Altin and S. E. Eyimaya, "A Review of Microgrid Control Strategies," in *2021 10th International Conference on Renewable Energy Research and Application (ICRERA)*, pp. 412-417, 2021, doi: 10.1109/ICRERA52334.2021.9598699. [Online]. Available: https://ieeexplore.ieee.org/document/9598699. (Accessed: 12-07-2022).

[54] StatsSA. "Statistics BY Place." Department: Statistics South Africa. http://www.statssa.gov.za/?page_id=4286&id=8542. (Acessed: 25-10-2020).

[55] "Mhlungwana village," M. T. A. (Pty), Ed., ed: Google, 2021. (Accessed: 12-02-2021).

[56] Solcast. "Solar Irradiance Data." Solcast. https://solcast.com. (Accessed: 10-06-2020).

[57] S. D. Gont, "Design of a standalone photovoltaic system for a typical household around Dessie City-Ethiopia," *American Journal of Electrical and Electronic Engineering*, vol. 7, no. 1, pp. 1-7, 2019. [Online]. Available: https://www.researchgate.net/profile/Solomon-Derbie-2/publication/331320357_Design_of_a_Standalone_Photovoltaic_System_for_a_Typical_Household_around_Dessie_City-Ethiopia/links/5c73bc56299bf1268d231e42/Design-of-a-Standalone-Photovoltaic-System-for-a-Typical-Household-around-Dessie-City-Ethiopia.pdf. (Accessed: 16-12-2021).

[58] M. S. Jadin, I. Z. M. Nasiri, S. E. Sabri, and R. Ishak, "A sizing tool for PV standalone system," *ARPN Journal of Engineering and Applied Sciences*, vol. 10, no. 22, pp. 10727-10732, 2015. [Online]. Available: http://www.arpnjournals.org/jeas/research_papers/rp_2015/jeas_1215_3123.pdf. (Accessed: 12-12-2021).

[59] W. Ali, H. Farooq, A. U. Rehman, Q. Awais, M. Jamil, and A. Noman, "Design considerations of stand-alone solar photovoltaic systems," presented at the 2018 International conference on computing, electronic and electrical engineering (ICE Cube), 2018. [Online]. Available: https://ieeexplore.ieee.org/abstract/document/8610970. (Accessed: 30-01-2022).

[60] *MAXEON 3 SOLAR PANEL 390-400W*, Maxeon, 2022. [Online]. Available: https://sunpower.maxeon.com/int/sites/default/files/2022-02/SPR-MAX3-400%20SPR-MAX3-395%20SPR-MAX3-390_0.pdf (Accessed: 15-01-2022).

[61] *MAXEON 3 SOLAR PANEL 415-430W*, Maxeon, 2022. [Online]. Available: https://sunpower.maxeon.com/int/sites/default/files/2022-02/SPR-MAX3-430%20SPR-MAX3-425%20SPR-MAX3-415_0.pdf (Accessed: 15-01-2022).

[62] J. Svarc. "Most Efficient Solar Panels 2022." Clean Energy Reviews. https://www.cleanenergyreviews.info/blog/most-efficient-solar-panels (Accessed: 01-03-2022).

[63] S. Podder and M. Z. R. Khan, "Comparison of lead acid and Li-ion battery in solar home system of Bangladesh," presented at the 2016 5th International Conference on Informatics, Electronics and Vision (ICIEV), 2016. [Online]. Available: https://ieeexplore.ieee.org/abstract/document/7760041. (Accessed: 25-10-2021).

[64] *LiFe Premium P Series Lithium Battery* [Online]. Available: https://www.powerplus-energy.com.au/wp-content/uploads/2020/11/LiFe-Premium-P-Series-Specification-V6.pdf. (Accessed: 15-01-2022).

[65] *Eco P Series Lithium Battery* [Online]. Available: https://www.rpc.com.au/pdf/powerPlus_energy_eco_series_datasheet.pdf. (Accessed: 15-01-2022).

[66] V. Energy, "SmartSolar Charge Controllers with load output MPPT 75/10, 75/15, 100/15, 100/20, 100/20-48V." [Online]. Available: https://www.victronenergy.com/upload/documents/Datasheet-SmartSolar-charge-controller-MPPT-75-10,-75-15,-100-15,-100-20,-100-20_48V-EN.pdf. (Accessed: 01-02-2022).

[67] V. Energy, "SmartSolar Charge Controller MPPT 150/35 & 150/45." [Online]. Available: https://www.victronenergy.com/upload/documents/Datasheet-SmartSolar-charge-controller-MPPT-150-35-&-150-45-EN.pdf. (Accessed: 01-02-2022).

[68] J. Svarc. "Best MPPT Solar Charge Controllers 2022." Clean Energy Reviews. https://www.cleanenergyreviews.info/blog/best-solar-charge-controllers (Accessed: 01-03-2022).

[69] P. A. Lynn, *Electricity from sunlight: an introduction to photovoltaics*. John Wiley & Sons, 2011. (Accessed: 25-05-2022).

[70] *Cable and Wire Catalogue*, 2018. [Online]. Available: https://www.specifile.co.za/wp-content/uploads/2018/10/Cable-Wire-Catalogue.pdf (Accessed: 10-10-2022).

[71] N. H. Baharudin, T. Mansur, F. A. Hamid, R. Ali, and M. I. Misrun, "Topologies of DC-DC converter in solar PV applications," *Indonesian Journal of Electrical Engineering and Computer Science*, vol. 8, no. 2, pp. 368-374, 2017. [Online]. Available: https://www.researchgate.net/profile/Muhammad-Irwanto/publication/322029190_Topologies_of_DC-DC_converter_in_solar_PV_applications/links/5aa6a192a6fdcc29af531990/Topologies-of-DC-DC-converter-in-solar-PV-applications.pdf. (Accessed: 12-07-2021).

[72] M. Marodkar, S. Adhau, M. Sabley, and P. Adhau, "Design and simulation of DC-DC converters for Photovoltaic system based on MATLAB," in *2015 International Conference on Industrial Instrumentation and Control (ICIC)*, 28-30 May 2015, pp. 1478-1483, doi: 10.1109/IIC.2015.7150983. [Online]. Available:

https://ieeexplore.ieee.org/iel7/7133193/7150576/07150983.pdf?casa_token=OFY5BFf9y1MAAAAA:GJmvT3F0WW5T-UBQ2PUpZNAWwIQuPj2c2nt5QWQ95pdNFOlEnExuxhfgRrdMXooL05EFSujx0RDg. (Accessed: 21-02-2021).

[73] R. Palanisamy, K. Vijayakumar, V. Venkatachalam, R. M. Narayanan, D. Saravanakumar, and K. Saravanan, "Simulation of various DC-DC converters for photovoltaic system," *International Journal of Electrical and Computer Engineering*, vol. 9, no. 2, p. 917, 2019. [Online]. Available: http://download.garuda.kemdikbud.go.id/article.php?article=1305477&val=146&title=Simulation%20of%20various%20DC-DC%20converters%20for%20photovoltaic%20system. (Accessed: 10-02-2022).

[74] V. Bhan *et al.*, "Performance Evaluation of Perturb and Observe Algorithm for MPPT with Buck–Boost Charge Controller in Photovoltaic Systems," *Journal of Control, Automation and Electrical Systems*, vol. 32, no. 6, pp. 1652-1662, 2021/12/01 2021, doi: 10.1007/s40313-021-00781-2. (Accessed: 25-08-2022).

[75] O. Elbaksawi, "Design of photovoltaic system using buck-boost converter based on MPPT with PID controller," *Universal Journal of Electrical and Electronic Engineering*, vol. 6, no. 5, pp. 314-322, 2019. [Online]. Available: https://www.academia.edu/download/91199107/UJEEE2-14913922.pdf. (Accessed: 15-05-2021).

[76] K. A. Ogudo and P. Umenne, "Design of a PV Based Power Supply with a NonInverting Buck-Boost Converter," in *2019 IEEE PES/IAS PowerAfrica*, 20-23 Aug. 2019, pp. 545-549, doi: 10.1109/PowerAfrica.2019.8928656. [Online]. Available: https://ieeexplore.ieee.org/abstract/document/8928656. (Accessed: 26-06-2022).

[77] A. Sarikhani, B. Allahverdinejad, and M. Hamzeh, "A Nonisolated Buck–Boost DC–DC Converter With Continuous Input Current for Photovoltaic Applications," *IEEE Journal of Emerging and Selected Topics in Power Electronics*, vol. 9, no. 1, pp. 804-811, 2021, doi: 10.1109/JESTPE.2020.2985844. (Accessed: 25-11-2022).

[78] H. Fathabadi, "Novel high efficiency DC/DC boost converter for using in photovoltaic systems," *Solar Energy*, vol. 125, pp. 22-31, 2016. [Online]. Available: https://www.sciencedirect.com/science/article/pii/S0038092X15006702?casa_token=iPBxPtZZ7mgAAAAA:VxzdczS1W0RUc-U4SKE6nauDoI7O81XhL2kV9xjkZb59S6tmYhfxclCBkvPEp6IxghoiWgZnaKGh. (Accessed: 23-04-2021).

[79] S. Miao, F. Wang, and X. Ma, "A New Transformerless Buck–Boost Converter With Positive Output Voltage," *IEEE Transactions on Industrial Electronics*, vol. 63, no. 5, pp. 2965-2975, 2016, doi: 10.1109/TIE.2016.2518118. (Accessed: 15-09-2021).

[80] Erickson, *Fundamentals of Power Electronics*. New York, NY, UNITED STATES: Springer, 1997. (Accessed: 12-07-2021).

[81] M. Urbano, *Introductory electrical engineering with math explained in accessible language*. John Wiley & Sons, 2019. (Accessed: 25-10-2022).

[82] M. H. Rashid, *Power electronics handbook*. Butterworth-heinemann, 2017. (Accessed: 20-10-2021).

[83] N. R. S. Harsha, A. Prakash, and D. P. Kothari, "Electromagnetic induction," *The Foundations of Electric Circuit Theory*: IOP Publishing, 2016, pp. 7-1-7-12. [Online]. Available: https://dx.doi.org/10.1088/978-0-7503-1266-0ch7. (Accessed: 10-10-2022).
[84] katkimshow, "Buck Converter Operation and Voltage equation.," ed: YouTube, 2019. (Accessed:).
[85] E. Technology. "Buck Converter." https://www.electricaltechnology.org/2020/09/buck-converter.html (Accessed: 10-05- 2022).
[86] O. Keysan, "EE463-Voltage Ripple in Boost (Step-Up) Converters ", ed, 2020. (Accessed: 25-10-2021).
[87] E. Workbook. "Boost Regulator Peak to Peak Ripple Voltage of Capacitor Expression Derivation." Electrical Workbook. https://electricalworkbook.com/boost-regulator-peak-peak-ripple-voltage-capacitor/ . (Accessed: 25-06-2023).
[88] B. Alajmi, N. A. Ahmed, and A. Al-Othman, "Small-signal analysis and hardware implementation of Boost converter fed PMDC motor for electric vehicle applications," *Journal of Engineering Research*, vol. 9, no. 3B, 2021. [Online]. Available: https://kuwaitjournals.org/jer/index.php/JER/article/view/10213. (Accessed: 12-05-2022).
[89] T. Kamal, U. Arifoğlu, and S. Z. Hassan, "Buck-boost converter small signal model: Dynamic analysis under system uncertainties," 2018. [Online]. Available: https://acikerisim.sakarya.edu.tr/handle/20.500.12619/64886. (Accessed: 25-02-2021).
[90] N. S. Nise, *Control systems engineering*. John Wiley & Sons, 2020. (Accessed: 25-01-2022).
[91] V. Viswanatha, "A complete mathematical modeling, simulation and computational implementation of boost converter via MATLAB/Simulink," 2017. [Online]. Available: https://www.researchgate.net/profile/Viswanatha-V/publication/319911556_A_Complete_Mathematical_Modeling_Simulation_and_Computational_Implementation_of_Boost_Converter_Via_MATLABSimulink/links/59c143230f7e9b21a82655fc/A-Complete-Mathematical-Modeling-Simulation-and-Computational-Implementation-of-Boost-Converter-Via-MATLAB-Simulink.pdf . (Accessed: 21-05-2021).
[92] S.-H. Kim, *Electric motor control: DC, AC, and BLDC motors*. Elsevier, 2017. (Accessed: 25-07-2021).
[93] A. Chitransh and S. Kumar, "The different type of MPPT techniques for photovoltaic system," *Indian Journal of Environment Engineering (IJEE)*, vol. 1, no. 2, pp. 1-4, 2021. [Online]. Available: https://www.ijee.latticescipub.com/wp-content/uploads/papers/v1i2/A1809051121.pdf. (Accessed: 30-06-2023).
[94] Z. M. S. Elbarbary and M. A. Alranini, "Review of maximum power point tracking algorithms of PV system," *Frontiers in Engineering and Built Environment*, vol. 1, no. 1, pp. 68-80, 2021, doi: 10.1108/FEBE-03-2021-0019. (Accessed: 10-12-2022).
[95] M. A. Eltawil and Z. Zhao, "MPPT techniques for photovoltaic applications," *Renewable and Sustainable Energy Reviews*, vol. 25, pp. 793-813, 2013/09/01/ 2013, doi: https://doi.org/10.1016/j.rser.2013.05.022. (Accessed: 25-02-2021).
[96] M. I. Juma, B. M. Mwinyiwiwa, C. J. Msigwa, and A. T. Mushi, "Design of a hybrid energy system with energy storage for standalone DC microgrid application," *Energies*, vol. 14, no. 18, p. 5994, 2021. [Online]. Available: https://doi.org/10.3390/en14185994. (Accessed: 25-10-2022).